FORCED CONVECTION HEAT TRANSFER WITH NANOFLUIDS IN FLAT PLATE SOLAR COLLECTOR

by

Mohammad Jane Alam Khan

A thesis submitted in partial fulfillment of the requirements for the degree of
MASTER OF SCIENCE IN MECHANICAL ENGINEERING

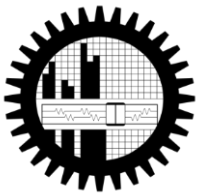

DEPARTMENT OF MECHANICAL ENGINEERING
BANGLADESH UNIVERSITY OF ENGINEERING AND TECHNOLOGY
DHAKA-1000, BANGLADESH

August, 2015

CERTIFICATE OF APPROVAL

This thesis titled, "**Forced Convection Heat Transfer with Nanofluids in Flat Plate Solar Collector**," submitted by **Mohammad Jane Alam Khan**, Roll No.: **0412102012 P**, Session: **April, 2012**, has been accepted as satisfactory in partial fulfillment of the requirements for the degree of MASTER OF SCIENCE IN MECHANICAL ENGINEERING on August, 2015.

BOARD OF EXAMINERS

Dr. Mohammad Arif Hasan Mamun Professor Department of Mechanical Engineering BUET, Dhaka-1000	Chairman (Supervisor)
Dr. Md. Zahurul Haq Professor & Head Department of Mechanical Engineering BUET, Dhaka-1000	Member (Ex-officio)
Dr. Mohammad Ali Professor Department of Mechanical Engineering BUET, Dhaka-1000	Member (Internal)
Dr. Md. Abdul Alim Professor Department of Mathematics BUET, Dhaka-1000	Member (External)

CERTIFICATE OF RESEARCH

This is to certify that the work presented in this thesis is carried out by the author under the supervision of Dr. Mohammad Arif Hasan Mamun, Professor, Departmental of Mechanical Engineering, Bangladesh University of Engineering and Technology, Dhaka, Bangladesh.

Dr. Mohammad Arif Hasan Mamun	Mohammad Jane Alam Khan

DECLERATION

It is hereby declared that this thesis or any part of it has not been submitted elsewhere for the award of any degree or qualification.

Mohammad Jane Alam Khan

Author

Date

ACKNOWLEDGEMENTS

First and foremost, thanks to most merciful, most gracious and the kindest almighty Allah. The author would like to thank his parents, his brother and sister for their constant support and inspirations.

The author would like to pay his earnest gratitude and reverence to his supervisor Dr. Mohammad Arif Hasan Mamun, Professor, Departmental of Mechanical Engineering, Bangladesh University of Engineering and Technology, for his constructive suggestion, meaningful criticism and constant supervision throughout this research.

The author gratefully acknowledges the assistance received at various stages of this work from Dr. Sumon Saha, Assistant Professor, Department of Mechanical Engineering, BUET and Ms. Rehana Nasrin, Assistant Professor, Department of Mathematics, BUET.

Special thanks go to all his colleagues, especially Md. Jamil Hossain, Sheikh Mohammad Shavik, Arif Abdullah Rokoni and KM. Rafidh Hassan for their support and encouragement.

Author

ABSTRACT

Nanofluids are fluids with immersed nanoparticles in it. It demonstrates much higher convective heat transfer coefficient than conventional working fluids. Single-phase and mixture-phase models are the two models that are being used for the nanofluid study. In this study, forced convection heat transfer of nanofluids is done using both single-phase and mixture-phase models and the results are compared with experimental results. The nanofluid is then used as the working fluid in a flat plate solar collector to investigate the performance improvement of the collector. The governing equations of various studies here are discretised using the finite volume method. The models are assumed axi-symmetric and at steady state. Hybrid differencing scheme is used during discretization. A code is written using SIMPLER algorithm and then solved using the MATLAB engine. The mixture-phase model studied here, considers two slip mechanisms between nanoparticle and base-fluid, namely Brownian diffusion and thermophoresis. Al_2O_3-water nanofluid is used for the study of nanofluid and the study shows significant increase in convective heat transfer coefficient while the mixture-phase model demonstrates slightly lower values than the single-phase model. The study is done with various nanoparticle concentrations and Reynolds numbers. With increasing particle concentration and Reynolds number, the convective heat transfer coefficient increases and as well as the shear stress. For low concentrations of the nanoparticle, Nusselt number is slightly lower than the base fluid and as the concentration increases, the Nusselt number also increases than the base fluid. The study also investigates the effect of particle size but the mixture-phase model didn't provide any variation with particle size. The Al_2O_3-water nanofluid is then used as the working fluid of a flat plate solar collector. The study is done with various nanoparticle concentration and flow rates and the efficiency increases with increase of both nanoparticle concentration and flow rates. The efficiency found by Al_2O_3-water nanofluid is then compared with CuO-water nanofluid in the flat plate collector and the CuO-water provides better results. The efficiency increases by 6.6% and 8.6% for Al_2O_3-water and CuO-water nanofluid respectively for 0.025 mL/s of flow rate. There is also a significant efficiency increase of 10.3% found by using internal fins to the riser tube.

List of Symbols

Notation	Definition
r	Radial location
z	Axial location
R	Radius
$\boldsymbol{u}$	Flow velocity vector
V	Velocity
V_0	Normal inflow velocity
p	Pressure
D	Diameter
D_B	Brownian diffusion coefficient
D_T	Thermophoretic diffusion coefficient
$\boldsymbol{T}$	Stress tensor
f	Body forces
h	Convective heat transfer coefficient
S	Source term
k	Thermal conductivity
c_p	Specific heat
k_B	Boltzmann constant
I_t	Solar irradiation
T_α	Ambient temperature
t	Absorber plate thickness
U_L	Overall heat loss coefficient
Pe	Peclet number = Re.Pr
Pr	Prandtl number
Re	Reynolds number
T	Temperature
T_b	Bulk temperature
m	Mass flow rate
L	Total length
T^*	Dimensionless temperature=$(T-T_s)/(T_b-T_s)$

Greek Letters

φ	Nanoparticle volume fraction
ρ	Density
μ	Dynamic viscosity
α	Thermal diffusivity
$\tau\alpha$	Total absorption coefficient for solar plate
η	Efficiency
τ_s	Wall shear stress

Subscript

r	Radial direction
z	Axial direction
np	Nanoparticle
in	Inlet
out	Outlet
av	Average

Contents

List of Figures

List of Tables

Chapter 1

Introduction

Conventional heat transfer fluids, such as water, engine oil, ethylene glycol etc. have limited convective heat transfer coefficient. Industrial process escalation and the technological developments have boosted the necessity for more efficient heat transfer fluids. Evidently, most of the solids, particularly metals have very high conductivity than the fluids. So, there is a possibility that fluids containing solid particles may demonstrate better thermal properties. About a century ago in 1904, Maxwell [1] pioneered an effective conductivity equation for two-phase mixtures which showed an increased conductivity. Following the Maxwell's work, numerous theoretical [2-3] and experimental studies [4-5] were done with suspended solid particles in fluids and gases. These mixtures demonstrate a considerable increase of heat transfer coefficient. Such augmentation is partly because of the increased conductivity of the mixture and partly due to the reduced boundary layer thickness. Prior to the recent development in manufacturing process, studies only involved millimeter and micrometer sized particles. These mixtures could be of limited use because of the drastic pressure drop, rapid settling of particles, clogging, wear of the channel etc. In the recent years, technologies have made it possible to manufacture nano-sized particles and introduce a new working fluid, nanofluid.

The term nanofluid was first coined by Choi [6]. Nanofluid is a two-phase mixture of base fluid and very fine sized particles of size less than 100nm. It is evident from experiments that, nanofluids are very stable (up to a certain volume percentage) and demonstrate a significant increase in heat transfer coefficient. The increased heat transfer coefficient depends on several factors such as the particle size, concentration, thermal properties of both the particles and the fluids etc. Many experimental and numerical studies have been done on understanding the influences of these factors [7-9]. Particle concentration has a positive effect on heat transfer coefficient while particle size has a negative effect. Many researchers have worked on determining the effective thermal conductivity, viscosity etc. of various nanofluids [10-11]. While the results are not always the same but the trend is always the same which is conductivity and viscosity both increase with particle concentration [12-13].

Numerical works on nanofluids are carried out using two approaches, the single-phase model and the two-phase model. In the single-phase model, the basic hypothesis is that the nanofluid behaves like a single-phase fluid with enhanced thermophysical properties due to the inclusion of nanoparticles. In the two-phase model, different factors resulting from nanoparticle immersion such as gravity, Brownian diffusion, thermophoresis, sedimentation, dispersion etc. are considered. Two-phase models can be Eulerian-Eulerian, Eulerian-Lagrangian, mixture model etc. [14-16]. J. Buongiorno has developed a four equation non-homogenous equilibrium model [17] considering the various slip mechanisms between base fluid and the nanoparticles. The two-phase study of nanofluids tends to give better results than the single-phase study. However the results from various two-phase models are not conclusive. The influence of the nano-particles on fluid flow and heat transfer has yet to be clearly understood. More and more research works are needed in this issue for a better numerical modeling of the nanofluids.

Because of the improved thermal properties, nanofluids can be used to design more efficient heat exchangers, electronic cooling devices etc. Application of nanofluids as the working medium for solar thermal collectors is a relatively new concept. To provide the ever increasing need of energy, researchers are now focused on harvesting solar energy [18-20]. It is economically favorable to use solar water heating systems in residential, private, commercial, and industrial buildings, schools, hospitals, hotels, swimming pools, industrial processes etc. Nevertheless solar water heating systems production technology is already well developed, it is being perfected continuously. Currently, the most common types of liquid thermal collectors are the evacuated tube, flat and concentrated ones [21]. Flat plate types have the advantages of reliability, manufacturability, durability and low cost but these types have comparatively low efficiency especially at low irradiance and ambient temperature. Many researchers are nowadays working on flat plate collectors, their traits, their applications and how to improve their efficiency. Use of internal fins and metal heat pipes are some common methods to increase efficiency of the solar collector [22-23]. Besides the conventional methods, researchers are now investigating the possibility of using nanofluids as the working fluid of the flat plate collector. Numerous experimental and numerical works have been done using nanofluids in the flat plate collector [24-26]. These studies show a significant increase in thermal performance of the flat plate collector.

Different kinds of nanofluids have been used for the study of nanofluids in flat plate collector. Al_2O_3-water, CuO-water, Cu-water, MWCNT-water etc. are some common nanofluids that have been used by the researchers. The maximum increase in thermal efficiency is found as high as 28%. The thermal performance of flat plate collectors depend on various factors such as the working fluid, the absorber material, aspect ratio, ambient temperature, solar irradiance, nanofluid, nanofluid concentration etc. It is not always feasible to perform experiment to evaluate the thermal performance of the flat plate collector using nanofluids. A numerical study with appropriate nanofluid modeling can save precious time and money and still provide with the required results. Most of the recent studies have used single-phase model of nanofluids and

constant overall heat loss coefficient in the efficiency evaluation of the flat plate collector. Implementation of mixture-phase model of nanofluid and variable overall heat loss coefficient in the investigation of flat plate collector can provide with a more accurate result of the thermal performance.

1.1 Objectives of the Thesis

The specific objectives of the study are as follows:

a) To study the forced convection heat transfer of nanofluids under laminar flow conditions using the mixture-phase and single-phase models.
b) To investigate the particle diameter sensitivity of the mixture-phase model.
c) To study the performance of a flat plate solar thermal collector using nanofluid as the working fluid.
d) To compare the findings of nanofluid model of solar collector with solar collector of internally finned tubes.

1.2 Scope of the Thesis

The present work involves single-phase and mixture-phase study of nanofluids in a straight circular pipe. Then the nanofluid models are implemented in a flat plate solar collector to evaluate the performance of the collector with nanofluids. This thesis also performs a study of flat plate collector with internally finned tubes. Relevant literatures on nanofluid study, single-phase and two-phase models of nanofluid, flat plate collector performance etc. are reviewed in chapter 2.

In chapter 3, physical geometry of different studies are discussed and graphically shown. Also equivalent numerical domain from the physical domain is shown. In chapter 4, the mathematical modeling of the studies are described. The governing equations for the nanofluid models, their simplified form, boundary conditions etc. are described for better understanding.

In chapter 5, numerical modeling of different studies are described. The finite volume method of discretisation, hybrid differencing scheme, staggered grid, SIMPLER algorithm, finite element method etc. are described in detail.

In chapter 6, the results found from different studies are graphically shown, tabulated and discussed. The results are described in terms of the convective heat transfer coefficient, Nusselt number, wall shear stress etc. of nanofluids. The particle size sensitivity of the mixture-phase model is also investigated. The results found from the numerical study of the nanofluid are

compared with an experimental result. In later sections, the improvement of solar efficiency for different nanofluids and riser tube fin configurations are described. Solar efficiencies calculated with constant and variable overall heat loss coefficient are compared.

Chapter 7 summarizes the results found from various studies. Some recommendations for future work are mentioned at the end.

Chapter 2

Literature Review

Heat transfer modes have its various applications in automotive engineering, nuclear engineering, electronic devices, insulation, materials processing, power station engineering etc. We need more and more efficient heat transfer fluids, more efficient energy conversion technologies, more and more energy sources. Heat exchanger is a very common and vastly used heat transfer device. Researchers are working on improving heat exchangers performance and recently nanofluids are being used as the working fluid of heat transfer devices.

2.1 Study of Nanofluids

Recent years have witnessed a blossom flourishing in the evolvement of electronics, communications, and auto computing industries, and this bearing is irrefutably continuing in this century. The cooling of electrical, mechanical, and electronic components has become troublesome in today's fast-growing technologies. Inasmuch as the significance of heat exchangers in tremendous engineering applications, the subject of potential heat transfer enhancement in these devices has received sizeable attention in practice and research. On account of the fact that the consistency of the electronic components commodiously increases, conspicuous lack of heat transfer enhancement both in macro- and microscales is realized. Encountering a fluid flow by utilizing transverse surfaces in a channel is a prevalent method that is used to intensify the rate of heat transfer from heated surfaces. Maxwell [1] showed the possibility of increasing thermal conductivity of a mixture by more volume fraction of solid particles in a fluid.

Masuda et al. reported an increase in thermal conductivity of liquid suspensions of γ-Al_2O_3, SiO_2 and TiO_2 nanoparticles [27]. In 1995, Choi studied the enhancement of thermal conductivity enhancement by suspending nanoparticles [6]. Early works on nanofluids were focused on determining the effective thermal conductivity and viscosity of nanofluids [28-29]. Lee et al. studied the enhancement of thermal conductivity for various metal oxide suspensions

[30]. These studies show that for a very little volume fraction of nanoparticles (say 1-5%), the thermal conductivity of the nanofluids may increase by about 20% more than the base fluid. These enhancements depend mainly on the nanoparticle size and form, volume concentration, thermal properties of both constituents etc. Hence, for efficient heat transfer, especially in micro and nano-scale, nanofluids appear to have very interesting application. Correlations were developed for effective conductivity and viscosity for various nanofluids as a function of base fluid properties and volume fraction of nanoparticles. In 2003, Das et al. experimentally investigated the temperature dependence of thermal conductivity of nanofluids [31]. Sadic et al. summarized the important published articles on forced convection heat transfer of nanofluids [32]. Research works on fluid flow and convective heat transfer characteristics of nanofluids in forced and free convection flows were reviewed by [33-35]. In 2011, Khnafer and Vafai have done a critical synthesis of the thermo-physical characteristics of nanofluids [36]. They have also synthesized and developed correlations for effective thermal conductivity and viscosity in terms of pertinent physical parameters based on the reported experimental data.

In 2004, Wen and Ding experimentally investigated the convection heat transfer of nanofluids in the entrance region under laminar flow conditions [37]. They found considerable enhancement of convection heat transfer and it was much higher than that of solely for the enhancement of thermal conduction. Possible reasons for the enhancement were reported to be nanoparticle migration, disturbance of the boundary layer etc. Heris et al. studied the convective heat transfer of alumina-water nanofluid [38]. They found much higher heat transfer coefficient than the prediction of single phase correlation. Heat transfer and flow behaviors of aqueous suspensions of TiO_2 and CNT nanofluids were studied experimentally by [39-40]. TiO_2 nanofluid study was done in a vertical pipe for both laminar and turbulent flows and the effect of particle concentration was more considerable for the turbulent flow regime. Heat transfer behavior of aqueous suspensions of multi-walled carbon nanotubes (CNT nanofluids) was studied in a horizontal tube. Significant enhancement of the convective heat transfer was observed and the enhancement depends on the Reynolds number, CNT concentration and the pH, with the effect of pH smallest. Chen et al. studied the heat transfer and flow behaviors of aqueous suspensions of titanate nanotubes [41]. They carried out experiments to investigate the effective thermal conductivity, rheological behaviour and forced convective heat transfer of the nanofluids. They found an excellent enhancement of the convective heat transfer coefficient, which is much higher than that of the thermal conductivity enhancement. They also demonstrated the important role of particle shape on heat transfer by comparing the results of nanofluids containing spherical titania nanoparticles with titanate nanofluids under similar conditions.

Numerous researches on nanfluids are found which are carried out using single-phase and two-phase approaches. In 2005, Maïga et al. investigated the laminar forced convection flow of nanofluids for two particular geometrical configurations, namely a uniformly heated tube and a system of parallel, coaxial and heated disks [42]. Among the two nanofluids studied, Ethylene

Glycol–Al_2O_3 nanofluid appears to offer a better heat transfer enhancement than water–Al_2O_3 nanofluid. Correlations have been provided for computing the Nusselt number of the nanofluids in terms of the Reynolds and the Prandtl numbers. Demir et al. studied the forced convection flows of nanofluids consisting of water with TiO_2 and Al_2O_3 nanoparticles in a horizontal tube with constant wall temperature [43]. Effects of nanoparticles concentration and Reynolds number on the wall shear stress, Nusselt number, heat transfer coefficient and pressure drops are presented. Rashmi et al. studied the natural convection heat transfer of Al_2O_3-water nanofluids using single-phase model [44]. They found a paradoxical behavior of decreasing heat transfer with increasing particle volume fraction for natural convection.

In the two-phase mixture modeling, the interactions between the phases are taken into account in the governing equations. In 2007, Behzadmehr et al. used a two-phase mixture model to study the turbulent nanofluid convection inside a circular tube [16]. Comparing with an experimental study they reported that the two-phase results are more precise than the homogeneous modeling (single-phase) results. Bianco et al. used both single and mixture model to study forced convection of nanofluids in circular tubes [15]. They found a maximum difference of 11% in the average heat transfer coefficient between the single and two phase model. They have also done a temperature dependent study of both models. Kalteh et al. studied the forced convection heat transfer of a copper–water nanofluid inside an isothermally heated microchannel [45]. They implemented Eulerian-Eulerian two-phase model to simulate the nanofluid flow inside the microchannel and the governing mass, momentum and energy equations were solved using finite volume method. The study showed that the relative velocity and temperature between the phases is very small and negligible and the nanoparticle concentration distribution is uniform. Laminar convection heat transfer of alumina-water nanofluid was studied both experimentally and numerically by [46]. The study showed that the maximum deviation from experimental results is 12.61% and 7.42% for homogeneous and two-phase methods respectively.

Buongiorno [17] theoretically developed a mixture model by considering slip mechanisms that can produce a relative velocity between the nanoparticles and the base fluid. The slip mechanisms considered were inertia, Brownian diffusion, thermophoresis, diffusiophoresis, Magnus effect, fluid drainage, and gravity. He found that only the Brownian diffusion and thermophoresis were the important slip mechanisms in nanofluids and based on the result, he proposed a two-component four-equation non-homogeneous equilibrium model for mass, momentum, and heat transport in nanofluids. Allahyari et al. studied the laminar mixed convection of alumina-water nanofluid in an inclined tube with heating at the top half surface of a copper tube [47]. The bottom half of the tube wall is assumed to be adiabatic (presenting a tube of a solar collector). They presented and discussed the change of hydrodynamic and thermal parameters with different volume fractions, Richardson numbers and tube inclinations. Sidik et al. studied the thermal performance of fins cooled either by water or alumina-water nanofluid in a channel by lattice Boltzmann method [48]. The results of the numerical simulation indicate that

the heat transfer rate of fins is significantly affected by the Reynolds number (Re) and the thermal conductivity of the fins. The influence of the solid volume fraction on the increase of heat transfer is more noticeable at higher values of the Re.

2.2 Performance Study of Flat Plate Collector (FPC)

Depletion of conventional energy resources and its adverse impact on environment have created renewed interest for the use of renewable energy resources. As a result, considerable research and development activities have taken place on how to extract solar energy reliably and economically. Solar thermal collector is a very well developed technology which collects the solar radiation and transfers it to a medium. Kalogirou have presented a detailed study on different solar collectors and their applications in 2004 [21]. An optical, thermal and thermodynamic analysis of the collectors and a description of the methods used to evaluate their performances were done. The most productive and low cost solar collectors are flat-plate type, but these types have comparatively low efficiency and outlet temperatures.

Attempts have been made to improve the thermal performance of conventional solar collectors by employing various design and flow arrangements. Manjunath et al. have done a comparative study on solar dimple plate collector with flat plate collector to augment the thermal performance [49]. They found a considerable increase in the average outlet temperature of the working fluid. Dović and Andrassy investigated the possibilities to improve the thermal performance of flat plate collector using a corrugated plate collector. Ramani et al. performed a theoretical and experimental study of double pass solar air collector with and without porous materials [50]. Their study showed a maximum of 35% enhancement of thermal performance of solar collector with double pass solar air collector with porous material. Thermal performance of solar collector with finned tubes was studied by [22]. Two types of fins were studied and both designs showed augmented thermal performance. Rassamakin et al. studied the flat plate solar collector made with Aluminum alloy made heat pipes with wide fins and longitudinal grooves [23]. The study showed that the thermal efficiency can be as high as 72% with these heat pipes. A review on recent developments on solar water heater using flat plate collector was done by Mathur et al. [51]. Developments involved use of double side absorber plate, honeycomb material, nano-material and more efficient coatings.

In recent times, researchers are investigating the possibility of using nanofluid as the working fluid of solar collectors because of the superior thermal properties of nanofluids. Applicability of nanofluids in direct solar energy absorption was studied by Ladjevardi et al. [52]. The study showed that with nanofluids, absorption of incident irradiation increases significantly. Tyagi et al. found an efficiency increase of 10% with direct absorption collector compared to the flat plate collector [53]. They used alumina-water nanofluid for the study. Because of the low cost and easy maintenance of flat plate collector, numerous experiments were

done with nanofluids on flat plate collector to improve its thermal performance. ASHRAE standard [54] was used to perform these tests with various nanofluids. In 2012, Yousefi et al. have studied the effects of alumina-water nanofluid on the efficiency of flat plate collector [55]. Jamal-Abad et al. have done an experiment with Cu-water nanofluid [56]. Their results showed that, the efficiency increases about 24% for 0.05 wt% of the nanofluid. Various surfactants and a degree of sonication were used in these studies to stabilize the nanofluids. Experimental investigation of the effect of pH variation of MWCNT-water nanofluid on the efficiency of flat plate collector was done by [57]. The experimental results showed that the more differences between the pH of nanofluid and pH of isoelectric point cause the more enhancement in the efficiency of the collector. Sambare and Prayagi have done a review work on the enhancement of thermal performance of solar collectors with nanofluids [58].

While there is plenty of experimental works, not much numerical works were found on flat plate collector with nanofluids in literature. In 2014, Nasrin and Alim have done a finite element simulation of forced convection in a flat plate collector using nanofluid with two nanoparticles [26]. The results show that, better performance of the flat plate solar collector is found by using the double nanoparticles (alumina and copper) than the single nanoparticle (only alumina). Effect of Prandtl number on the free convection in a solar collector was studied with Al_2O_3-water nanofluid by [59]. Tora and Moustafa numerically simulated the thermal performance of a flat plate collector with alumina-water nanofluid [60]. Their results showed good agreement with the experimental ones.

This thesis work numerically investigates the thermal performance of flat plate collector for different nanofluids and riser tube configurations. The results from the numerical work can be used to develop more and more efficient flat plate collector.

Chapter 3

Physical Model

This thesis work can be subdivided in three parts: (i) Nanofluid study in a circular pipe, (ii) Thermal performance study of flat plate collector with nanofluids, and (iii) Thermal performance study of flat plate collector with internally finned tubes. Physical models for these different studies are described in detail in the following sections.

3.1 Nanofluid Study Model

For the fluid flow and heat transfer study of nanofluid, a straight circular pipe like a riser tube of a solar collector of diameter 13.5 mm and length 1.5 m are considered. Following assumptions are made during the nanofluid study:

1. Incompressible flow
2. Axi-symmetric study
3. Steady-state flow
4. No external forces
5. Dilute solution ($\varphi \leq 0.05$)
6. Temperature independent properties

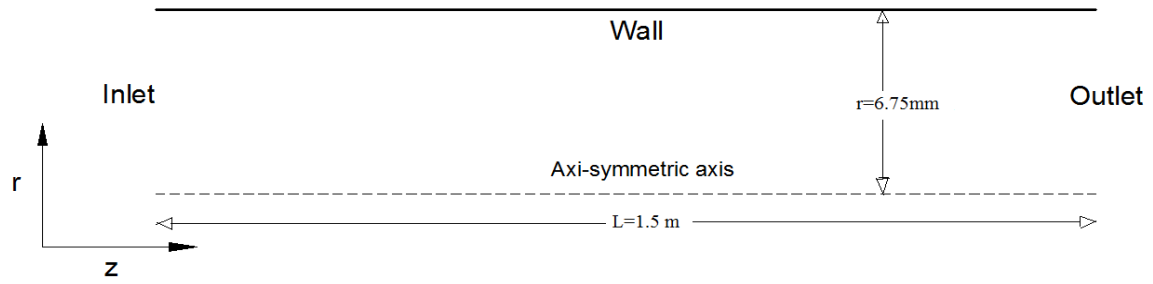

Fig. 3.1: Rectangular domain for nanofluid study

The axi-symmetric study assumption made the 3D circular pipe into a 2D rectangular domain as shown in the previous page in Fig. 3.1.

3.2 FPC with Nanofluid

For the study of flat plate collector with nanofluid, the absorber plate is of length 1.5 m and width 1.2 m. The absorber plate is made of copper and it has eight riser tubes attached to it. The riser tube material is also copper. Now, the absorber plate can be divided into eight identical parts of 150 mm width, each with one riser tube and these parts will have the same fluid flow and temperature profiles. For the numerical study, one part of these eight identical parts is considered as shown in Fig. 3.2. Detailed parameters of the flat plate collector model with nanofluid are given in table 3.1.

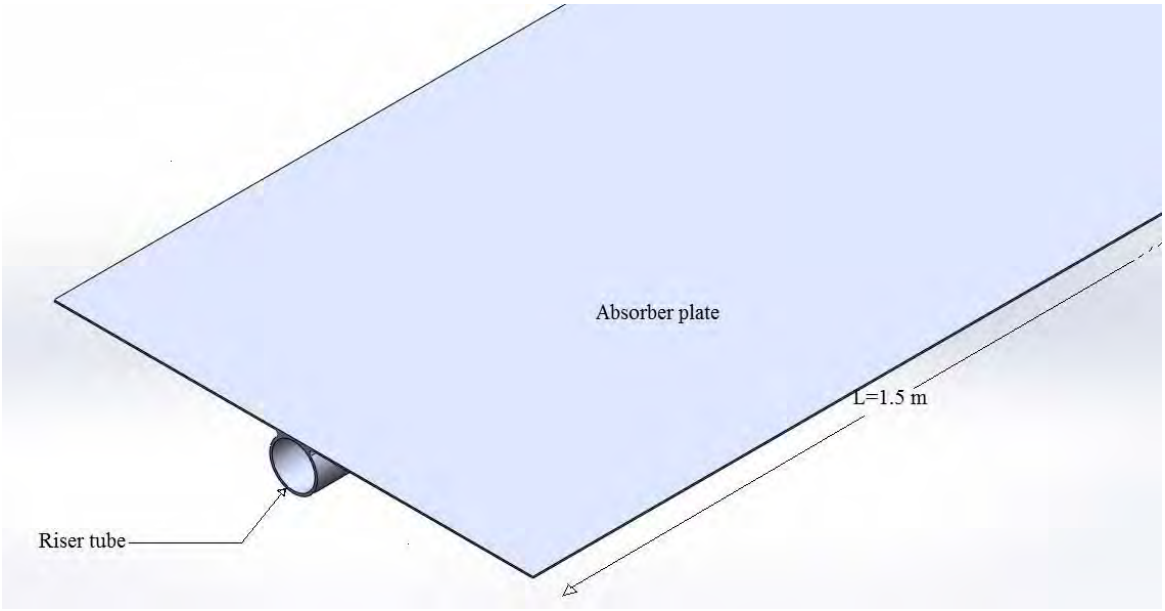

(a)

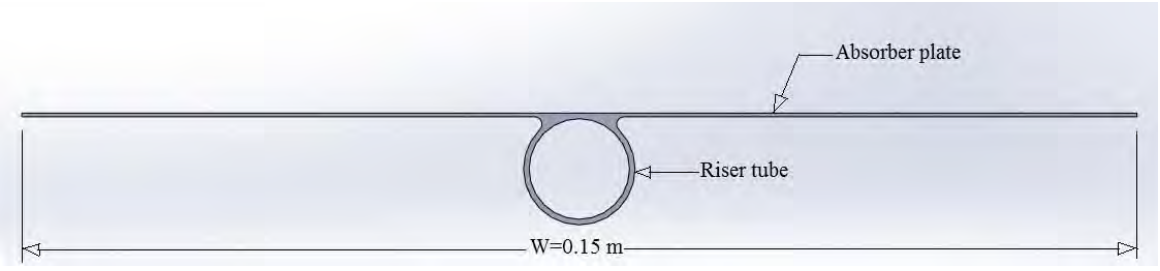

(b)

Fig. 3.2: (a) Isometric view, (b) Cross section view of the flat plate collector model

The assumptions of flat plate with nanofluid model are as following:

1. The collector is in steady state.
2. The collector is of the header and riser type fixed on a sheet with parallel tubes.
3. The headers cover only a small area of the collector and can be neglected.
4. Headers provide uniform flow to the riser tubes.
5. Temperature gradients around tubes are neglected.
6. Properties of materials are independent of temperature.
7. Heat flow through the absorber plate is two dimensional.
8. Fluid and heat flow through the riser pipe are axi-symmetric.

These assumptions make it possible to study the flat plate collector with a 2D absorber plate and a 2D riser pipe connected with heat transfer continuity.

Table 3.1: Solar collector model parameters

Absorber (L x W x H)	1500 x 150 x 0.5 mm^3
Glass cover	Highly transparent anti-reflection glass, transmission 95%
Absorber	Absorption 90%; emission 10%
Inner diameter of pipe	13.5 mm
Pipe thickness	0.75 mm
Material	Absorber, bonding and riser pipe are made of copper

3.3 FPC with Finned Tubes

To increase the thermal performance, flat plate collectors are also studied with internally finned tubes. The fins are attached to the inside surface of the riser tube and the other parameters are same as given in table 3.1. Two different fin configurations are considered in this thesis as shown in Fig. 3.3.

Fin-1 is of isosceles triangle shape that is arranged circumferentially to the pipe inner surface. There are a total of 18 fins and each 20 degree apart from each other. The length and width of the fin cross section is 1.5 mm and 0.8 mm respectively. Fin-2 configuration is of four thin rectangular segments which meets at the pipe centre and divides the pipe cross section into four equal sections. The rectangular segments are placed diagonally and each of width 0.6 mm.

The assumptions for this model are:

1. The collector is in steady state.
2. The collector is of the header and riser type fixed on a sheet with parallel tubes.

3. The headers cover only a small area of the collector and can be neglected.
4. Headers provide uniform flow to the riser tubes.
5. Properties of materials are independent of temperature.

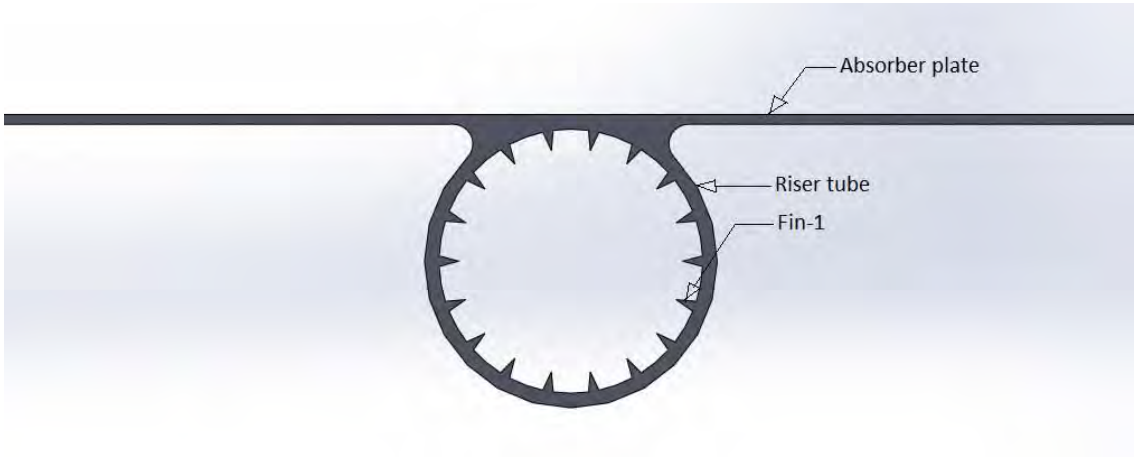

(a)

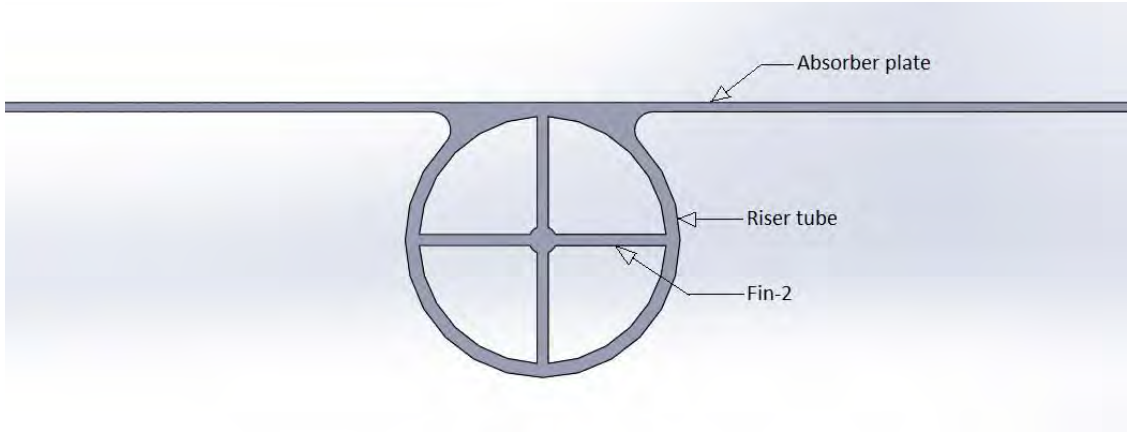

(b)

Fig. 3.3: (a) Fin-1, (b) Fin-2 configurations

Chapter 4

Mathematical Model

This thesis uses both single-phase and two-phase mixture model to study the nanofluid fluid flow and heat transfer. These both models are then used to investigate the thermal performance of flat plate collector with nanofluids. At last, flat plate collectors are investigated with finned tubes using FEM with water as the working fluid. All of these above studies require a mathematical model with appropriate governing equations and boundary conditions.

4.1 Governing Equations

The thesis requires various equations to govern the different models that are studied here. The governing equations used in this thesis are discussed in the following sections.

4.1.1 Continuity equation

From the principle of conservation of mass, the continuity equation is found as:

$$\frac{\partial \rho}{\partial t} + \nabla.(\rho \boldsymbol{u}) = 0 \tag{4.1}$$

where, ρ is fluid density, t is time, $\boldsymbol{u}$ is the flow velocity vector.

For the case of steady state and incompressible flow (ρ constant), the mass continuity equation simplifies to a volume continuity equation:

$$\nabla.(\boldsymbol{u}) = 0 \tag{4.2}$$

In cylindrical coordinate system (r,θ,z), the continuity equation becomes:

$$\frac{1}{r}\frac{\partial(ru_r)}{\partial r}+\frac{1}{r}\frac{\partial(u_\theta)}{\partial \theta}+\frac{\partial u_z}{\partial z}=0 \tag{4.3}$$

where, u_r, u_θ, u_z are the velocity components of $\boldsymbol{u}$.

4.1.2 Continuity Equation for Nanoparticle

For the two-phase study of nanofluid, this thesis uses the model given by J. Buongiorno [17]. For a nanofluid with φ volume fraction of nanoprticles, Buongiorno has developed a nanoparticle continuity equation as following:

$$\boldsymbol{u}.\nabla\varphi=\nabla.\left[D_B\nabla\varphi+D_T\frac{\nabla T}{T}\right] \tag{4.4}$$

Here, D_B represents the Brownian diffusion coefficient, given by the Einstein-Stokes's equation, and D_T represents the thermophoretic diffusion coefficient of the nanoparticles:

$$D_B=\frac{k_BT}{3\pi\mu d_{np}}$$

$$D_T=\left(\frac{0.26k}{2k+k_{np}}\right)\left(\frac{\mu}{\rho}\right)\varphi$$

where, k_B is the Boltzmann constant, d_{np} is particle diameter, k and k_{np} are the conductivities of the base fluid and nanoparticle respectively.

The two terms to the right of equation (4.4) is due to Brownian diffusion and thermophoresis. Brownian motion is proportional to the volumetric fraction of nanoparticles, in the direction from high to low concentration, whereas the thermophoresis is proportional to the temperature gradient, from hot to cold.

4.1.3 Momentum Equations

The general form of the equations which describe the fluid motion can be written as:

$$\frac{\partial(\rho\boldsymbol{u})}{\partial t}+\boldsymbol{u}.\nabla(\rho\boldsymbol{u})=-\nabla p+\nabla\boldsymbol{T}+\boldsymbol{f} \tag{4.5}$$

In the above equation, $\boldsymbol{u}$ is the fluid velocity vector, p is the flow pressure, $\boldsymbol{T}$ is the stress tensor and $\boldsymbol{f}$ is considered body forces caused by the outside environment. Body forces can be of various types and a common example of the body forces is the gravity force. In some circumstances, the body forces can be too large to be ignored, for example, electrified flow in an electric field. However, in most cases, gravity is the only body force and its influence to the fluid

motion is so small that normally it will be taken out of consideration. Furthermore, for steady-state, the transient term is taken out of the equation.

Thus, a simplified steady-state momentum equation for incompressible Newtonian flow is derived as:

$$\rho\mathbf{u}.\nabla\mathbf{u} = -\nabla p + \mu\nabla^2\boldsymbol{u} \tag{4.6}$$

where, μ is the constant viscosity of the fluid.

In cylindrical coordinate system (r,θ,z), the equations become:

r-momentum:

$$\rho\left(u_r\frac{\partial u_r}{\partial r} + \frac{u_\theta}{r}\frac{\partial u_r}{\partial\theta} - \frac{{u_\theta}^2}{r} + u_z\frac{\partial u_r}{\partial z}\right) = -\frac{\partial p}{\partial r} + \mu\left[\frac{\partial}{\partial r}\left(\frac{1}{r}\frac{\partial}{\partial r}(ru_r)\right) + \frac{1}{r^2}\frac{\partial^2 u_r}{\partial\theta^2} - \frac{2}{r^2}\frac{\partial u_\theta}{\partial\theta} + \frac{\partial^2 u_r}{\partial z^2}\right] \tag{4.7}$$

θ −momentum:

$$\rho\left(u_r\frac{\partial u_\theta}{\partial r} + \frac{u_\theta}{r}\frac{\partial u_\theta}{\partial\theta} + \frac{u_r u_\theta}{r} + u_z\frac{\partial u_\theta}{\partial z}\right) = -\frac{1}{r}\frac{\partial p}{\partial\theta} + \mu\left[\frac{\partial}{\partial r}\left(\frac{1}{r}\frac{\partial}{\partial r}(ru_\theta)\right) + \frac{1}{r^2}\frac{\partial^2 u_\theta}{\partial\theta^2} + \frac{2}{r^2}\frac{\partial u_r}{\partial\theta} + \frac{\partial^2 u_\theta}{\partial z^2}\right] \tag{4.8}$$

z-momentum:

$$\rho\left(u_r\frac{\partial u_z}{\partial r} + \frac{u_\theta}{r}\frac{\partial u_z}{\partial\theta} + u_z\frac{\partial u_z}{\partial z}\right) = -\frac{\partial p}{\partial z} + \mu\left[\frac{1}{r}\frac{\partial}{\partial r}\left(r\frac{\partial u_z}{\partial r}\right) + \frac{1}{r^2}\frac{\partial^2 u_z}{\partial\theta^2} + \frac{\partial^2 u_z}{\partial z^2}\right] \tag{4.9}$$

4.1.4 Energy Equation

Energy equation can be written in many different ways, one such form is given below:

$$\rho\left[\frac{\partial h}{\partial t} + \boldsymbol{u}.\nabla\mathrm{h}\right] = -\frac{Dp}{Dt} + \nabla.(k\nabla T) + S \tag{4.10}$$

where, h is the specific enthalpy, T is the absolute temperature, S is the source term. Source could be electrical energy due to current flow, chemical energy, nuclear energy etc.

Pressure term on the right side of equation (4.10) is usually neglected. The equation given can be simplified considering $h = c_p T$ and taking c_p and k constant. So, the steady-state, incompressible flow energy equation takes the following form:

$$\rho c_p[\boldsymbol{u}.\nabla T] = k\nabla^2\mathrm{T} \tag{4.11}$$

here, the source term is considered zero.

For the nanofluid mixture model [17], two additional terms are added to equation (4.11) for Brownian diffusion and thermophoresis. The energy equation for nanofluid mixture model is as following:

$$\rho c_p[\boldsymbol{u}.\nabla T] = k\nabla^2\mathrm{T} + \rho_{np}c_{np}\left[D_B\nabla\varphi.\nabla T + D_T\frac{\nabla T.\nabla T}{T}\right] \tag{4.12}$$

The two additional terms on the right side of equation (4.12) comes due to the heat transfer by virtue of nanoparticle diffusion. It is important to note that ρc_p is the heat capacity of the nanofluid and $\rho_{np}c_{np}$ is the heat capacity of the nanoparticle.

4.1.5 Conduction Equation

The steady-state governing equation for conduction heat transfer is as following:

$$k\nabla^2 T + S = 0 \tag{4.13}$$

The conduction equation is used to find the temperature distribution of the absorber plate of the flat plate solar collector. With the assumption of heat flow along the thickness of a flat absorber plate is negligible, conduction equation for absorber plate becomes two-dimensional. The source term S here then would be the amount of solar heat absorbed minus the amount of heat lost to the environment by per unit volume of the collector. If energy absorbed by per unit area of the plate is $I_t(\tau\alpha)$ and the overall heat loss coefficient is U_L, then the source term S can be written as:

$$S = \frac{I_t(\tau\alpha)}{t} - \frac{U_L(\mathrm{T} - \mathrm{T}_\alpha)}{t} \tag{4.14}$$

where, I_t is the solar irradiation, τ is the transmittance of the glass cover, α is the absorptivity of the collector plate, T_α is the ambient temperature and t is the plate thickness.

The study is done using both constant and variable values of overall heat loss coefficient, $\mathrm{U_L}$. The overall heat loss coefficient, $\mathrm{U_L}$ is a complicated function of collector construction and its operating conditions and is given by the following equation:

$$U_L = U_t + U_b + U_e \tag{4.15}$$

The top heat loss coefficient, $\mathrm{U_t}$ in equation (4.15) is given by [61].

$$U_t = \frac{1}{\frac{N_g}{\frac{C}{T_p}\left[\frac{T_{av}-T_\alpha}{N_g+f}\right]^{0.33}+\frac{1}{h_w}}} + \frac{\sigma(T_{av}^2+T_\alpha^2)(T_{av}+T_\alpha)}{\frac{1}{\varepsilon_p+0.05N_g(1-\varepsilon_p)}+\frac{2N_g+f-1}{\varepsilon_g}-N_g} \quad (4.16)$$

where, $h_w = 5.7 + 3.5W$

$$f = (1 - 0.04h_w + 0.0005h_w^2)\left(1 + 0.091N_g\right)$$

$$C = 365.9(1 - 0.00883\beta + 0.0001298\beta^2)$$

T_p is the collector stagnation temperature, i.e. the absorber temperature when the flow rate is zero and is given by:

$$T_p = \frac{I_t(\tau\alpha)}{U_L} + T_\alpha$$

And ε is the infrared emissivity, N_g is the number of glass covers, σ is the Plank's constant, and β is the solar plate inclination angle in degree.

The heat loss coefficient for the bottom and edges, U_b and U_e are constant and barely exceeds 10% of the upward loss.

If the study is done in 3D as for the solar collector with finned tubes, then source term, S would be zero and the value of St would be given as the heat flux at the top face of the collector.

4.2 Single-phase Model

For the study of single-phase model of nanofluid, the continuity, momentum and energy equations can be solved as if the fluid is a classical Newtonian fluid by using effective properties of nanofluid. Effective properties are functions of particle size (d_{np}), type, shape, particle volume concentration (φ), and temperature.

With the assumption of axi-symmetric fluid and heat flow, the governing equations for single phase model can be written from equation (4.3), (4.7), (4.8), (4.9) and (4.11).

Continuity equation:

$$\frac{1}{r}\frac{\partial(ru_r)}{\partial r} + \frac{\partial u_z}{\partial z} = 0 \quad (4.17)$$

Momentum equations:

r-momentum:

$$\rho\left[\frac{1}{r}\frac{\partial}{\partial r}(ru_r u_r)+\frac{\partial}{\partial z}(u_z u_r)\right]=-\frac{\partial p}{\partial r}+\mu\left[\frac{\partial}{\partial r}\left(\frac{1}{r}\frac{\partial}{\partial r}(ru_r)\right)+\frac{\partial^2 u_r}{\partial z^2}\right] \quad (4.18)$$

z-momentum:

$$\rho\left[\frac{1}{r}\frac{\partial}{\partial r}(ru_r u_z)+\frac{\partial}{\partial z}(u_z u_z)\right]=-\frac{\partial p}{\partial z}+\mu\left[\frac{1}{r}\frac{\partial}{\partial r}\left(r\frac{\partial u_z}{\partial r}\right)+\frac{\partial^2 u_z}{\partial z^2}\right] \quad (4.19)$$

Energy equation:

$$\rho c_p\left[\frac{1}{r}\frac{\partial}{\partial r}(ru_r T)+\frac{\partial}{\partial z}(u_z T)\right]=k\left[\frac{1}{r}\frac{\partial}{\partial r}\left(r\frac{\partial T}{\partial r}\right)+\frac{\partial^2 T}{\partial z^2}\right] \quad (4.20)$$

Boundary conditions of this model are as following:

1. Normal inflow velocity and constant temperature at inlet.
2. Fully developed flow and zero pressure at outlet.
3. No slip condition and constant heat flux at wall.

4.3 Two-phase Mixture Model

This thesis utilizes the mixture model given by Buongiorno [17] for the two-phase study of nanofluid. Buongiorno has developed a two component four equation nonhomogenous mixture model for nanofluid.

With the axi-symmetric assumption, the governing equations (4.17)-(4.19) of single-phase model are directly applicable to this model. Another two equations for this model can be found from equation (4.4) and (4.12).

Continuity equation of nanoparticle:

$$\frac{1}{r}\frac{\partial}{\partial r}(ru_r\varphi)+\frac{\partial}{\partial z}(u_z\varphi) = \left[\frac{1}{r}\frac{\partial}{\partial r}\left(rD_B\frac{\partial\varphi}{\partial r}\right)+\frac{\partial}{\partial z}\left(D_B\frac{\partial\varphi}{\partial z}\right)\right]+\left[\frac{1}{r}\frac{\partial}{\partial r}\left(r\frac{D_T}{T}\frac{\partial T}{\partial r}\right)+\frac{\partial}{\partial z}\left(\frac{D_T}{T}\frac{\partial T}{\partial z}\right)\right] \quad (4.21)$$

Energy equation of nanofluid:

$$\rho c_p \left[\frac{1}{r}\frac{\partial}{\partial r}(r u_r T) + \frac{\partial}{\partial z}(u_z T)\right] = k\left[\frac{1}{r}\frac{\partial}{\partial r}\left(r\frac{\partial T}{\partial r}\right) + \frac{\partial^2 T}{\partial z^2}\right] + \rho_{np} c_{np}\left[D_B\left(\frac{\partial \varphi}{\partial r}\frac{\partial T}{\partial r} + \frac{\partial \varphi}{\partial z}\frac{\partial T}{\partial z}\right) + \frac{D_T}{T}\left(\frac{\partial T}{\partial r}\frac{\partial T}{\partial r} + \frac{\partial T}{\partial z}\frac{\partial T}{\partial z}\right)\right] \quad (4.22)$$

Boundary conditions:

1. Normal inflow velocity and constant temperature at inlet.
2. Fully developed flow and zero pressure at outlet.
3. No slip condition and constant heat flux at wall.
4. Zero nanoparticle mass flux at wall.

4.4 FPC with Nanofluid Model

Flat plate collector is investigated using both single-phase and mixture model of nanofluid. So the governing equations of flat plate collector model comprise that of single-phase model and mixture model of nanofluid and an additional conduction equation for the absorber plate.

The 2D governing equation for the absorber plate can be written from equation (4.13) and (4.14) as following:

$$k\left[\frac{\partial T^2}{\partial y^2} + \frac{\partial T^2}{\partial z^2}\right] + \frac{\mathrm{I_t}(\tau\alpha)}{t} - \frac{U_L(\mathrm{T} - \mathrm{T_\alpha})}{t} = 0 \quad (4.23)$$

Boundary conditions:

1. at inlet of riser pipe: $T = T_{in}$, $\boldsymbol{u} = U_{in}$
2. at outlet: convective boundary condition, $p = 0$
3. at side walls of absorber: No heat flux
4. at riser wall: $\boldsymbol{u} = 0$
5. at the solid-fluid interface: continuity $k_f\left(\frac{\partial T}{\partial n}\right)_f = k_a\left(\frac{\partial T}{\partial n}\right)_{absorber}$

4.5 FPC with Finned Tubes

Analysis of the flat plate collector with internally finned riser tubes requires 3D investigation as the fluid and heat flow in the riser are not axi-symmetric this time. So, the governing equations of this model are three-dimensional.

Equation (4.2), (4.6) and (4.11) are the three governing equations of this model. Now, the governing equation for absorber plate can be written from equation (4.13) with S=0:

$$k\nabla^2 T = 0 \tag{4.24}$$

Boundary conditions:

1. at inlet of riser pipe: $T = T_{in}$, $\boldsymbol{u} = U_{in}$
2. at outlet: convective boundary condition, $p = 0$
3. at the top wall of absorber: heat flux, $q = St = I_t(\tau\alpha) - U_L(\mathrm{T} - \mathrm{T}_\alpha)$
4. at bottom and side walls of absorber: No heat flux
5. at outer part of bonding and pipe: insulation
6. at riser wall: $\boldsymbol{u} = 0$
7. at the solid-fluid interface: continuity $k_f \left(\frac{\partial T}{\partial n}\right)_f = k_a \left(\frac{\partial T}{\partial n}\right)_{absorber}$

4.6 Thermo-Physical Properties of Nanofluid

The determination of nanofluid properties is very important as the results of the numerical study depend on these properties. Various researchers have studied the increase of thermal conductivity and viscosity for small volume percentages of nanoparticles. The other thermophysical properties used in this study are density and specific heat.

Density: The nanofluid density is the average of the nanoparticle and base fluid densities:

$$\rho_{nf} = \varphi\rho_{np} + (1 - \varphi)\rho_{bf} \tag{4.25}$$

where, the subscripts nf, p and bf refer to the nanofluids, nanoparticles and base fluid respectively.

Specific Heat: The effective specific heat of nanofluid can be calculated by the following equation as reported in [28, 42].

$$c_{nf} = \varphi c_{np} + (1 - \varphi)c_{bf} \tag{4.26}$$

Viscosity: Different researchers have studied to calculate the effective viscosity of different nanofluids [27, 30]. Nguyen et al. [62] proposed the following correlations for Al_2O_3-water and CuO-water nanofluid as given in equation (4.25) and (4.26).

$$\mu_{nf} = 0.904e^{14.82\varphi}\mu_{bf} \qquad for\ Al_2O_3 - water\ nanofluid \quad (4.27)$$

$$\mu_{nf} = \mu_{bf}(1.475 - 31.9\varphi + 510\varphi^2 + 9000\varphi^3) \qquad for\ CuO - water\ nanofluid \quad (4.28)$$

Thermal Conductivity: Various correlations by different researchers can be found for the effective conductivity of different nanofluids [27-28, 37]. The thermal conductivity given by Pak and Cho [37] for Al_2O_3-water nanofluid and the conductivity found by Eastman et al. [63] for CuO-water nanofluid are used in this study which can be correlated as follows:

$$k_{nf} = k_{bf}(1 + 7.47\varphi) \qquad for\ Al_2O_3 - water\ nanofluid \quad (4.29)$$

$$k_{nf} = k_{bf}(1 + 11.9\varphi) \qquad for\ CuO - water\ nanofluid \quad (4.30)$$

The nanofluid study is done for various Reynolds number and volume fraction at constant inlet temperature of 293 K.

The thermo-physical properties of Al_2O_3 nanoparticle are:

$$\rho_{np} = 3880\ kg/m^3\ ; \quad c_{np} = 733\ J/kg.K$$

The thermo-physical properties of CuO nanoparticle are:

$$\rho_{np} = 6310\ kg/m^3\ ; \quad c_{np} = 550.5\ J/kg.K$$

The thermo-physical properties of water are:

$$\rho = 998.2\ kg/m^3\ ; \quad c_p = 4182\ J/kg.K\ ; \quad k = 0.597\ W/m.K$$

Chapter 5

Numerical Modeling

After defining a physical model with governing equations, the toughest part of the study is to solve the governing equations to get the desired results. Numerical methods typically transform the differential equations governing a continuum, to a set of algebraic equations of a discrete model of the continuum that can be solved easily. There are various methods (FDM, FEM, FVM etc.) that are used to transform these differential equations into algebraic equations. In this study, FVM method is used to discretise the governing equations of single-phase model, mixture model, and solar plate with nanofluid models. For the solar plate model with finned tubes, FEM method is used.

5.1 Finite Volume Method

The finite volume method (FVM) is a method of discretising partial differential equations to algebraic equations [64]. For the finite volume method, the usual approach is to divide the physical space into many small sub-domains which are called control volumes or cells. The shape of cells can be arbitrary while triangular cell and rectangular cell are the most popular two types. The partial differential equations are recast on these cells and approximated by the nodal values or central values of the control volumes.

In the finite volume method, volume integrals in a partial differential equation that contain a divergence term are converted to surface integrals, using the divergence theorem. Divergence theorem can be mathematically stated as:

$$\oint_V (\nabla . \boldsymbol{F}) dV = \oint_s (\boldsymbol{F} . \boldsymbol{n}) dS \tag{5.1}$$

Theoretically, the volume can be any arbitrary shape. For the polygonal of Fig. 5.1, above equation can be recast as:

$$\oint_V (\nabla . \boldsymbol{F}) dV = \oint_s (\boldsymbol{F} . \boldsymbol{n}) dS = \sum_i (\boldsymbol{F} . \boldsymbol{n_i}) \Delta S_i \quad (5.2)$$

where, $\boldsymbol{n_i}$ represents the outward unit normal vector of the face $\boldsymbol{i}$ of the volume and ΔS_i stands for the surface area of the face $\boldsymbol{i}$.

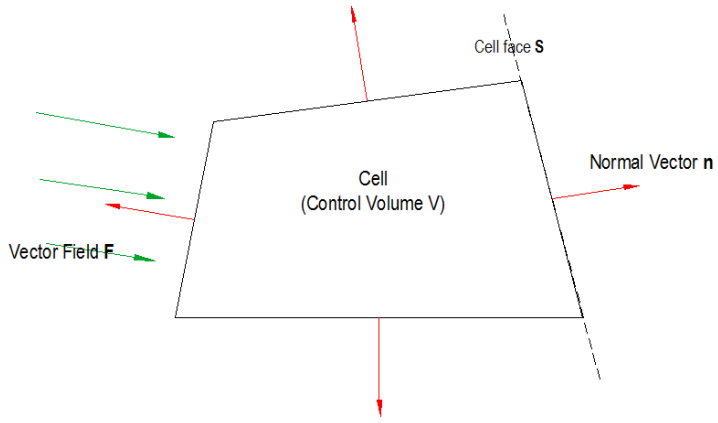

Fig. 5.1: A typical polygonal cell

5.1.1 Discretisation of Energy Equation

The steady-state energy equation for axi-symmetric flow is given by equation (4.20):

$$\frac{1}{r}\frac{\partial}{\partial r}(r u_r T) + \frac{\partial}{\partial z}(u_z T) = \alpha \left[\frac{1}{r}\frac{\partial}{\partial r}\left(r\frac{\partial T}{\partial r}\right) + \frac{\partial^2 T}{\partial z^2}\right] \quad (5.3)$$

here, $\alpha = \frac{k}{\rho c_p}$

For discretising of the above equation, structured grids are used as given in Fig. 5.2 [65]. A general nodal point is identified as P and its neighbors in a two-dimensional geometry, the nodes to the west, east, north and south are identified by W, E, N and S respectively. The west side face of the control volume is referred to by w and the east, north and south side face are referred by e, n and s respectively. The distance between west and east face and between north and south face are denoted by Δz and Δr respectively. Now the key step is the integration of the differential equation over the control volume to yield a discretised equation at its nodal point P.

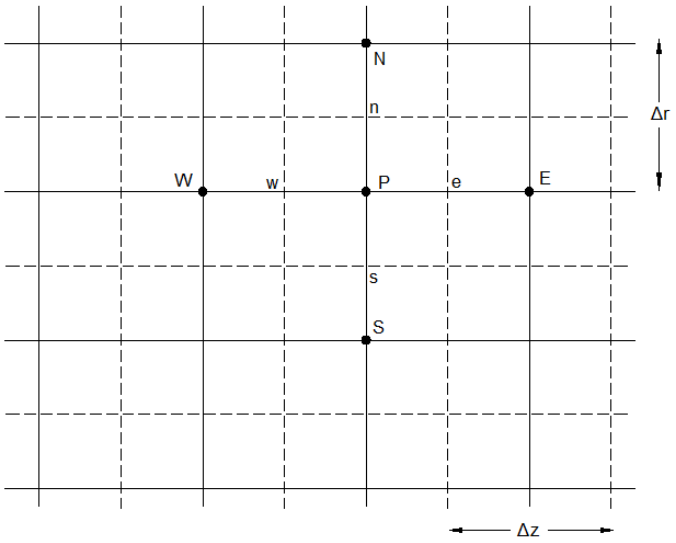

Fig. 5.2: Grid in cylindrical coordinate system

Integration of the transport equation (5.3) over the control volume of nodal point P gives:

$$\int \frac{1}{r}\frac{\partial}{\partial r}(ru_rT)rdrdz + \int \frac{\partial}{\partial z}(u_zT)\,rdrdz = \int \alpha\frac{1}{r}\frac{\partial}{\partial r}\left(r\frac{\partial T}{\partial r}\right)rdrdz + \int \alpha\frac{\partial^2 T}{\partial z^2}rdrdz \quad (5.4)$$

or,

$$(ru_rT\Delta z)_n - (ru_rT\Delta z)_s + (u_zTr\Delta \mathrm{r})_e - (u_zTr\Delta \mathrm{r})_w = \left(\alpha\frac{\partial T}{\partial r}r\Delta z\right)_n - \left(\alpha\frac{\partial T}{\partial r}r\Delta z\right)_s + \left(\alpha\frac{\partial T}{\partial z}r\Delta r\right)_e - \left(\alpha\frac{\partial T}{\partial z}r\Delta r\right)_w \quad (5.5)$$

Now for a structured grid,

$$\left(\alpha\frac{\partial T}{\partial r}r\Delta z\right)_n = \alpha r_n\Delta z\frac{T_N - T_P}{\Delta r}$$

$$\left(\alpha\frac{\partial T}{\partial r}r\Delta z\right)_s = \alpha r_s\Delta z\frac{T_P - T_S}{\Delta r}$$

$$\left(\alpha\frac{\partial T}{\partial z}r\Delta r\right)_e = \alpha r_e\Delta r\frac{T_E - T_P}{\Delta z}$$

$$\left(\alpha\frac{\partial T}{\partial z}r\Delta r\right)_w = \alpha r_w\Delta r\frac{T_P - T_W}{\Delta z}$$

It is convenient to define new variables as following:

$$F_n = (ru_r\Delta z)_n, \quad F_s = (ru_r\Delta z)_s, \quad F_e = (ru_z\Delta r)_e, \quad F_w = (ru_z\Delta r)_w$$

and,

$$D_n = \frac{\alpha r_n \Delta z}{\Delta r}, \quad D_s = \frac{\alpha r_s \Delta z}{\Delta r}, \quad D_e = \frac{\alpha r_e \Delta r}{\Delta z}, \quad D_w = \frac{\alpha r_w \Delta r}{\Delta z}$$

The integrated energy equation can now be written as:

$$F_nT_n - F_sT_s + F_eT_e - F_wT_w = D_n(T_N - T_P) - D_s(T_P - T_S) + D_e(T_E - T_P) - D_w(T_P - T_W) \qquad (5.6)$$

To solve the above equation, we need to determine the transported property T at the control volume faces. Various schemes for this purpose are assessed in the following section.

5.1.1.1 Differencing Schemes

Central Differencing Scheme: To calculate the cell face values, central differencing scheme uses linear interpolation. Using linear interpolation for the uniform grid of Fig. 5.2, we can write

$$T_n = (T_N + T_P)/2, \qquad T_s = (T_P + T_S)/2$$

$$T_e = (T_E + T_P)/2, \qquad T_w = (T_P + T_W)/2$$

Central differencing scheme is stable and accurate for small cell Peclet numbers. One major inadequacy is that it does not recognize the direction of the flow or the strength of convection relative to diffusion.

Upwind Differencing Scheme: The upwind differencing scheme takes into account the flow direction when determining the value at a cell face: the value of T at a cell face is taken to be equal to the value at the upstream node. When the flow is in the positive direction, $u_s>0$, $u_n>0$, $u_w>0$, $u_e>0$, the upwind scheme sets,

$$T_s = T_S, \quad T_n = T_P, \quad T_w = T_W \ \ and \quad T_e = T_P$$

When the flow is in the negative direction, $u_s<0$, $u_n<0$, $u_w<0$, $u_e<0$, the upwind scheme sets,

$$T_s = T_P, \quad T_n = T_N, \quad T_w = T_P \ \ and \quad T_e = T_E$$

The accuracy of upwind scheme is of first order whereas the accuracy of central differencing is of second order.

Hybrid Differencing Scheme: The hybrid differencing scheme of Spalding [66] is based on a combination of central and upwind differencing schemes. The central differencing scheme is employed for small Peclet numbers and the upwind scheme is used for large Peclet numbers. Now Peclet number is evaluated at the face of the control volume. For example, for a west face,

$$Pe_w = \frac{F_w}{D_w} = \frac{(ru_z\Delta r)_w}{\alpha r_w \Delta r/\Delta z} \tag{5.7}$$

The hybrid differencing formula for T_w is as follows:

$$\begin{aligned} T_w &= \frac{1}{2}\left(1+\frac{2}{Pe_w}\right)T_W + \frac{1}{2}\left(1-\frac{2}{Pe_w}\right)T_P \qquad for -2 < Pe_w < 2 \\ T_w &= T_W \qquad for\ Pe_w \geq 2 \\ T_w &= T_P \qquad for\ Pe_w \leq -2 \end{aligned} \tag{5.8}$$

In this study, hybrid differencing scheme is used. After applying the hybrid scheme for the face values of T in equation (5.6), the equation becomes:

$$a_P T_P = a_N T_N + a_S T_S + a_E T_E + a_W T_W \tag{5.9}$$

The central coefficient is given by

$$a_P = a_N + a_S + a_E + a_W + (F_n - F_s) + (F_e - F_w)$$

where,

$$a_N = max\left[-F_n, \left(D_n - \frac{F_n}{2}\right), 0\right], \qquad a_S = max\left[F_s, \left(D_s + \frac{F_s}{2}\right), 0\right]$$

$$a_E = max\left[-F_e, \left(D_e - \frac{F_e}{2}\right), 0\right], \qquad a_W = max\left[F_w, \left(D_w + \frac{F_w}{2}\right), 0\right]$$

5.1.2 Flow Field

The convection of a scalar variable like temperature depends on the magnitude and direction of the local velocity field. The velocity field can be obtained by solving the momentum equations. The momentum equations also must satisfy the continuity equation. The continuity and momentum equations for incompressible axi-symmetric steady flow are found in equation (4.17), (4.18) and (4.19).

Continuity equation:

$$\frac{1}{r}\frac{\partial(ru_r)}{\partial r}+\frac{1}{r}\frac{\partial(u_\theta)}{\partial \theta}+\frac{\partial u_z}{\partial z}=0$$

r-momentum equation:

$$\rho\left[\frac{1}{r}\frac{\partial}{\partial r}(ru_ru_r)+\frac{\partial}{\partial z}(u_zu_r)\right]=-\frac{\partial p}{\partial r}+\mu\left[\frac{\partial}{\partial r}\left(\frac{1}{r}\frac{\partial}{\partial r}(ru_r)\right)+\frac{\partial^2 u_r}{\partial z^2}\right]$$

z-momentum equation:

$$\rho\left[\frac{1}{r}\frac{\partial}{\partial r}(ru_ru_z)+\frac{\partial}{\partial z}(u_zu_z)\right]=-\frac{\partial p}{\partial z}+\mu\left[\frac{1}{r}\frac{\partial}{\partial r}\left(r\frac{\partial u_z}{\partial r}\right)+\frac{\partial^2 u_z}{\partial z^2}\right]$$

The solution of the above three equations are problematic for following reasons:

- The convective term of the momentum equations contain non-linear quantities.
- All three equations are intricately coupled because every velocity component appears in every equation. Again pressure appears in both momentum equations, but evidently there is no equation for pressure.

Both the problems associated with the non-linearities and the pressure-velocity linkage is solved by adopting the iterative solution strategy of SIMPLER algorithm [67] which will be discussed in detail in later sections.

5.1.2.1 Staggered Grids

During discretisation of the flow equations, the first question is where to store the velocities. If the velocities and pressures are both defined at the nodes of an ordinary control volume, a highly non-uniform pressure field can act like a uniform field in the discretised momentum equations. This problem can be solved by using staggered grid [68] for the velocity components. This way, scalar variables like pressure, density, temperature etc. are evaluated at ordinary nodal points but velocity components are calculated on staggered grids centered around the cell faces. A further advantage of staggered grid arrangement is that it generates velocities at exactly the locations where they are required for the solution of the discretized energy equations or other scalar transport equations. The arrangement for a two-dimensional staggered grid is shown in Fig. 5.3. The scalar variables, including pressure are stored at the nodes marked (•). The velocities are defined at the (scalar) cell faces in between the nodes and are indicated by arrows. The control volumes for u_r and u_z are different from the scalar control volume and different from each other.

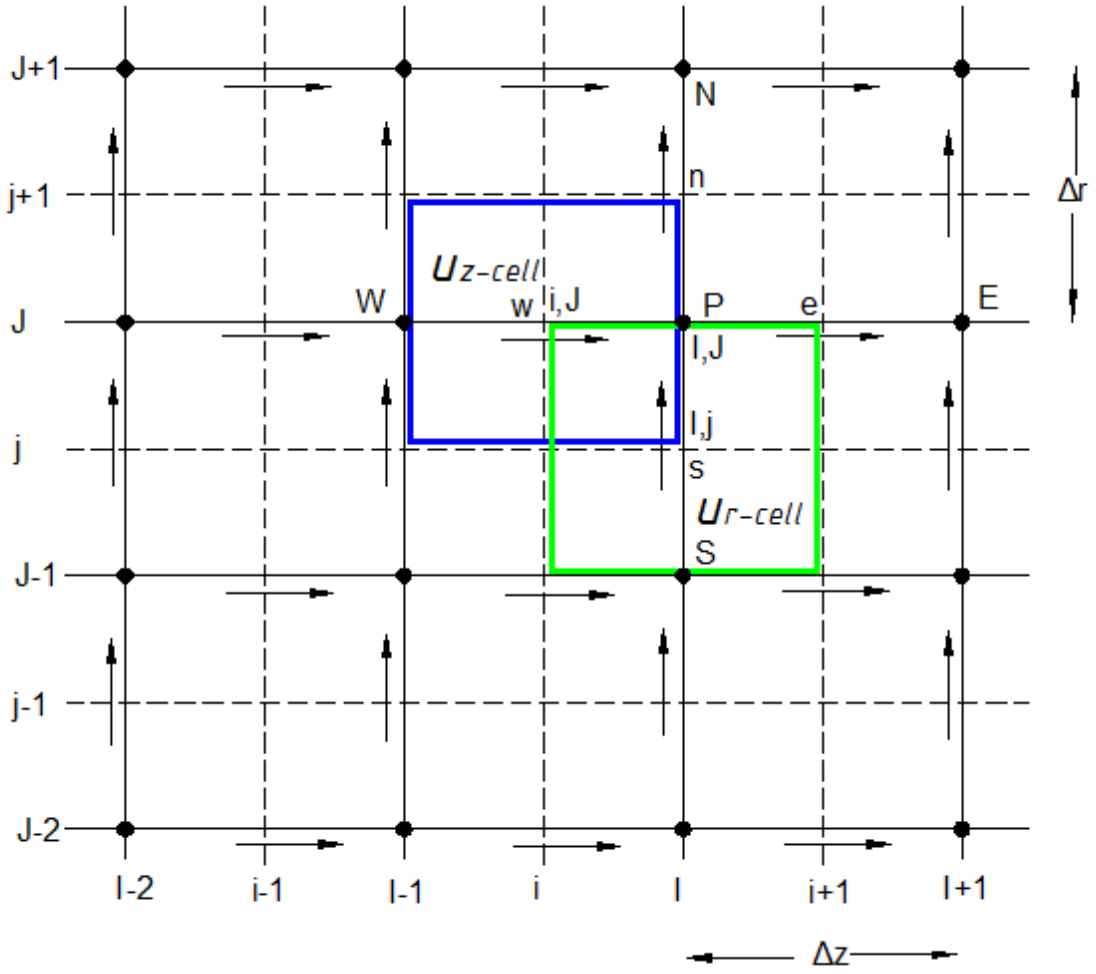

Fig. 5.3: Staggered Grid

For the staggered grid, a new notation based on grid line and cell face numbering is used. In Fig. 5.3, the unbroken grid lines are numbered by capital letters. In the z-direction, the numbering is ….., I-1, I, I+1, …. etc. and in the r-direction is …., J-1, J, J+1, … etc. The dashed lines that construct the scalar cell faces are denoted by lower case letters …., i-1, i, i+1, … and …., j-1, j, j+1, … in the z- and r-direction respectively. Backward staggered velocity grid is used in this study.

5.1.2.2 Discretised Flow Equations

r-momentum: Integration of the r-momentum equation over the u_r control volume (shown in Fig. 5.3) gives the following final form:

$$a_p u_{r_{I,j}} = a_n u_{r_{I,j+1}} + a_s u_{r_{I,j-1}} + a_e u_{r_{I+1,j}} + a_w u_{r_{I-1,j}} + \left(P_{I,J-1} - P_{I,J}\right) r_j \Delta z \qquad (5.10)$$

where,

$$a_p = a_n + a_s + a_e + a_w + (F_n - F_s) + (F_e - F_w) + \mu\, ln\frac{r_J}{r_{J-1}}\Delta z$$

$$a_n = max\left[-F_n, \left(D_n - \frac{F_n}{2}\right), 0\right], \quad a_s = max\left[F_s, \left(D_s + \frac{F_s}{2}\right), 0\right]$$

$$a_e = max\left[-F_e, \left(D_e - \frac{F_e}{2}\right), 0\right], \quad a_w = max\left[F_w, \left(D_w + \frac{F_w}{2}\right), 0\right]$$

$$F_n = \frac{\rho\Delta z}{2}\left[r_{j+1}u_{r_{I,j+1}} + r_j u_{r_{I,j}}\right], \quad F_s = \frac{\rho\Delta z}{2}\left[r_j u_{r_{I,j}} + r_{j-1}u_{r_{I,j-1}}\right]$$

$$F_e = \frac{\rho r_j\Delta r}{2}\left[u_{z_{i+1,J}} + u_{z_{i+1,J-1}}\right], \quad F_w = \frac{\rho r_j\Delta r}{2}\left[u_{z_{i,J}} + u_{z_{i,J-1}}\right]$$

$$D_n = \mu\frac{r_J\Delta z}{\Delta r}, \quad D_s = \mu\frac{r_{J-1}\Delta z}{\Delta r}, \quad D_e = D_w = \mu\frac{r_j\Delta r}{\Delta z}$$

z-momentum: Integration of the z-momentum equation over the u_z control volume (shown in Fig. 5.3) gives the following final form:

$$a_p u_{z_{i,J}} = a_n u_{z_{i,J+1}} + a_s u_{z_{i,J-1}} + a_e u_{z_{i+1,J}} + a_w u_{z_{i-1,J}} + \left(P_{I-1,J} - P_{I,J}\right)r_J\Delta r \qquad (5.11)$$

where,

$$a_p = a_n + a_s + a_e + a_w + (F_n - F_s) + (F_e - F_w)$$

$$a_n = max\left[-F_n, \left(D_n - \frac{F_n}{2}\right), 0\right], \quad a_s = max\left[F_s, \left(D_s + \frac{F_s}{2}\right), 0\right]$$

$$a_e = max\left[-F_e, \left(D_e - \frac{F_e}{2}\right), 0\right], \quad a_w = max\left[F_w, \left(D_w + \frac{F_w}{2}\right), 0\right]$$

$$F_n = \frac{\rho r_{j+1}\Delta z}{2}\left[u_{r_{I,j+1}} + u_{r_{I-1,j+1}}\right], \quad F_s = \frac{\rho r_j\Delta z}{2}\left[u_{r_{I,j}} + u_{r_{I-1,j}}\right]$$

$$F_e = \frac{\rho r_J\Delta r}{2}\left[u_{z_{i+1,J}} + u_{z_{i,J}}\right], \quad F_w = \frac{\rho r_J\Delta r}{2}\left[u_{z_{i,J}} + u_{z_{i-1,J}}\right]$$

$$D_n = \mu\frac{r_{j+1}\Delta z}{\Delta r}, \quad D_s = \mu\frac{r_j\Delta z}{\Delta r}, \quad D_e = D_w = \mu\frac{r_J\Delta r}{\Delta z}$$

Continuity: Integration of the continuity equation over the scalar control volume surrounding nodal point P (in Fig. 5.3) gives the following final form:

$$\left(r_{j+1}u_{r_{I,j+1}} - r_j u_{r_{I,j}}\right)\Delta z + \left(u_{z_{i+1,J}} - u_{z_{i,J}}\right) r_J \Delta r = 0 \tag{5.12}$$

The above equation will be used later to determine the pressure distribution equation in the flow domain.

5.1.3 Nanoparticle Continuity Equation

The steady-state axi-symmetric nanoparticle continuity equation is given in equation (4.21) as:

$$\frac{1}{r}\frac{\partial}{\partial r}(r u_r \varphi) + \frac{\partial}{\partial z}(u_z \varphi) = \left[\frac{1}{r}\frac{\partial}{\partial r}\left(r D_B \frac{\partial \varphi}{\partial r}\right) + \frac{\partial}{\partial z}\left(D_B \frac{\partial \varphi}{\partial z}\right)\right] + \left[\frac{1}{r}\frac{\partial}{\partial r}\left(r \frac{D_T}{T}\frac{\partial T}{\partial r}\right) + \frac{\partial}{\partial z}\left(\frac{D_T}{T}\frac{\partial T}{\partial z}\right)\right]$$

Integration of the nanoparticle continuity equation over the scalar control volume surrounding nodal point P (in Fig. 5.3) gives the following final form:

$$a_{p_1}\varphi_{I,J} = a_{n_1}\varphi_{I,J+1} + a_{s_1}\varphi_{I,J-1} + a_{e_1}\varphi_{I+1,J} + a_{w_1}\varphi_{I-1,J} + a_{n_2}T_{I,J+1} + a_{s_2}T_{I,J-1} + a_{e_2}T_{I+1,J} + a_{w_2}T_{I-1,J} - a_{p_2}T_{I,J} \tag{5.13}$$

where,

$$a_{p_1} = a_{n_1} + a_{s_1} + a_{e_1} + a_{w_1} + (F_n - F_s) + (F_e - F_w)$$

$$a_{p_2} = a_{n_2} + a_{s_2} + a_{e_2} + a_{w_2}$$

$$a_{n_1} = max\left[-F_n, \left(D_n - \frac{F_n}{2}\right), 0\right], \quad a_{s_1} = max\left[F_s, \left(D_s + \frac{F_s}{2}\right), 0\right]$$

$$a_{e_1} = max\left[-F_e, \left(D_e - \frac{F_e}{2}\right), 0\right], \quad a_{w_1} = max\left[F_w, \left(D_w + \frac{F_w}{2}\right), 0\right]$$

$$F_n = r_{j+1}u_{r_{I,j+1}}\Delta z, \quad F_s = r_j u_{r_{I,j}}\Delta z, \quad F_e = u_{z_{i+1,J}} r_J \Delta r, \quad F_w = u_{z_{i,J}} r_J \Delta r$$

$$D_n = \frac{D_{B_{I,J+1}} + D_{B_{I,J}}}{2}\frac{r_{j+1}\Delta z}{\Delta r}, \quad D_s = \frac{D_{B_{I,J}} + D_{B_{I,J-1}}}{2}\frac{r_j \Delta z}{\Delta r}$$

$$D_e = \frac{D_{B_{I+1,J}} + D_{B_{I,J}}}{2}\frac{r_J \Delta r}{\Delta z}, \quad D_w = \frac{D_{B_{I,J}} + D_{B_{I-1,J}}}{2}\frac{r_J \Delta r}{\Delta z}$$

$$a_{n_2} = \frac{\left(\frac{D_T}{T}\right)_{I,J+1} + \left(\frac{D_T}{T}\right)_{I,J}}{2}\frac{r_{j+1}\Delta z}{\Delta r}, \quad a_{s_2} = \frac{\left(\frac{D_T}{T}\right)_{I,J} + \left(\frac{D_T}{T}\right)_{I,J-1}}{2}\frac{r_j \Delta z}{\Delta r}$$

$$a_{e_2} = \frac{\left(\frac{D_T}{T}\right)_{I+1,J} + \left(\frac{D_T}{T}\right)_{I,J}}{2} \frac{r_J \Delta r}{\Delta z}, \qquad a_{w_2} = \frac{\left(\frac{D_T}{T}\right)_{I,J} + \left(\frac{D_T}{T}\right)_{I-1,J}}{2} \frac{r_J \Delta r}{\Delta z}$$

5.1.4 Nanofluid Energy Equation

For nanofluid, two additional terms are added to the right side of the energy equation of a pure fluid which truly account for the additional contribution associated with the nanoparticle motion relative to the base fluid. The equation is given in equation (4.22) as:

$$\rho C_p \left[\frac{1}{r}\frac{\partial}{\partial r}(r u_r T) + \frac{\partial}{\partial z}(u_z T)\right] = k\left[\frac{1}{r}\frac{\partial}{\partial r}\left(r\frac{\partial T}{\partial r}\right) + \frac{\partial^2 T}{\partial z^2}\right] + \rho_{np} c_{np}\left[D_B\left(\frac{\partial \varphi}{\partial r}\frac{\partial T}{\partial r} + \frac{\partial \varphi}{\partial z}\frac{\partial T}{\partial z}\right) + \frac{D_T}{T}\left(\frac{\partial T}{\partial r}\frac{\partial T}{\partial r} + \frac{\partial T}{\partial z}\frac{\partial T}{\partial z}\right)\right]$$

Integration of the above equation over the scalar control volume of Fig. 5.3 gives the following final form:

$$a_p T_{I,J} = a_n T_{I,J+1} + a_s T_{I,J-1} + a_e T_{I+1,J} + a_w T_{I-1,J} + S_1 + S_2 \tag{5.14}$$

where,

$$a_p = a_n + a_s + a_e + a_w + (F_n - F_s) + (F_e - F_w) - C_1 - C_2$$

$$a_n = max\left[-F_n, \left(D_n - \frac{F_n}{2}\right), 0\right], \qquad a_s = max\left[F_s, \left(D_s + \frac{F_s}{2}\right), 0\right]$$

$$a_e = max\left[-F_e, \left(D_e - \frac{F_e}{2}\right), 0\right], \qquad a_w = max\left[F_w, \left(D_w + \frac{F_w}{2}\right), 0\right]$$

$$F_n = r_{j+1} u_{r_{I,j+1}} \Delta z, \quad F_s = r_j u_{r_{I,j}} \Delta z, \quad F_e = r_J u_{z_{i+1,J}} \Delta r, \quad F_w = r_J u_{z_{i,J}} \Delta r$$

$$D_n = \frac{\alpha r_{j+1} \Delta z}{\Delta r}, \quad D_s = \frac{\alpha r_j \Delta z}{\Delta r}, \quad D_e = \frac{\alpha r_J \Delta r}{\Delta z}, \quad D_w = \frac{\alpha r_J \Delta r}{\Delta z}$$

$$S_1 = \frac{\rho_{np} c_{np}}{\rho c_p} \frac{0.26k}{k + k_{np}} \frac{\mu}{\rho} \frac{r_J \Delta z}{4\Delta r} \frac{\varphi_{I,J}}{T_{I,J}} \left(T_{I,J+1} - T_{I,J-1}\right)^2$$

$$S_2 = \frac{\rho_{np} c_{np}}{\rho c_p} \frac{0.26k}{k + k_{np}} \frac{\mu}{\rho} \frac{r_J \Delta r}{4\Delta z} \frac{\varphi_{I,J}}{T_{I,J}} \left(T_{I+1,J} - T_{I-1,J}\right)^2$$

$$C_1 = \frac{\rho_{np} c_{np}}{\rho c_p} \frac{k_B}{3\pi\mu d_{np}} \frac{r_J \Delta z}{4\Delta r} \left(\varphi_{I,J+1} - \varphi_{I,J-1}\right)\left(T_{I,J+1} - T_{I,J-1}\right)$$

$$C_2 = \frac{\rho_{np} c_{np}}{\rho c_p} \frac{k_B}{3\pi\mu d_{np}} \frac{r_J \Delta r}{4\Delta z} \left(\varphi_{I+1,J} - \varphi_{I-1,J}\right)\left(T_{I+1,J} - T_{I-1,J}\right)$$

5.1.5 Absorber Plate Conduction Equation (2D)

Absorber plate is a rectangular plate. For discretising the conduction equation, we need a Cartesian grid as shown in Fig. 5.4. The two-dimensional conduction equation for a solar absorber plate is given in equation (4.23) as:

$$k\left[\frac{\partial T^2}{\partial y^2} + \frac{\partial T^2}{\partial z^2}\right] + \frac{\mathrm{I_t}(\tau\alpha)}{t} - \frac{U_L(\mathrm{T} - \mathrm{T_\alpha})}{\mathrm{t}} = 0$$

Integrating the above equation over the control volume surrounding nodal point P in Fig. 5.4 gives the following final form:

$$a_p T_{I,J} = a_n T_{I,J+1} + a_s T_{I,J-1} + a_e T_{I+1,J} + a_w T_{I-1,J} + \frac{\mathrm{I_t}(\tau\alpha)}{kt}\Delta y \Delta z + \frac{U_L}{kt}\Delta y \Delta z T_a \qquad (5.15)$$

$$a_p = a_n + a_s + a_e + a_w + \frac{\mathrm{U_L}}{kt}\Delta y \Delta z$$

$$a_n = a_s = \frac{\Delta z}{\Delta y}, \quad a_e = a_w = \frac{\Delta y}{\Delta z}$$

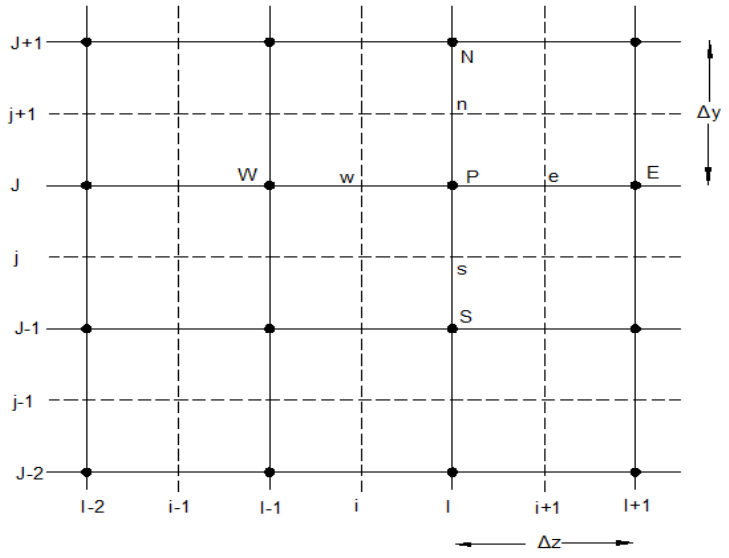

Fig. 5.4: Cartesian grid

5.1.6 Implementation of Boundary Conditions

All CFD problems are defined in terms of initial and boundary conditions. Since this study is under steady-state condition, only the boundary conditions are needed. In a staggered grid arrangement, additional nodes are set up surrounding the physical boundary, as shown in Fig. 5.5. The calculations are made only at internal nodes (I=2, J=2 and onwards). With this arrangement, the physical boundaries coincide with the scalar cell boundaries and the nodes just outside the actual boundaries are available to store the boundary conditions.

This grid arrangement enables the implementation of boundary conditions with very small modifications to the discretised equations for near boundary internal nodes. The most used boundary types in this study are:

- Inlet
- Outlet
- Wall
- Symmetry

Detailed study of the implementation of boundary conditions in this study can be found in [69].

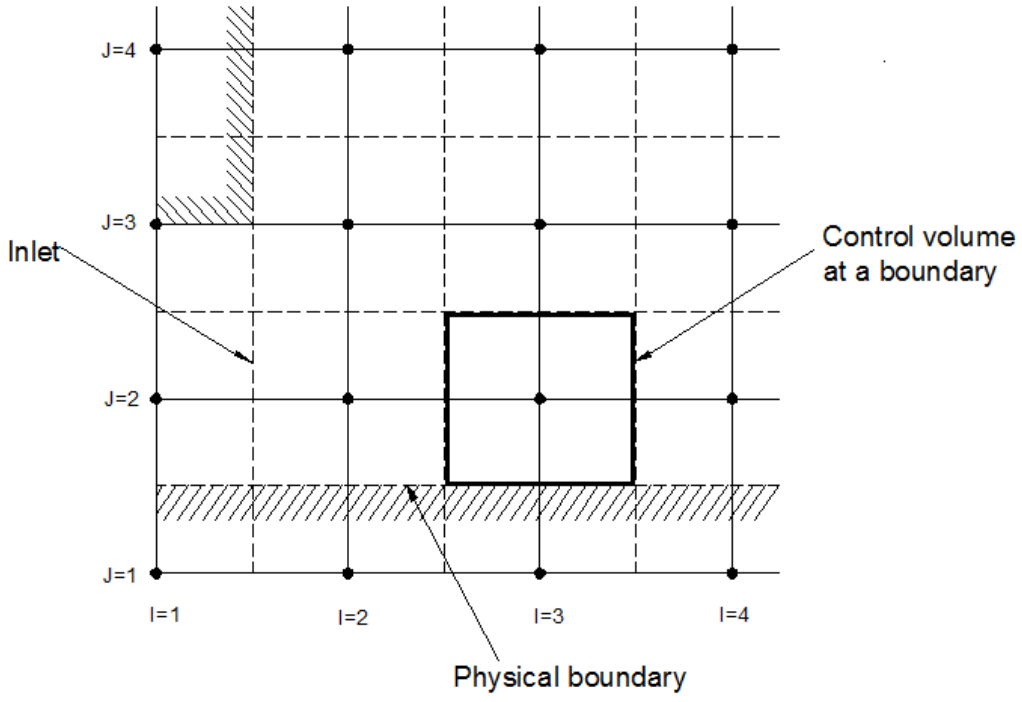

Fig. 5.5: Grid arrangement for boundary implementation

5.1.7 Solution of Discretised Equations

Among the various discretized governing equations, the solution of the flow equations are the most problematic because the pressure field is unknown. Once the pressure field is known, discretised momentum equation can be written for each u_r and u_z control volume and then solved to obtain the velocity fields. A correct pressure field will produce a velocity field which in turn will satisfy the continuity equation. Once the velocity field is known, all other discretised transport equations can be solved.

To solve for the pressure field, this study incorporates an algorithm called SIMPLER algorithm developed by Patankar [66]. SIMPLER stands for Semi-Implicit Method for Pressure Linked Equations-Revised. In this algorithm, the discretised continuity equation is used to derive a discretised pressure equation.

The discretised momentum equations (5.10) and (5.11) are re-arranged as:

$$u_{r_{I,j}} = \frac{\sum a_{nb} u_{r_{nb}}}{a_{p_{I,j}}} + \frac{\left(P_{I,J-1} - P_{I,J}\right) r_j \Delta z}{a_{p_{I,j}}} \tag{5.16}$$

$$u_{z_{i,J}} = \frac{\sum a_{nb} u_{z_{nb}}}{a_{p_{i,J}}} + \frac{\left(P_{I-1,J} - P_{I,J}\right) r_J \Delta r}{a_{p_{i,J}}} \tag{5.17}$$

In the SIMPLER algorithm, pseudo-velocities $\widehat{u_r}$ and $\widehat{u_z}$ are defined as follows:

$$\widehat{u_r} = \frac{\sum a_{nb} u_{r_{nb}}}{a_{p_{I,j}}}$$

$$\widehat{u_z} = \frac{\sum a_{nb} u_{z_{nb}}}{a_{p_{i,J}}}$$

So the equations (5.16) and (5.17) can be written as:

$$u_{r_{I,j}} = \widehat{u_r}_{I,j} + \frac{r_j \Delta z}{a_{p_{I,j}}} \left(P_{I,J-1} - P_{I,J}\right) \tag{5.18}$$

$$u_{z_{i,J}} = \widehat{u_z}_{i,J} + \frac{r_J \Delta r}{a_{p_{i,J}}} \left(P_{I-1,J} - P_{I,J}\right) \tag{5.19}$$

Substituting for $u_{r_{I,j}}$ and $u_{z_{i,J}}$ from these equations into the discretised continuity equation of (5.12), using similar forms for $u_{r_{I,j+1}}$ and $u_{z_{i+1,J}}$ results in:

$$\left[r_{j+1}\left(\widehat{u_r}_{I,j+1}+\frac{r_{j+1}\Delta z}{a_{p_{I,j+1}}}\left(P_{I,J}-P_{I,J+1}\right)\right)-r_j\left(\widehat{u_r}_{I,j}+\frac{r_j\Delta z}{a_{p_{I,j}}}\left(P_{I,J-1}-P_{I,J}\right)\right)\right]\Delta z$$
$$+\left[\widehat{u_z}_{i+1,J}+\frac{r_J\Delta r}{a_{p_{i+1,J}}}\left(P_{I,J}-P_{I+1,J}\right)-\widehat{u_z}_{i,J}+\frac{r_J\Delta r}{a_{p_{i,J}}}\left(P_{I-1,J}-P_{I,J}\right)\right]r_J\Delta r=0 \tag{5.20}$$

Equation (5.20) is re-arranged to the following discretised pressure equation:

$$a_{I,J}P_{I,J}=a_{I,J+1}P_{I,J+1}+a_{I,J-1}P_{I,J-1}+a_{I+1,J}P_{I+1,J}+a_{I-1}P_{I-1,J}+b_{I,J} \tag{5.21}$$

where,

$$a_{I,J}=a_{I,J+1}+a_{I,J-1}+a_{I+1,J}+a_{I-1,J}$$

$$a_{I,J+1}=\frac{\left(r_{j+1}\Delta z\right)^2}{a_{p_{I,j+1}}},\quad a_{I,J-1}=\frac{\left(r_j\Delta z\right)^2}{a_{p_{I,j}}},\quad a_{I+1,J}=\frac{\left(r_J\Delta r\right)^2}{a_{p_{i+1,J}}},\quad a_{I-1,J}=\frac{\left(r_J\Delta r\right)^2}{a_{p_{i,J}}}$$

$$b_{I,J}=\left(r_j\widehat{u_r}_{I,j}-r_{j+1}\widehat{u_r}_{I,j+1}\right)\Delta z+\left(\widehat{u_z}_{i,J}-\widehat{u_z}_{i+1,J}\right)r_J\Delta r$$

The SIMPLER algorithm uses another pressure correction equation which is as follows:

$$a_{I,J}P'_{I,J}=a_{I,J+1}P'_{I,J+1}+a_{I,J-1}P'_{I,J-1}+a_{I+1,J}P'_{I+1,J}+a_{I-1}P'_{I-1,J}+b'_{I,J} \tag{5.22}$$

All of the coefficients are same as of discretised pressure equation (5.21) except $b'_{I,J}$

$$b'_{I,J}=\left(r_ju^*_{r_{I,j}}-r_{j+1}u^*_{r_{I,j+1}}\right)\Delta z+\left(u^*_{z_{i,J}}-u^*_{z_{i+1,J}}\right)r_J\Delta r$$

The SIMPLER algorithm is given in Fig. 5.6.

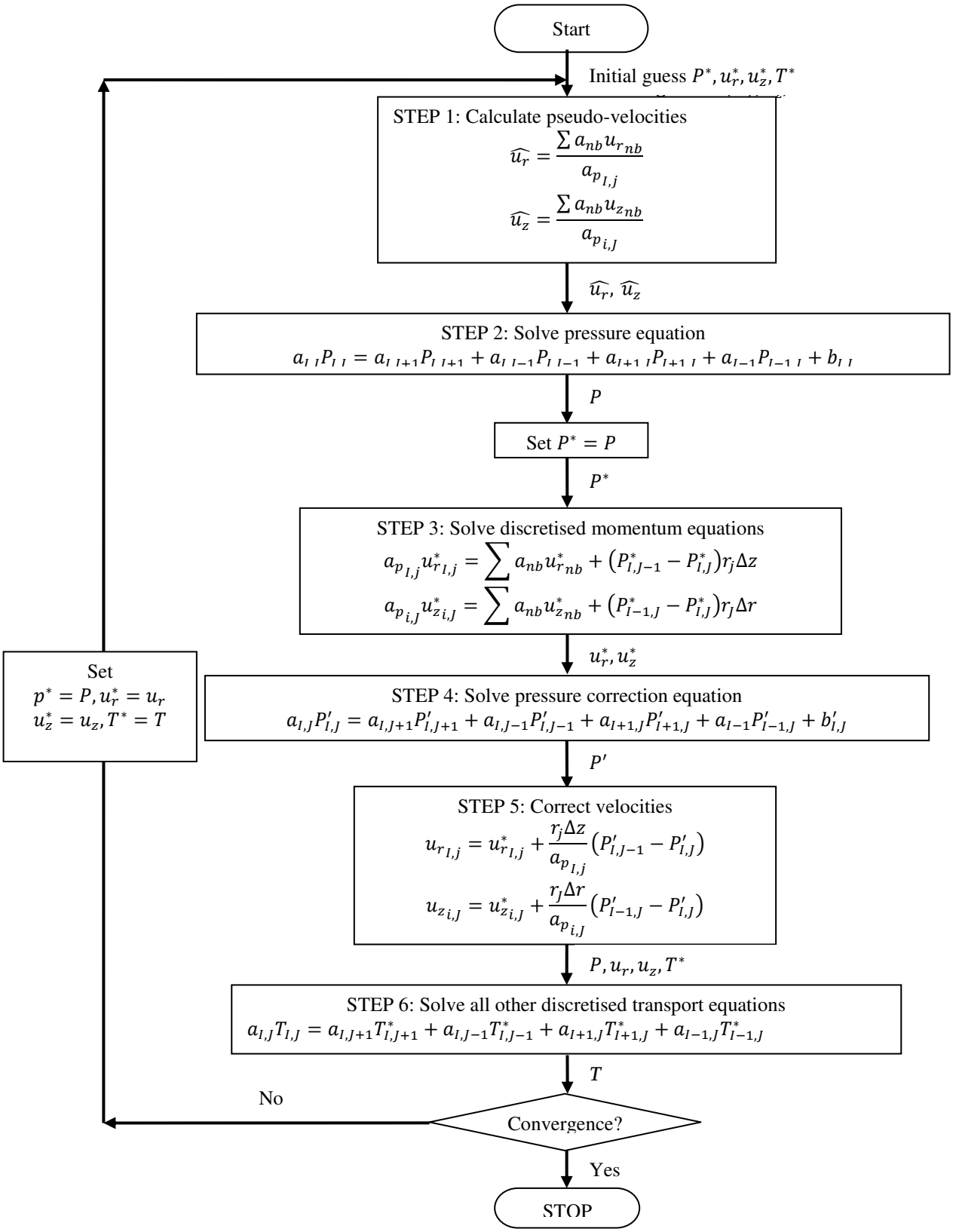

Fig. 5.6: Flowchart of SIMPLER algorithm

5.2 Finite Element Method

The finite element method (FEM) is a numerical method that can be used for the accurate solution of complex engineering problems. In FEM, the solution region is considered of many small, interconnected sub regions called finite elements. These elements are considered to be interconnected at specified joints called nodes or nodal points. The nodes usually lie on the element boundaries where adjacent elements are considered to be connected. The variation of the field variables (e.g., displacement, stress, temperature, pressure, or velocity) inside a finite element is approximated by a simple function. These approximating functions (also called interpolation models) are defined in terms of the values of the field variables at the nodes. When field equations (like equilibrium equations) for the whole continuum are written, the only unknowns will be the nodal values of the field variables. By solving the field equations, which are generally in the form of matrix equations, the nodal values of the field variables are known. Once these are known, the approximating functions define the field variable throughout the assemblage of elements. The solution of a general continuum problem by the finite element method always follows an orderly step-by-step process as stated in Fig. 5.7.

In this study, the finite element method is applied for the three-dimensional analysis of solar plate with internally finned riser tubes. Galerkin's weighted residual method is applied to generate the finite element equations.

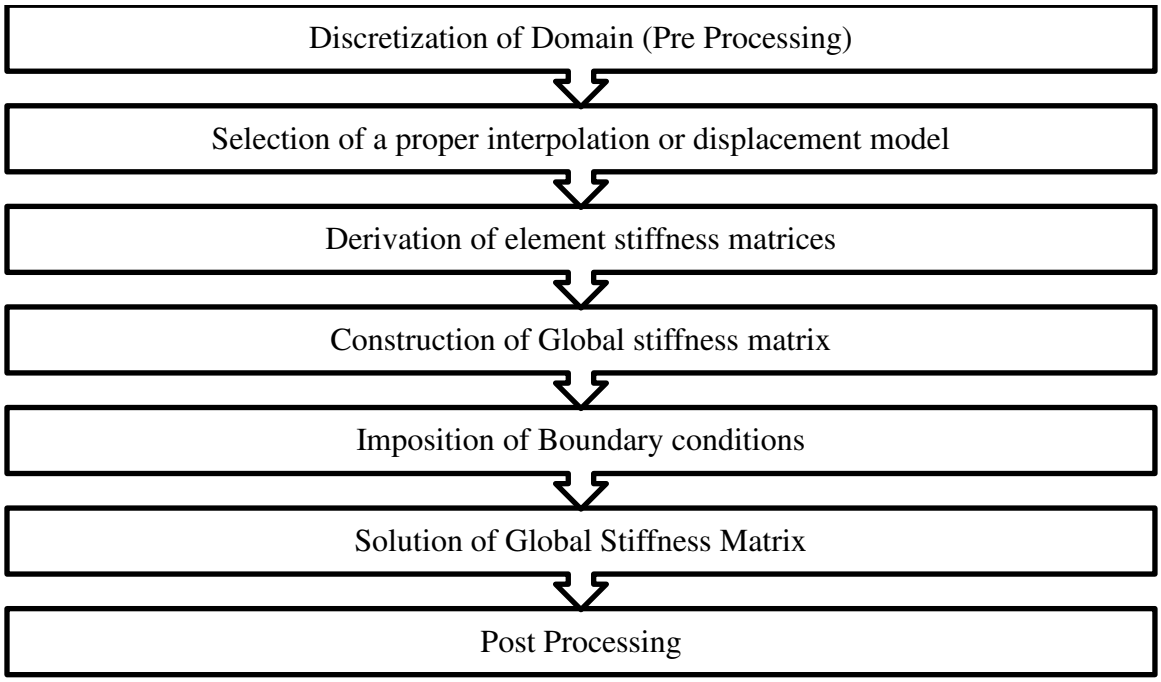

Fig. 5.7: Flowchart of solving technique by Finite Element Method

5.3 Post Analyses

After obtaining the velocity and temperature field, additional calculations are done to obtain the desired parameters. The various parameters used and discussed in this study are convective heat transfer coefficient, Nusselt number, Reynolds number, shear stress, solar plate efficiency etc. The expressions of different parameters are as following:

Reynolds number: $\mathrm{Re}= \frac{\rho V_{av} D}{\mu}$

Wall shear stress: $\tau_s = -\mu \frac{du_z}{dr}$

Local convective coefficient: $h_z = \frac{q}{T_{s_z} - T_{b_z}}$

Average convective coefficient: $h_{av} = \frac{1}{L}\int_0^L h_z dz$

Local Nusselt number: $Nu_z = \frac{h_z D}{k}$

Average Nusselt number: $Nu_{av} = \frac{h_{av} D}{k}$

Average velocity: $V_{av} = \frac{2}{R^2}\int_0^R Vrdr$

Bulk temperature: $T_{b_z} = \frac{2}{V_{av} R^2}\int_0^R T_z Vrdr$

The integrations are performed using the trapezoidal and Simpson's 1/3rd rule of integration.

FPC Efficiency: Under steady-state conditions, the useful heat delivered by a solar plate collector is equal to the energy absorbed by the plate minus the heat lost from the surface to the surroundings. The useful energy from a collector can be obtained from the following formula:

$$q_u = A_c\left[I_t(\tau\alpha) - U_L\left(T_p - T_\alpha\right)\right] = mc_p(T_{in} - T_{out}) \tag{5.23}$$

where, m is the mass flow rate, A_c is the surface area of the absorber plate, I_t is the solar irradiation and T_{in} and T_{out} are the average temperature of the inlet and outlet section of the riser tube.

The total energy fallen on the collector plate is $A_c I_t$, so the efficiency of the flat plate collector can be calculated with the following equation:

$$\eta = \frac{q_u}{A_c I_t} \tag{5.24}$$

5.4 Geometry and Grid

Study of nanofluid involves nanofluid flow in a straight circular pipe. With the assumption of axi-symmetric fluid and heat flow, the 3D domain is converted into a 2D rectangular domain. To study the nanofluid flow and temperature distribution, this domain is divided into many small volumes or cells upon which the governing equations are reposted. This is called meshing. Rectangular grids are used for meshing. The meshed study domain is shown in Fig. 5.8.

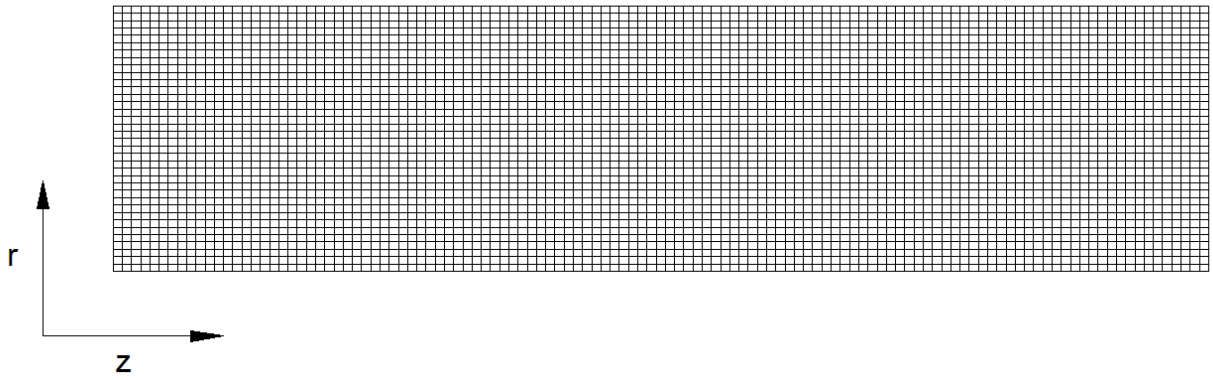

Fig. 5.8: Meshed domain for nanofluid study

For the solar plate study with nanofluid, the flow domain is exactly like in Fig. 5.8 and the absorber plate domain is assumed two dimensional. So, the absorber plate domain is also like the domain in Fig. 5.8 but with y and z direction instead of r and z direction.

Solar plate study with internally finned riser tube requires 3D investigation. The physical domain considered for solar plate study is shown in Fig. 4.3 and as the physical body is symmetric about the middle plane, only half of the body is considered during numerical computation. Tetrahedral elements are used for meshing of the domain. The solar plate domain and meshing are shown in Fig. 5.9.

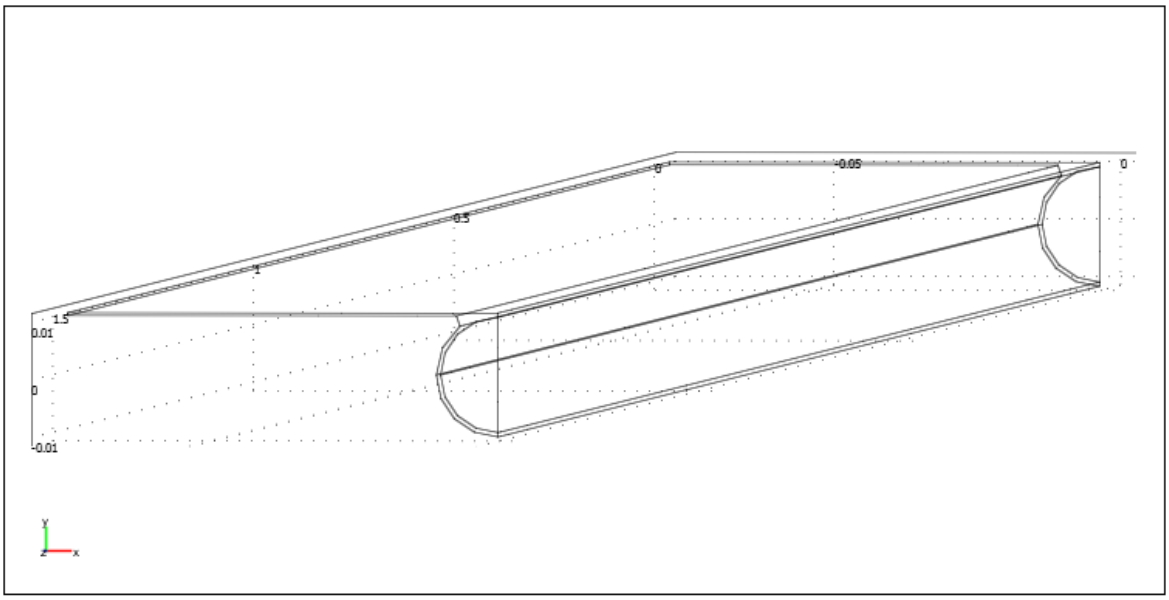

(a)

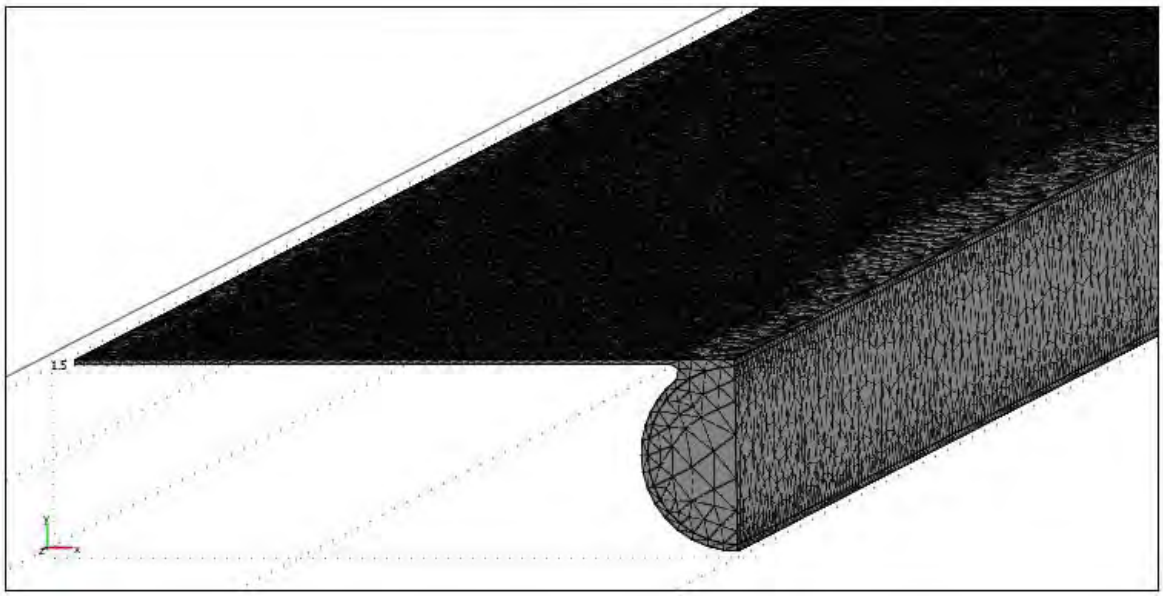

(b)

Fig. 5.9: Solar plate domain (a) without, (b) with mesh

5.5 Grid Independence Test

For the nanofluid study, rectangular grids are used to discretise the study domain. The domain is discretised with different numbers of mesh elements and temperature at the middle of the domain is monitored. It is found that after 9000 mesh elements, the variation of temperature is almost

zero as shown in Fig. 5.10. So, 9000 mesh elements are considered satisfactory for the nanofluid study.

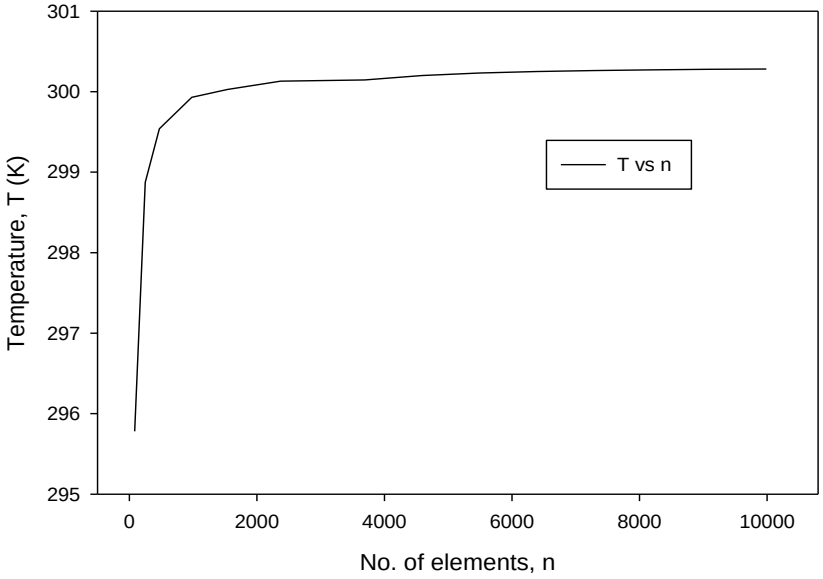

Fig. 5.10: Grid independence test for FVM

For the 3D investigation, tetrahedral mesh elements are also checked to ensure accurate results. Here also the temperature is plotted against the number of mesh elements in Fig. 5.11 to see the variation. It shows that the variation is very small after number of mesh elements of 800000. However, more elements than 1636147 couldn't be checked as the computer was out of memory. So, 1630000 mesh elements are considered satisfactory here.

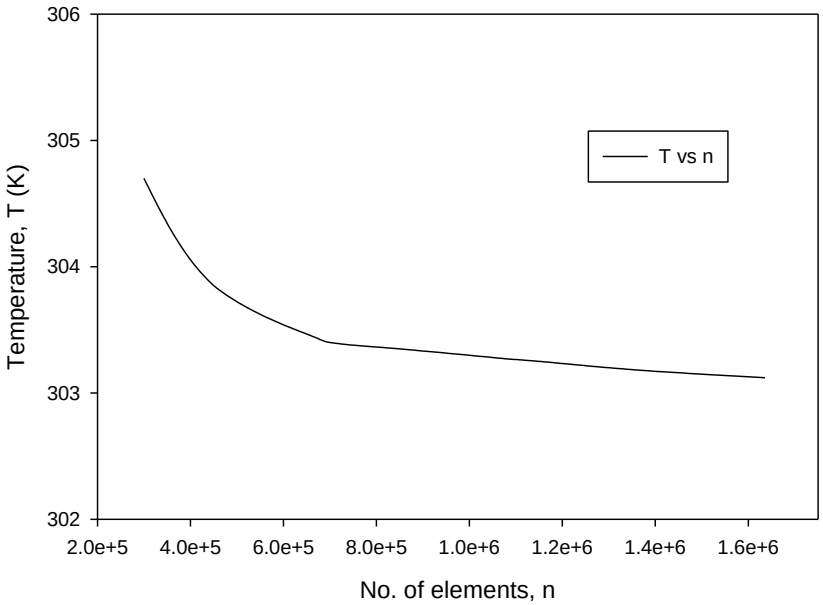

Fig. 5.11: Grid independence test for FEM

5.6 Code validation

The nanofluid study is done by writing a code using FVM method. To validate the code, Nusselt numbers calculated from pure water flow is compared with the Nusselt number correlation for constant wall heat flux given by Shah and London [70]. The two results are plotted in Fig. 5.12. The two plots are almost identical with present results slightly higher in the developing flow region and it gradually decreases to slightly lower values in the fully developed region than the Shah and London [70] results. The above trend of variation of the present results can be attributed to the use of temperature independent properties. The Shah and London correlation is given by equation (5.23).

$$Nu_{z_*} = \begin{cases} 3.302 z_*^{-1/3} - 1.00 & z_* \le 0.00005 \\ 1.302 z_*^{-1/3} - 0.50 & 0.00005 < z_* \le 0.0015 \\ 4.364 + 8.68(10^3 z_*)^{-0.506} e^{-41 z_*} & z_* > 0.0015 \end{cases} \quad (5.23)$$

where,

$$z_* = \frac{z/D}{Re.Pr}$$

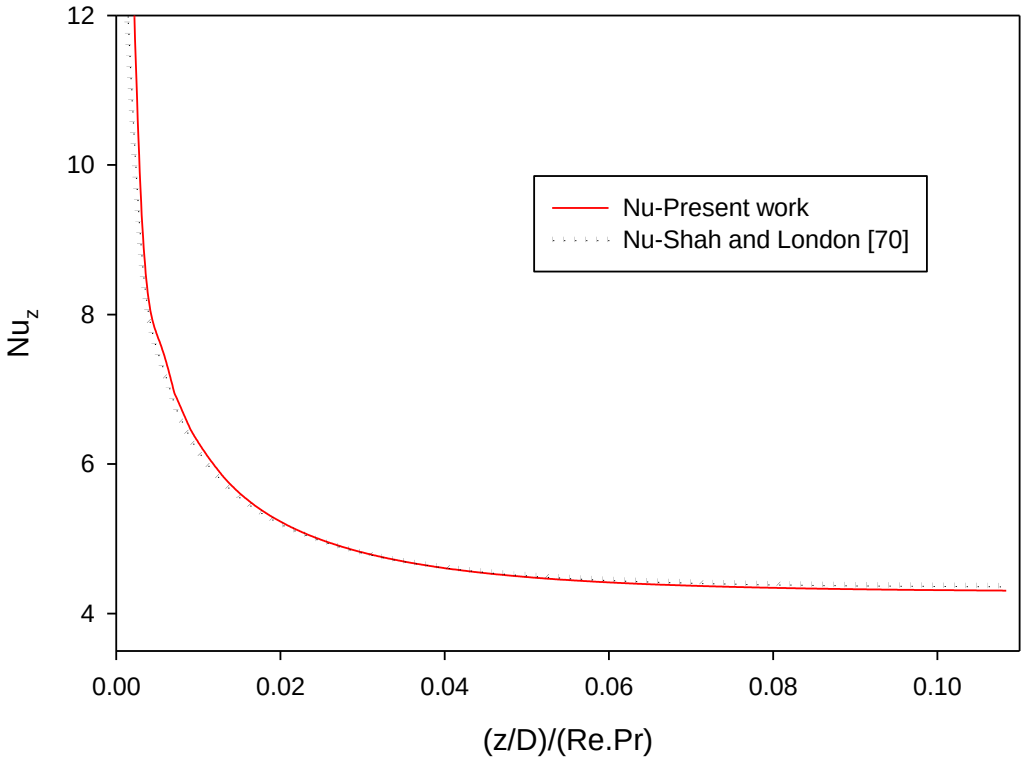

Fig. 5.12: Code validation of nanofluid study

The codes for solar plate study are validated by comparing it with the results given by Kalougirou [21]. The FVM and FEM both methods are applied to calculate the efficiency of a flat plate collector with water as the working fluid. The results of both studies are plotted with the results of Kalogirou [21] in Fig. 5.13. For the comparison, velocity of the water is taken as 0.075 m/s, overall heat loss coefficient, U_L as 7 and the atmospheric temperature as 288 K are taken. The plots show that the results of FVM and FEM are in good agreement with the results of Kalogirou [21]. The FVM method gives slightly higher results than FEM. This could be because of the additional assumptions that are made during the FVM study of solar plate. But the difference is very small that the results by the two methods also can be used to compare results of different geometries and working fluids. The numeric values of the efficiency from different studies are given in table 5.1.

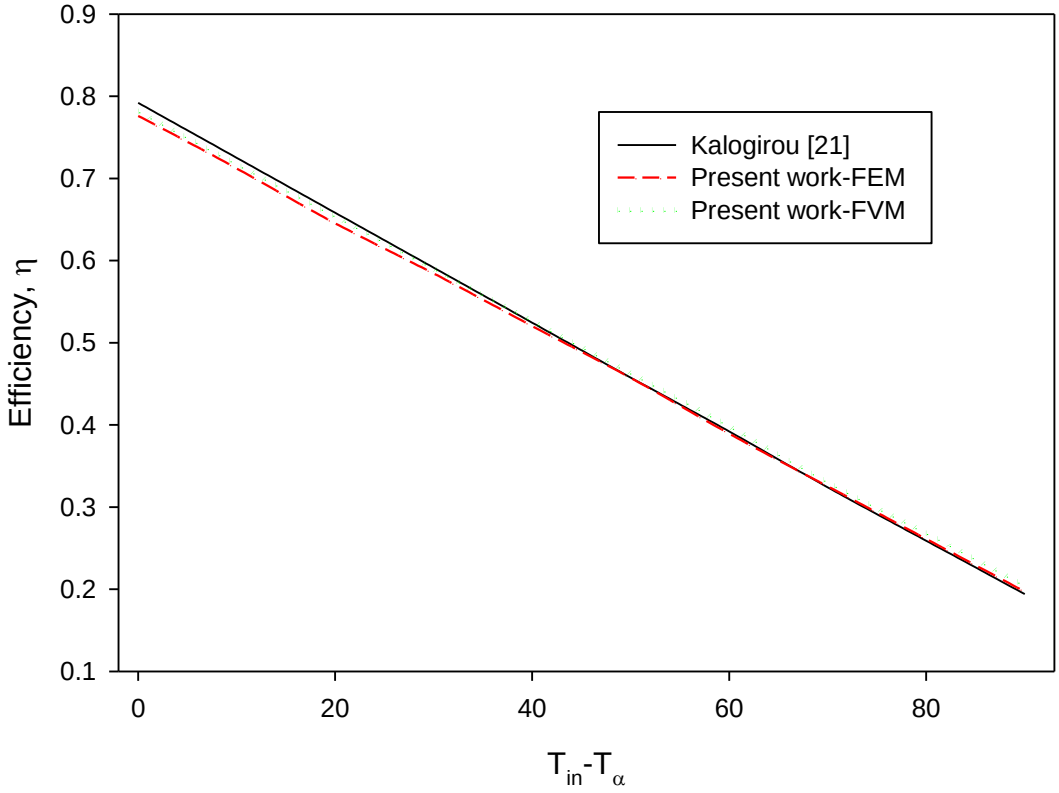

Fig. 5.13: Code validation for solar plate study

Table 5.1: Numeric values of the flat plate collector efficiency

Temperature difference, (T_{in}-T_{α}) (°C)	Efficiency		
	Kalogirou [21]	Present work-FVM	Present work-FEM
0	0.792	0.782	0.776
10	0.725	0.717	0.712
20	0.658	0.654	0.647
30	0.591	0.590	0.584
40	0.524	0.526	0.520
50	0.458	0.463	0.457
60	0.392	0.398	0.389
70	0.324	0.330	0.325
80	0.259	0.268	0.261
90	0.194	0.204	0.197

Chapter 6

Results and Discussion

This thesis work performs numerical simulation of nanofluid model and flat plate collector model. The various models are solved with a self developed code with FVM discretization. Only for the flat plate collector with internally finned tube, the study performs 3D investigation with FEM discretization. Temperature independent properties are used for the simulations. The various results found from the numerical simulations are discussed in the following sections.

6.1 Nanofluid Study Results

Simulation for nanofluid study is carried out with $\varphi = 0\%, 2\%$ and 4% at Reynolds numbers of 200, 400 and 600. A constant heat flux of 2500 W/m^2 is considered during the study. Change of different parameters like convective heat transfer coefficient, Nusselt number, shear stress etc. are investigated for nanoparticle immersion to the base fluid.

Fig. 6.1(a) shows the profiles of axial velocity along pipe radius at different length sections for pure water at Reynolds number of 200. The plot shows that for z/L=0.2 and 0.3, the two graphs almost coincide i.e. the flow is fully developed at z/L=0.2. Fig. 6.1(b) shows the axial velocity profiles for various nanoparticle concentration at z/L=0.3 for the mixture model. The velocity profiles are fully developed and are nearly identical with very small increase near the wall. The velocity of the mixture model slightly increases near the wall because of the reduced viscosity near the wall. The viscosity reduces near the wall because of the reduced nanoparticle concentration near the wall.

Dimensionless temperature is plotted along pipe radius in Fig. 6.2(a) at various locations along the axial direction at Re=200. Thermal entrance length is larger length than the hydrodynamic entrance length. The plots for z/L=0.4, 0.7, and 1.0 are almost identical, meaning a thermally fully developed flow. Fig. 6.2(b) shows the dimensionless temperature at outlet for various volume concentrations. The plots are almost identical. With the increase of volume

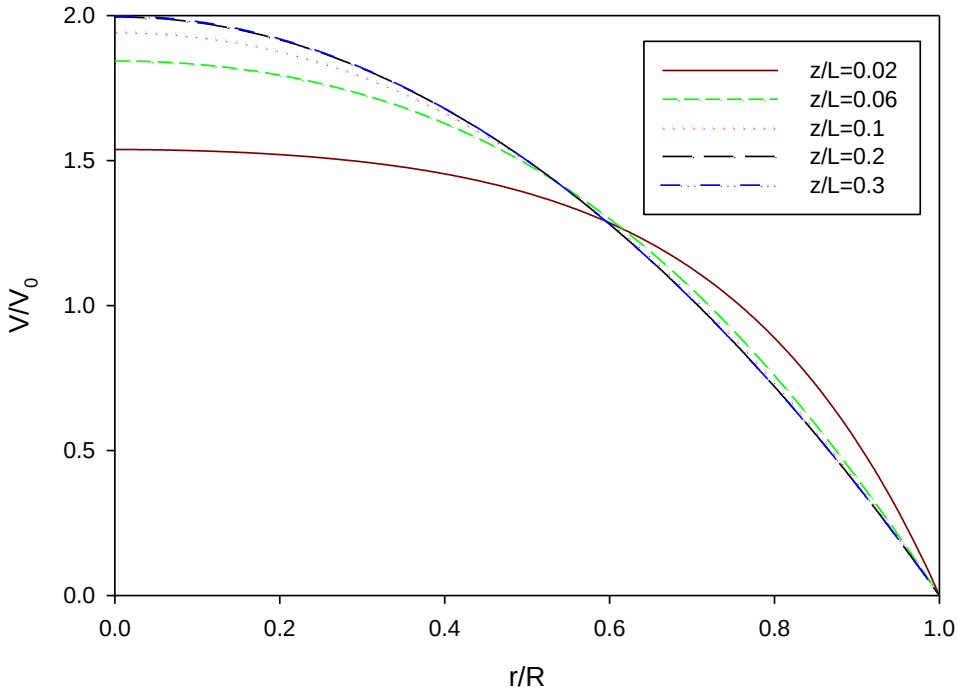

(a)

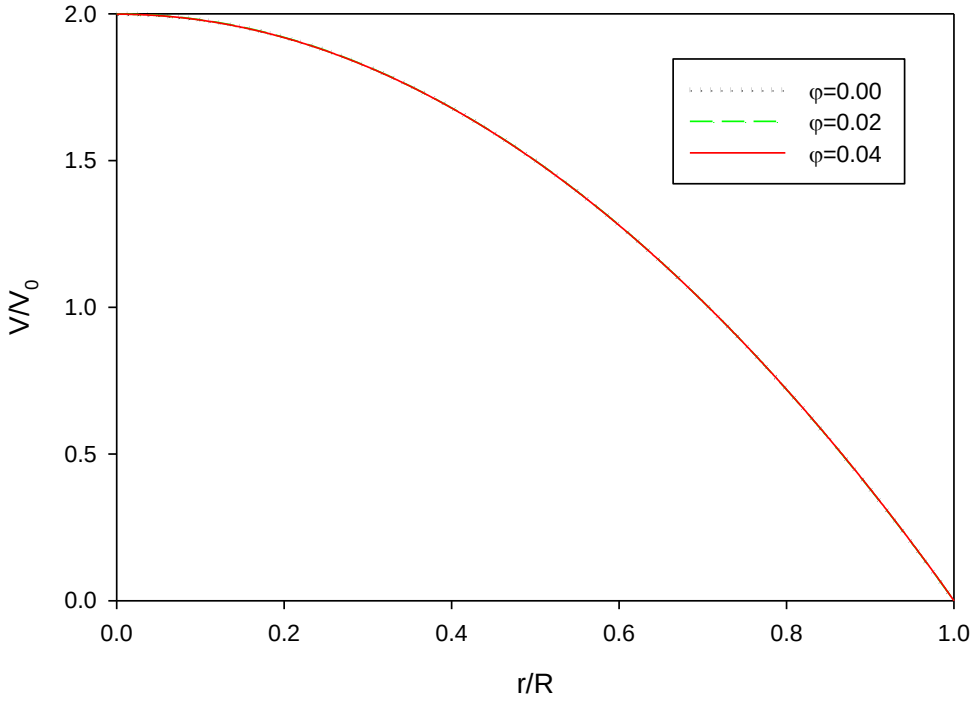

(b)

Fig. 6.1: Axial velocity profiles (a) at various locations for pure water, (b) at z/L=0.3 for various nanoparticle volume concentration.

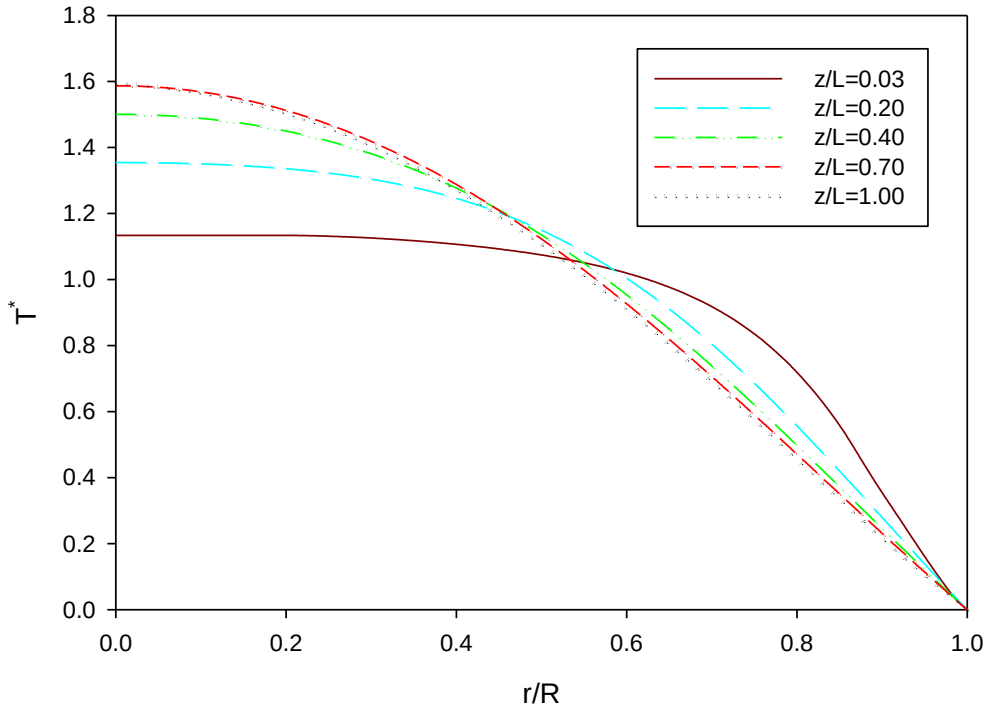

(a)

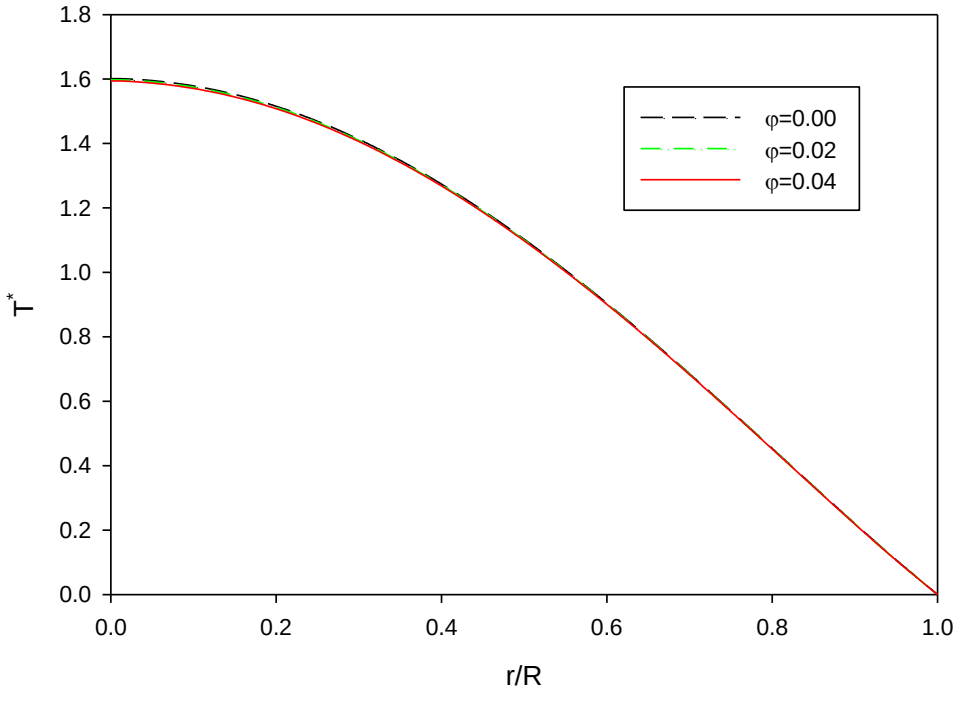

(b)

Fig. 6.2: Dimensionless temperature (a) at various locations for pure water, (b) at z/L=1.0 for various volume concentration.

concentration, Prandtl number increases only slightly. As a result, not much variation is seen in the plots of dimensionless temperature.

The local convective heat transfer coefficient is plotted in Fig. 6.3 for various nanoparticle concentrations at Re=200. The S-P and M-P stands for single-phase and mixture-phase respectively. The convective coefficient is very high at the entrance region and then drastically drops to an almost constant value at the fully developed region. The plots show an increasing convective heat transfer coefficient with increasing particle concentration. The single-phase and the mixture-phase models provide almost same results for most of the pipe length. Towards the end of the pipe, the difference between the single-phase and mixture-phase model increases whereas mixture-phase model provides lower values. At the exit section, the increment is 15% for single-phase model and 13% for mixture-phase model for nanoparticle volume fraction of 2%. For volume fraction of 4%, the increment is 31% for single-phase and 26% for mixture-phase model. The mixture model shows lower increment in heat transfer coefficients than the single-phase model. This is because the nanoparticle volume fraction reduces near the wall and as a result thermal conductivity gets reduced near the wall. Because of the reduced particle concentration, velocity increases slightly near the wall but not enough to compensate for the reduced conductivity. Also, the two additional terms in the right side of mixture-phase energy equation is very small to make noticeable difference in the convective coefficient. Fig. 6.4 and Fig. 6.5 show the plots of local convective heat transfer coefficient for Reynolds numbers of 400 and 600. It is seen that the difference between the single-phase and mixture-phase increases in the entrance region and the difference decreases in the fully developed region. Finally, the average convective heat transfer coefficient for various nanoparticle concentration and Reynolds number is plotted in Fig. 6.6. The figure shows that the convective coefficient increases with Reynolds number and nanoparticle volume fraction. The difference in the convective coefficient of single-phase and mixture-phase increases with the nanoparticle volume fraction. The convective coefficient increases by around 34% for 4% volume fraction of nanofluid found by single-phase model of study.

The local Nusselt numbers are plotted in Fig. 6.7, Fig. 6.8 and Fig. 6.9 for Reynolds numbers of 200, 400 and 600 respectively. All these graphs have the same trend as that of the convective heat transfer coefficient. The Nusselt numbers of different nanofluids depend on the nanofluid model and the nanoparticle concentration. Fig. 6.7 shows that, for mixture model study, the Nusselt number is higher in the entrance region and it falls below the Nusselt number of base fluid in the developed region. The single-phase model gives slightly higher Nusselt number than the base fluid in all sections of the pipe. As the Reynolds number increases, the Nusselt number becomes lower in the entrance region and higher in the developed region than the base fluid.

The average Nusselt number is plotted in Fig. 6.10 for various nanoparticle volume fractions at different Reynolds numbers. The variation of average Nusselt number is very small with the

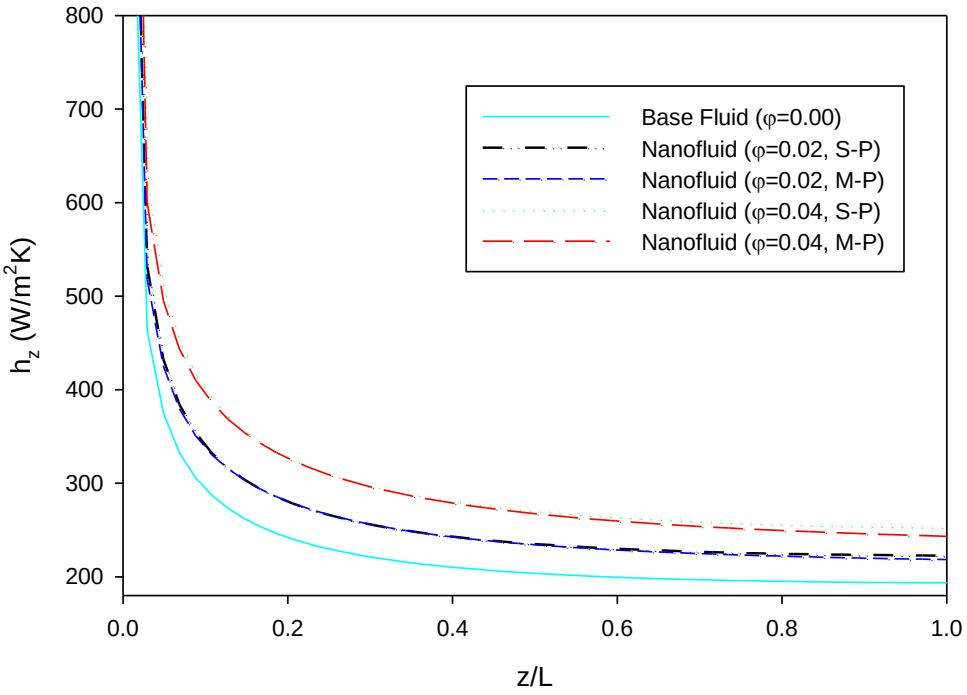

Fig. 6.3: Local convective heat transfer coefficient for various volume fractions at Re=200

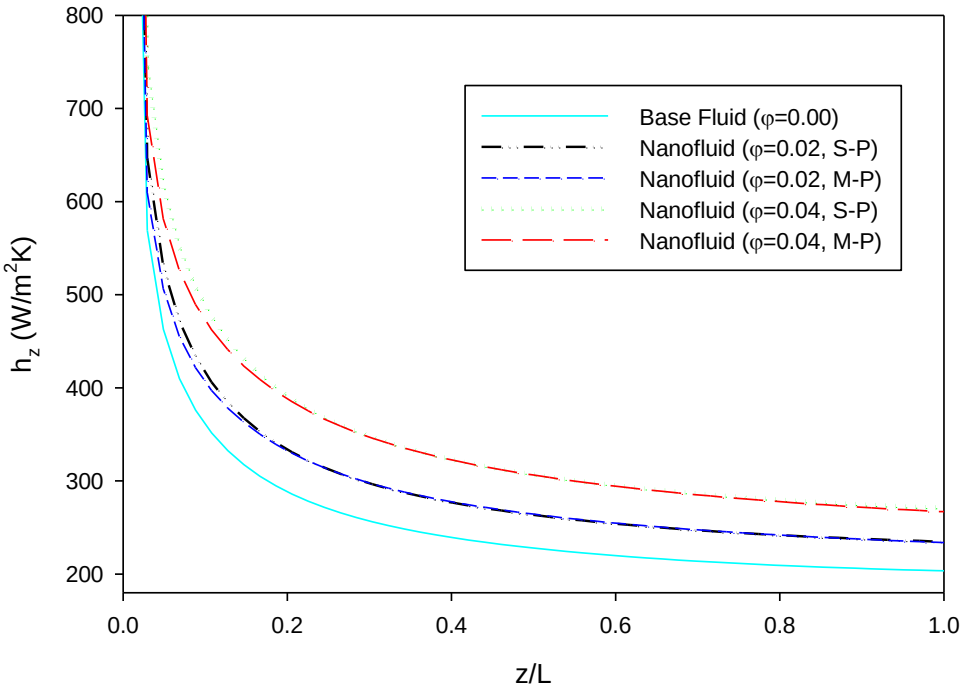

Fig. 6.4: Local convective heat transfer coefficient for various volume fractions at Re=400

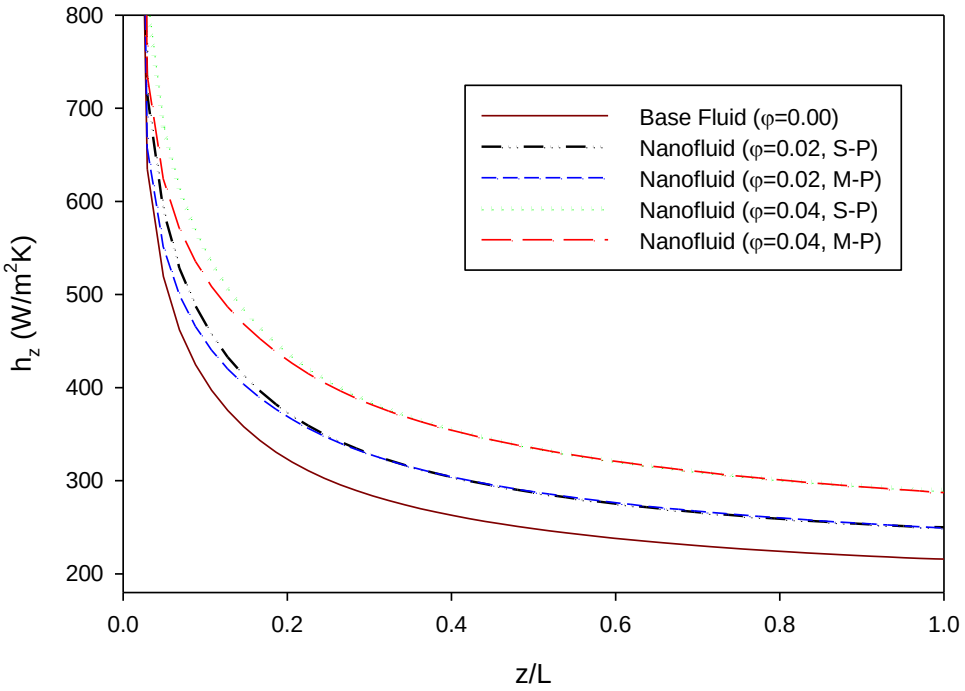

Fig. 6.5: Local convective heat transfer coefficient for various volume fractions at Re=600

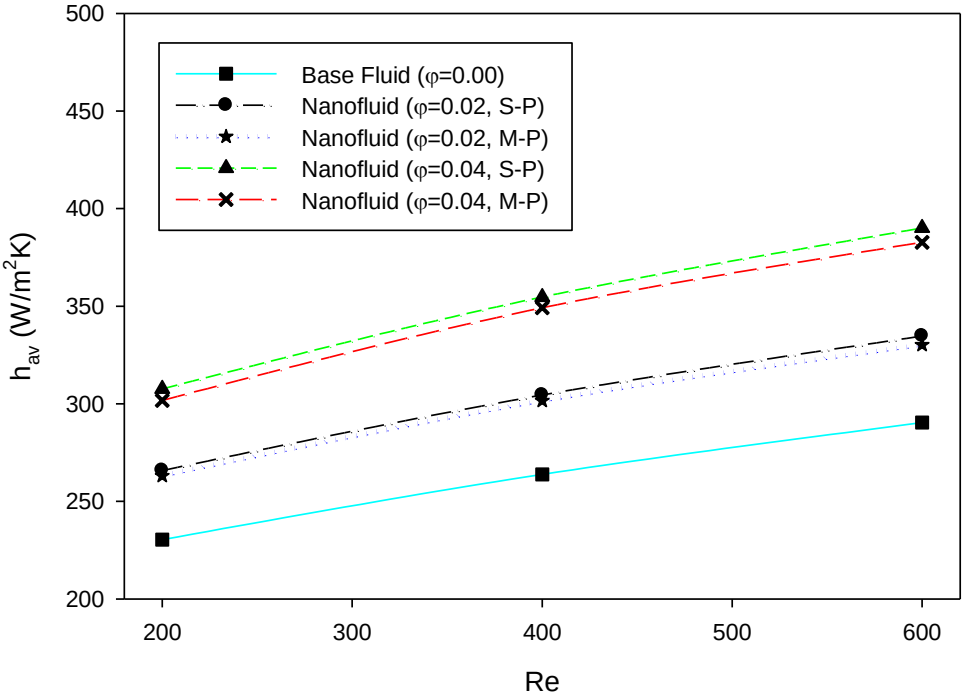

Fig. 6.6: Average convective heat transfer coefficient at different nanoparticle volume fractions

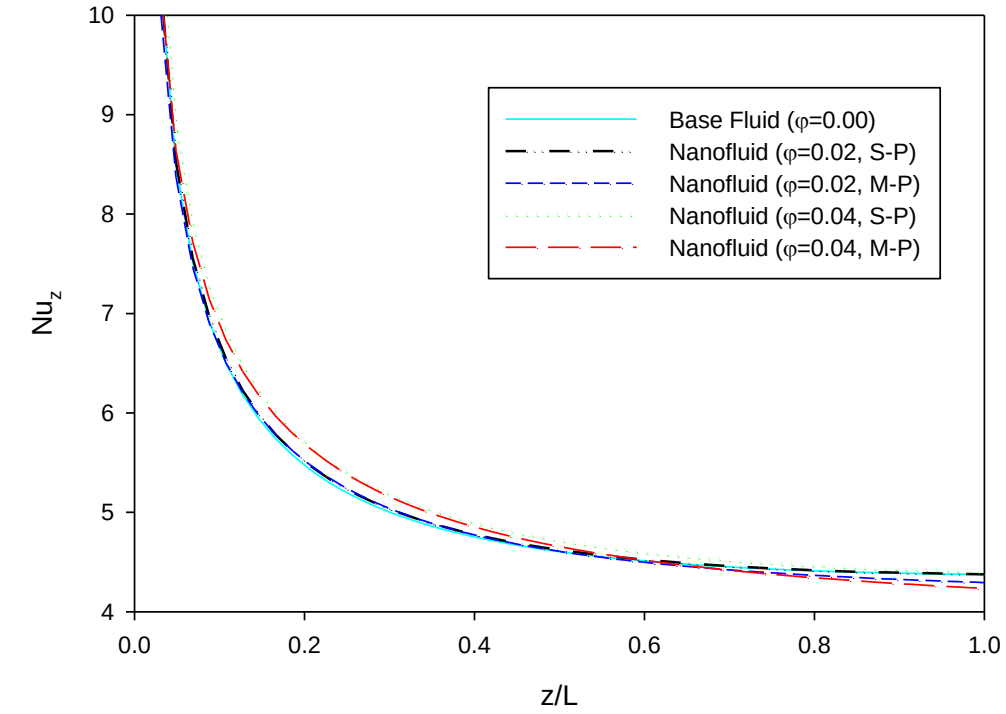

Fig. 6.7: Local Nusselt number for various volume fractions at Re=200

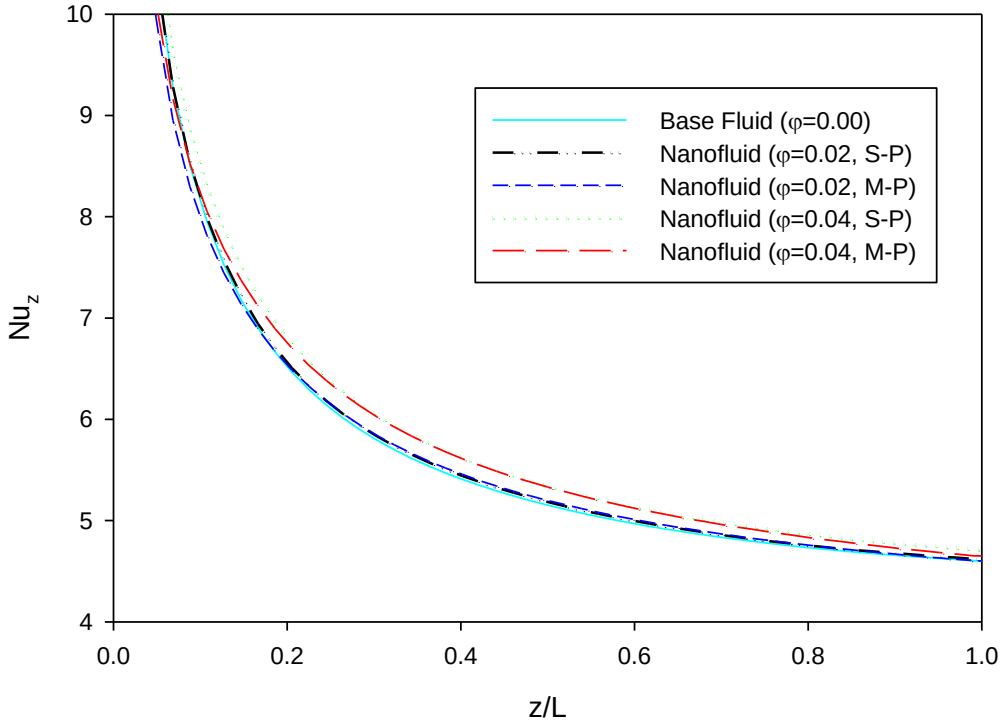

Fig. 6.8: Local Nusselt number for various volume fractions at Re=400

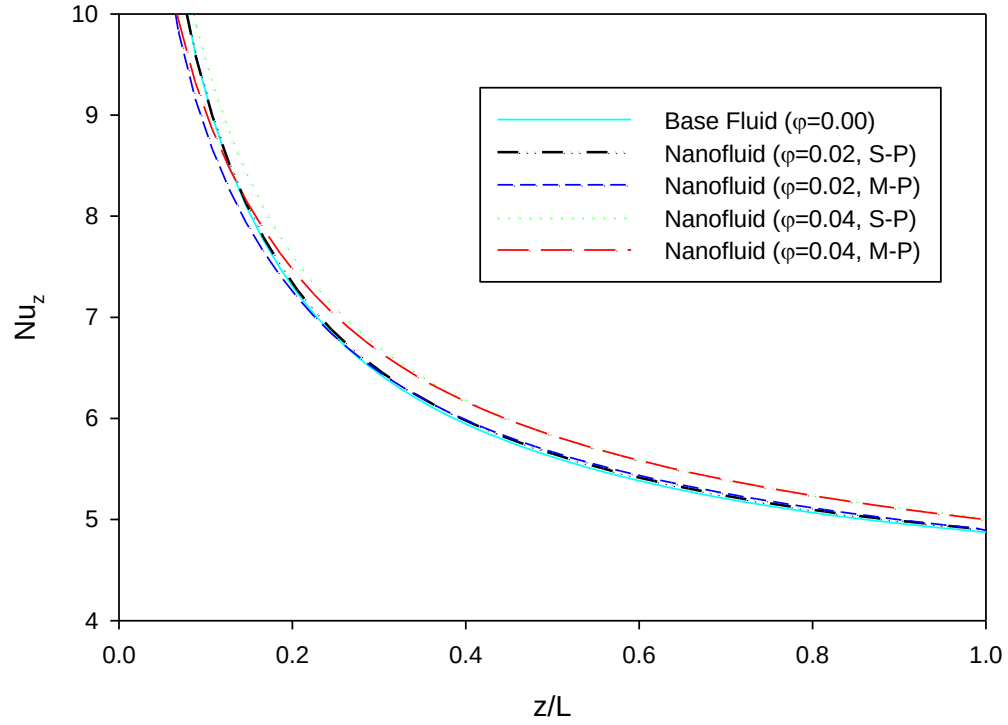

Fig. 6.9: Local Nusselt number for various volume fractions at Re=600

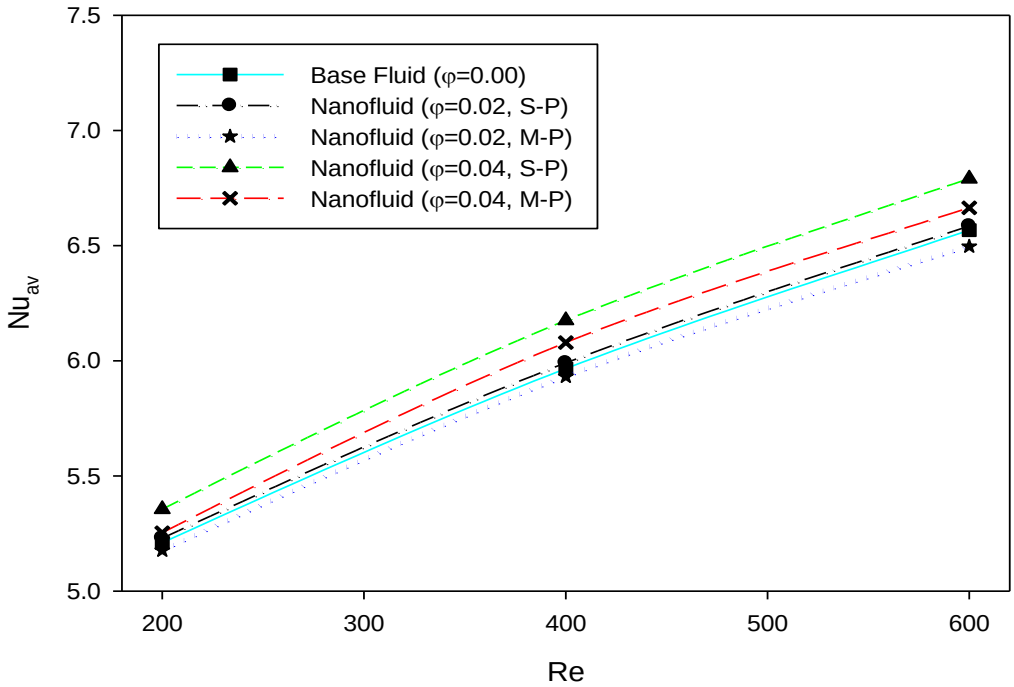

Fig. 6.10: Average Nusselt number for various volume fractions at different Reynolds number

nanoparticle volume percentages. For 2% volume fraction of nanoparticle, the mixture-phase model gives slightly lower average Nusselt number while the single-phase model gives slightly higher average Nusselt number than the base fluid. For 4% volume fraction, both the single-phase and mixture-phase model gives higher average Nusselt number than the base fluid.

The local shear stress is plotted for different volume concentration at Reynolds number of 200, 400 and 600 in Fig. 6.11, Fig. 6.12 and Fig. 6.13 respectively. The plots show that the stress drastically drops to an almost constant value near the inlet section. The shear stress is almost constant at later sections of the pipe. The shear stress increases with nanoparticle volume fraction and the relative increment with respect to base fluid is higher for 4% volume fraction than 2% volume fraction of nanoparticles. The mixture-phase model gives lower values of shear stress than the single-phase model as the viscosity near the wall reduces in the mixture-phase model. The average shear stress is plotted in Fig 6.14 for various volume fractions at different Reynolds numbers. The average shear stress increases with Reynolds number at an almost constant rate with the Reynolds number. The average shear stress increases by 40% and 140% than the base fluid for 2 and 4% volume fraction of nanoparticles for single-phase study. For mixture-phase study, the increment is 35% and 125% for 2 and 4% volume fraction of nanoparticles respectively. The variation of the average wall shear stress can be better assessed from the plots of axial velocity along the radius in Fig. 6.15 and Fig. 6.16. Fig. 6.15 shows the plots of axial velocity for different Reynolds number for pure water. It is obvious form the figure that the velocity gradient at wall increases proportionately with the Reynolds number and so the increase of wall shear stress in also proportional to the Reynolds number. Axial velocity for different nanoparticle volume fraction is plotted in Fig. 6.16 at a Reynolds number of 400. The figure shows that the velocity gradient near the wall increases with the nanoparticle volume fraction and relative increase is higher for higher volume fractions. Also the effective viscosity of the nanofluid increases exponentially with the nanoparticle volume fraction. So, the relative increment of wall shear stress increases with the increase in nanoparticle volume fraction as found in Fig. 6.14.

The various average values of convective heat transfer coefficient, Nusselt number, wall shear stress etc. are given in table 6.1 for different volume fractions at different Reynolds numbers.

The radial distribution of the nanoparticle volume fractions at inlet, middle and outlet section of the pipe are plotted in Fig. 6.17. The nanoparticle volume fraction reduces near the wall as the length of the tube increases and the reduction is higher at the outlet section. The figure also shows that the volume fraction slightly increases near the axis of the pipe. Fig. 6.18 shows the distribution of nanoparticle volume fraction for different Reynolds number at the outlet section. It shows that the reduction is highest for Re=200 and it gets reduced as the Reynolds number increases to 600. So, with higher Reynolds number, the nanoparticle distribution becomes more uniform. Both the figures are plotted for a volume fraction of 4%.

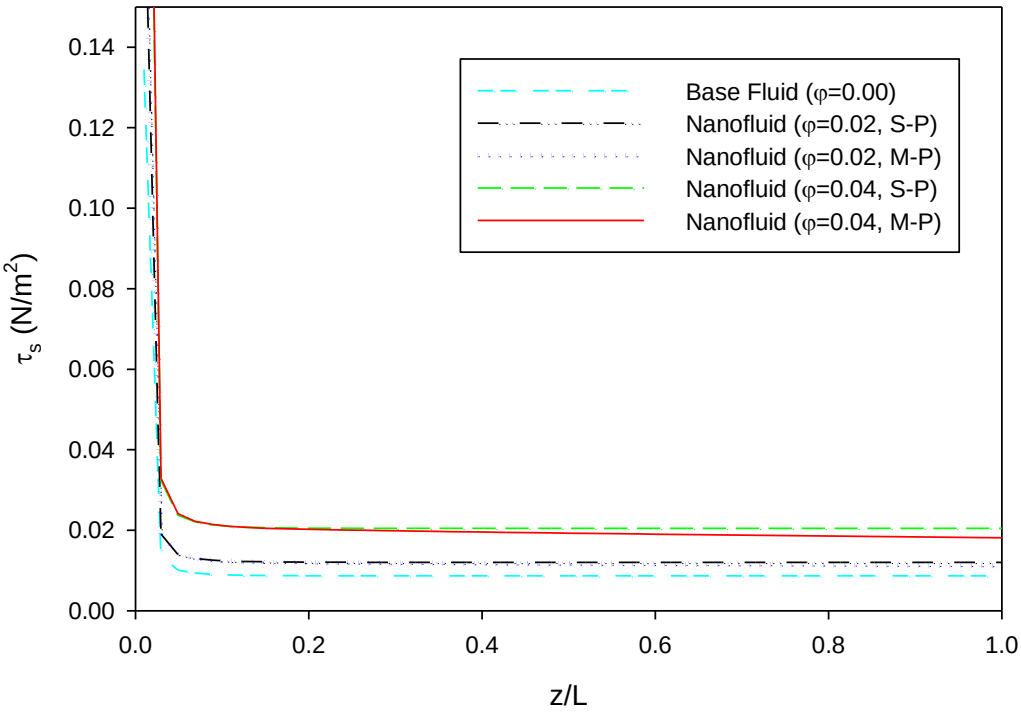

Fig. 6.11: Local shear stress for various volume fractions at Re=200.

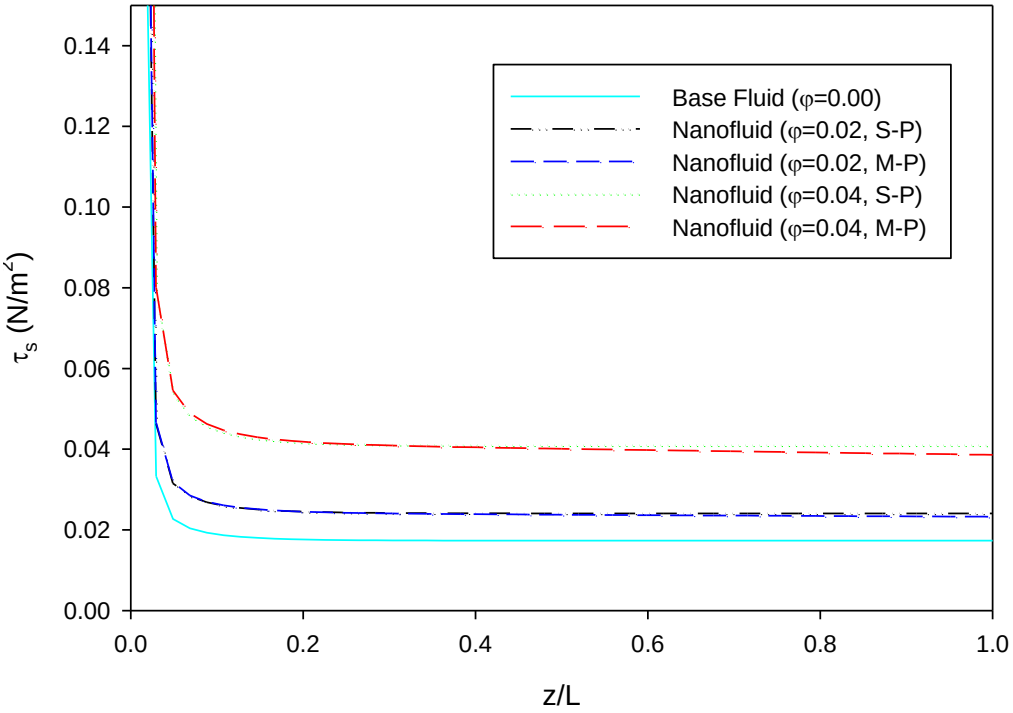

Fig. 6.12: Local shear stress for various volume fractions at Re=400.

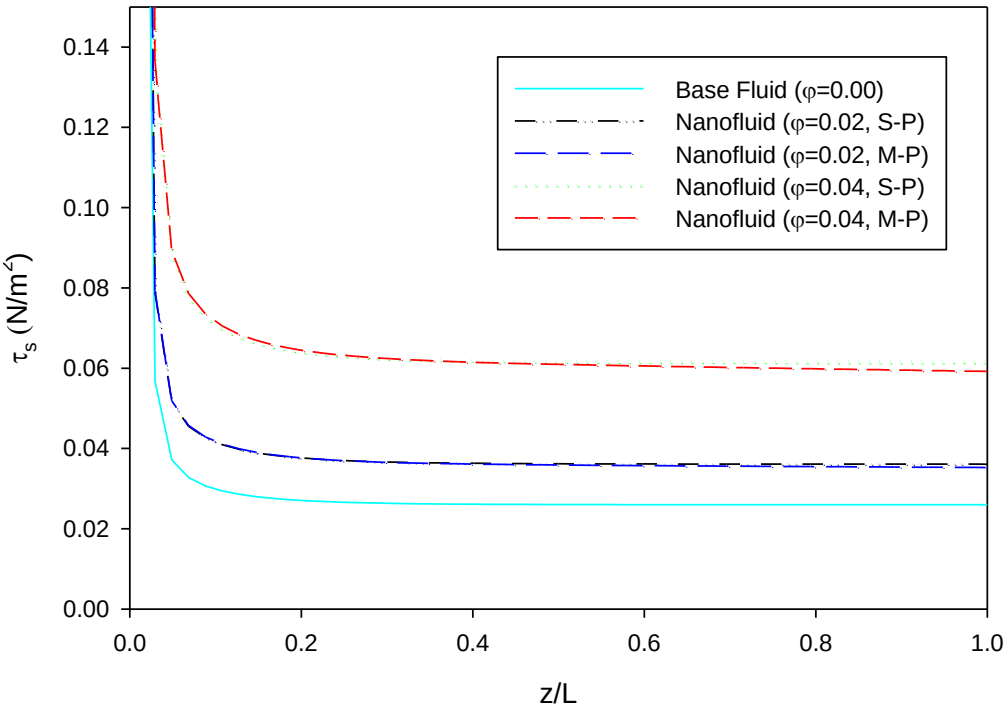

Fig. 6.13: Local shear stress for various volume fractions at Re=600.

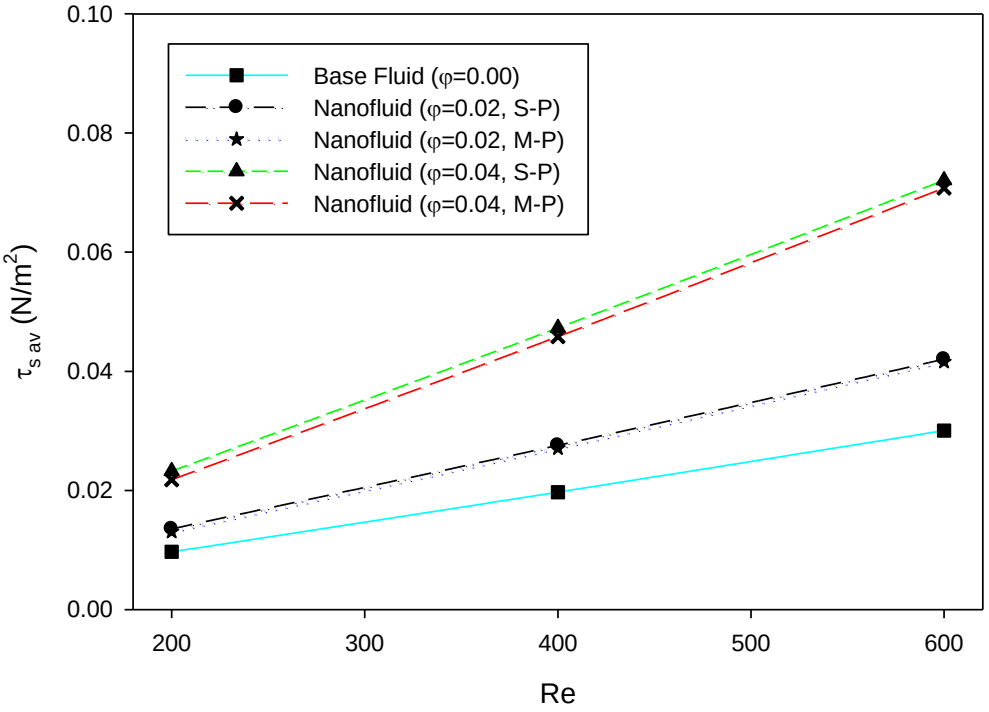

Fig. 6.14: Average shear stress for various volume fractions at different Reynolds number

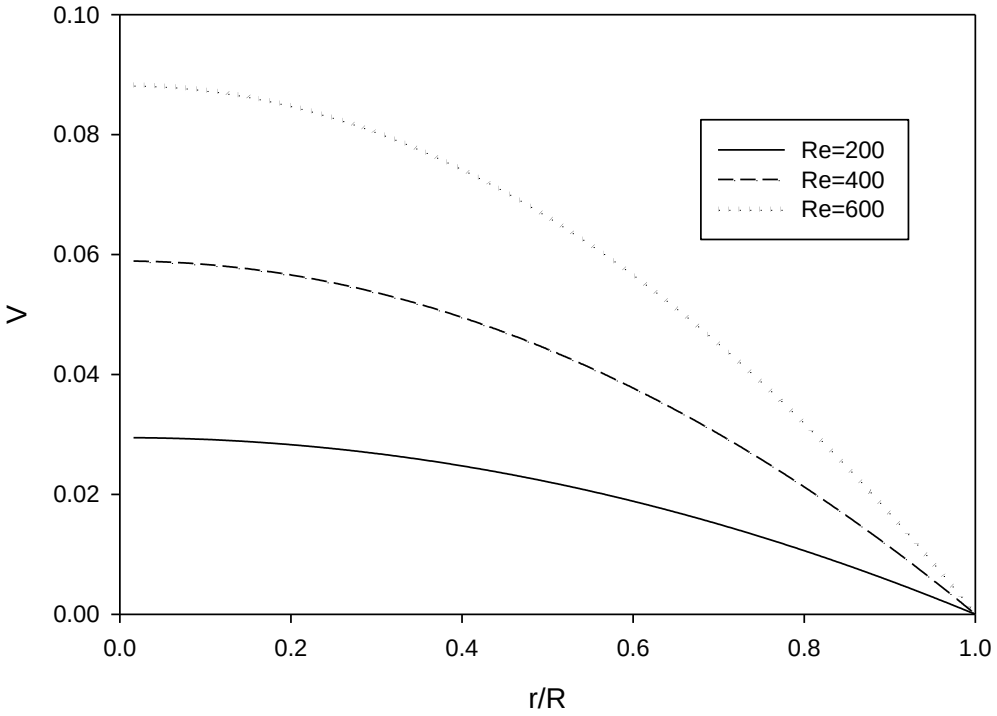

Fig. 6.15: Velocity comparison for different Reynolds number for pure water

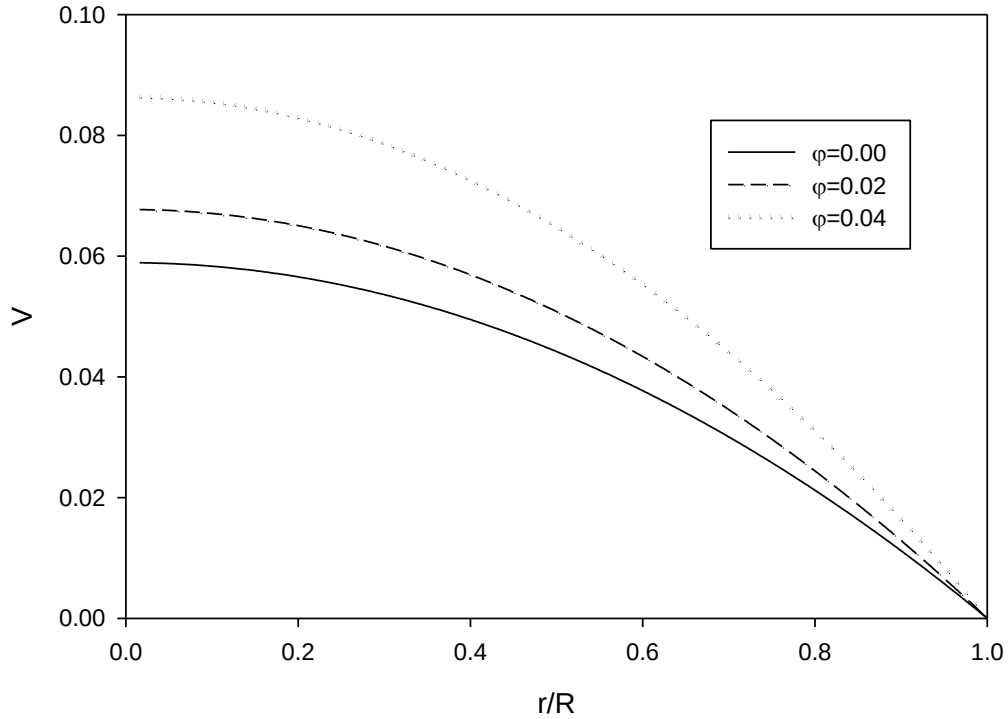

Fig. 6.16: Velocity comparison for different volume fractions at Re=400

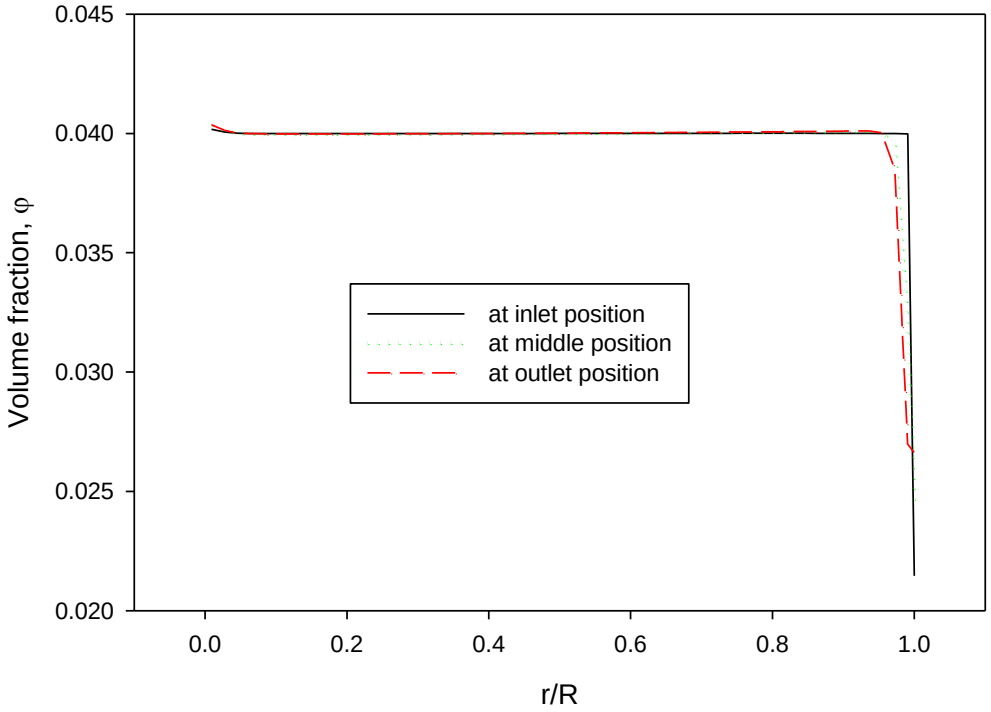

Fig. 6.17: Nanoparticle volume fraction at different positions for Re=400

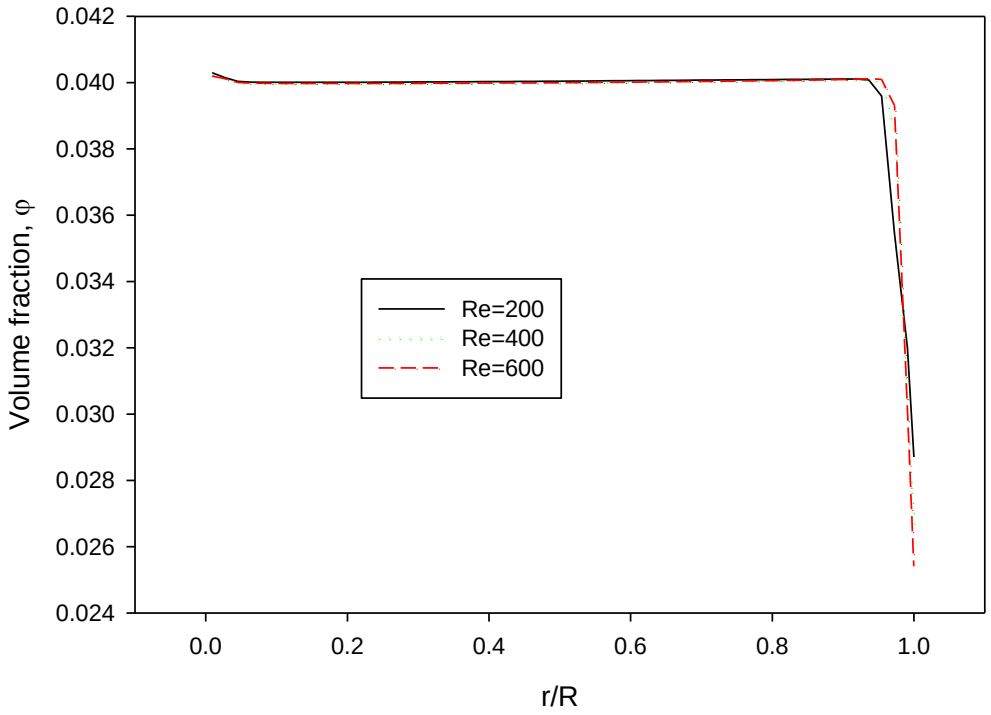

Fig. 6.18: Nanoparticle volume fraction at various Reynolds number

This study also investigates the particle diameter sensitivity of the mixture model studied here. The average convective heat transfer coefficient is plotted in Fig 6.19 for different nanoparticle diameters. The convection coefficient is essentially indifferent for different nanoparticle size with a very small reduction with the increase of particle size for this model. This is in turn proves that, the additional term on the energy equation for Brownian diffusion which depends on the particle size, have very negligible effect on the heat transfer for the Reynolds number range studied here.

Table 6.1: Various average values of convective coefficient, Nusselt number and shear stress

Reynolds number	Nanoparticle volume fraction		Convective coefficient, h_{av} (W/m^2K)	Nusselt number, Nu_{av}	Shear stress, $\tau_{s\,av}*10^3$ (N/m^2)
Re=200	φ=0.00		230.39	5.210	9.689
	φ=0.02	Single-phase	265.82	5.230	13.54
		Mixture-phase	262.03	5.176	13.07
	φ=0.04	Single-phase	307.61	5.356	23.23
		Mixture-phase	300.52	5.253	21.79
Re=400	φ=0.00		263.82	5.966	19.71
	φ=0.02	Single-phase	304.48	5.990	27.55
		Mixture-phase	300.28	5.931	27.08
	φ=0.04	Single-phase	354.67	6.175	47.26
		Mixture-phase	347.76	6.079	45.81
Re=600	φ=0.00		290.39	6.567	30.06
	φ=0.02	Single-phase	334.71	6.585	42.01
		Mixture-phase	328.86	6.496	41.57
	φ=0.04	Single-phase	390.03	6.791	72.06
		Mixture-phase	381.21	6.664	70.75

In Fig. 6.20, current study results are compared with an experimental result given by Heris et al. [38]. In the figure, convective coefficient ratio of nanofluid and base fluid are plotted against Peclet number. The nanofluid volume fraction is taken as 2.5%. The experimental convective coefficient ratio initially decreases and then increases with the Peclet number. The convective coefficient ratio found from single-phase study remains almost constant with Peclet number with very slight reduction with the increase of Peclet number. The convective coefficient ratio from the mixture-phase model slightly increases with the Peclet number. While the results from the single-phase and mixture-phase models are very close, these values are lower than the results reported by Heris et al. [38]. As the numerical study model of nanofluids is still in its development, many researchers have considered this range of deviation acceptable for the nanofluid study and implemented these results in calculation of the thermal performance of various heat exchanging devices. Based on the available nanofluid numerical models, the current results can be considered quite satisfactory for numerical study of nanofluids. The numeric values of the convective coefficient ratios are listed in Table 6.2.

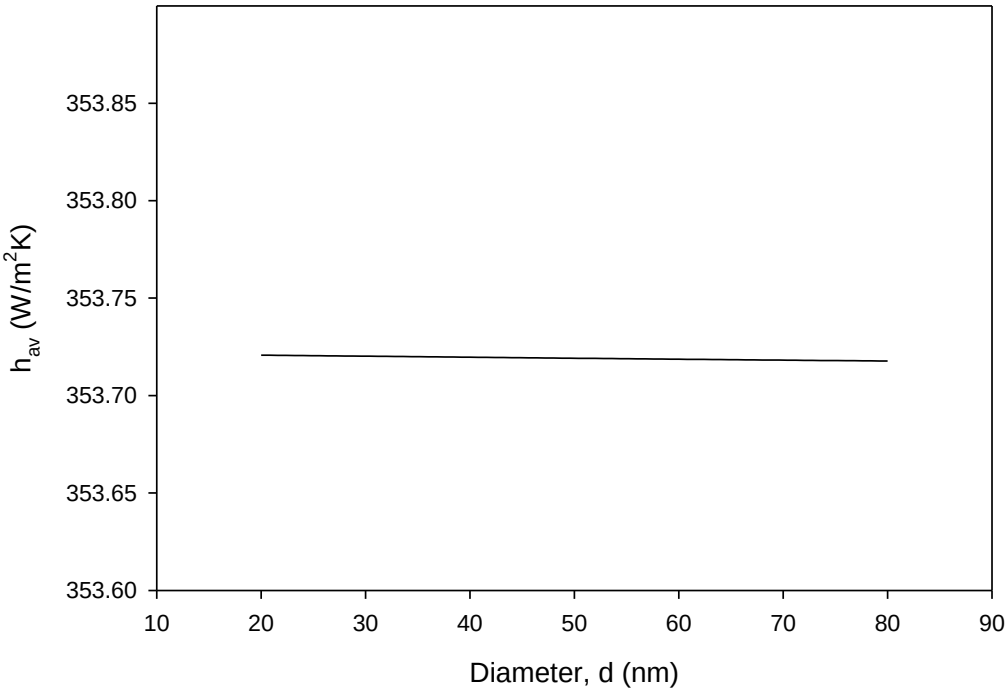

Fig. 6.19: Average convective heat transfer coefficient for different nanoparticle size

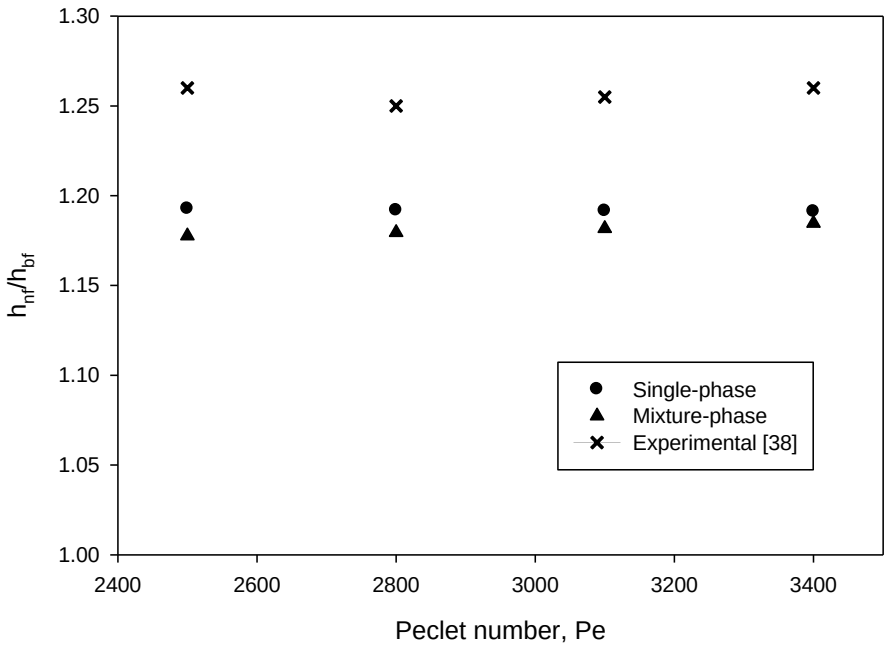

Fig. 6.20: Comparison of convective heat transfer coefficient ratio of nanofluid and base fluid for different study models

Table 6.2: Comparison between current results and the results by Heris et al. [38]

Peclet number, Pe	Convective heat transfer coefficient ratio, h_{nf}/h_{bf}		
	Single-phase	Mixture-phase	Experimental [38]
2500	1.193	1.178	1.260
2800	1.192	1.180	1.250
3100	1.192	1.182	1.255
3400	1.191	1.185	1.260

6.2 Flat Plate Collector Results

6.2.1 Results with Nanofluid

In this study, the effect of Al_2O_3-water nanofluid on the thermal performance of flat plate solar collector is studied. The solar collector is studied with three different flow rates of 0.015 mL/s, 0.025 mL/s and 0.035 mL/s. These flow rates are the total flow rates of all eight of the riser tubes in the flat plate collector. Each of these flow rates are then studied with three different nanoparticle volume fractions of 1%, 3% and 5%.

The temperature of the absorber plate along the length at various width sections is plotted in Fig. 6.21. The temperature on both sides of the riser pipe is symmetric and so, only the temperature at one side of the riser tube is plotted here. The temperatures are found from the flat plate collector with water as the working fluid for a flow rate of 0.025 mL/s. From the plots, it is seen that the plots for w/W=0 and w/W=0.025 are same. This is because it is assumed that the plate temperature of about half of the riser tube radius amount on each side from the collector plate middle axis is same. After these two plots, the temperature is plotted with a constant interval. It is seen from the plots that the collector temperature difference between plots decreases as it reaches near the edge. This is because of the insulated edge of the collector. A surface temperature plot of the absorber plate is given in Fig. 6.22.

Fig. 6.23 shows the absorber temperature at the middle of the plate for various flow rates of water. With the increase in flow rates, the absorber temperature decreases and as a result the useful solar radiation increases. So, for an increase in solar plate efficiency, solar absorber temperature has to be reduced which can also be seen from equation (5.23). The results here are for constant overall heat loss coefficient and from equation (5.23), it is seen that the plate average temperature must reduce for an increase in the useful solar energy. Absorber plate temperature drops more for the flow rate increase from 0.015 mL/s to 0.025 mL/s than the increase from 0.025 mL/s to 0.035 mL/s. So, the relative increase in efficiency tends to decrease with the increase of flow rates. Fig. 6.24 shows the plots of bulk and surface temperature of the riser tube for various flow rates. It shows that, both the bulk and surface temperature decrease with the increase of flow rates. Decrease in surface temperature means increase in useful heat. Although the bulk temperature deceases with flow rates, the useful energy increases because the mass flow rate increases with increasing flow rates. The surface temperature changes parabolically, while the bulk temperature increase is almost in straight lines along the length.

The heat flux at the surface of the riser tube is plotted in Fig. 6.25 for various flow rates. After a sudden decrease at the entrance, the heat flux gradually decreases up until the outlet. Near the outlet, the decrease is slightly higher which could be because of the insulated condition of the absorber plate at outlet. This plot shows us that the boundary condition of the riser tube wall is nor constant wall temperature or neither constant wall heat flux. Although the heat flux distribution along the length of the tube resembles more with the constant wall heat flux condition. Fig. 6.26 shows the plots of bulk and surface temperature of the riser pipe for water and nanofluid of 3% volume concentrations of nanoparticles. While a significant decrease in surface temperature is visible, the bulk temperature of the two fluids is almost same where the nanofluid bulk temperature is slightly low. The results are obtained for a flow rate of 0.025 mL/s. For the same flow rate, mass flow rate of nanofluid is higher than water. So, although bulk temperature reduces slightly, the useful heat is higher for nanofluid because of the increased mass flow rate.

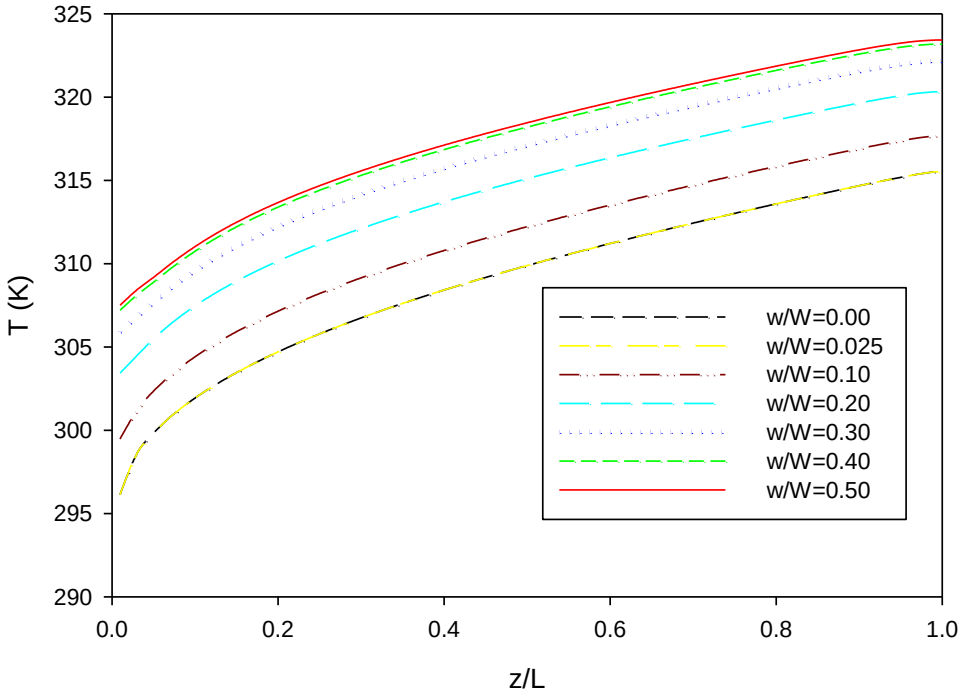

Fig. 6.21: Absorber plate temperature along the length at various width sections

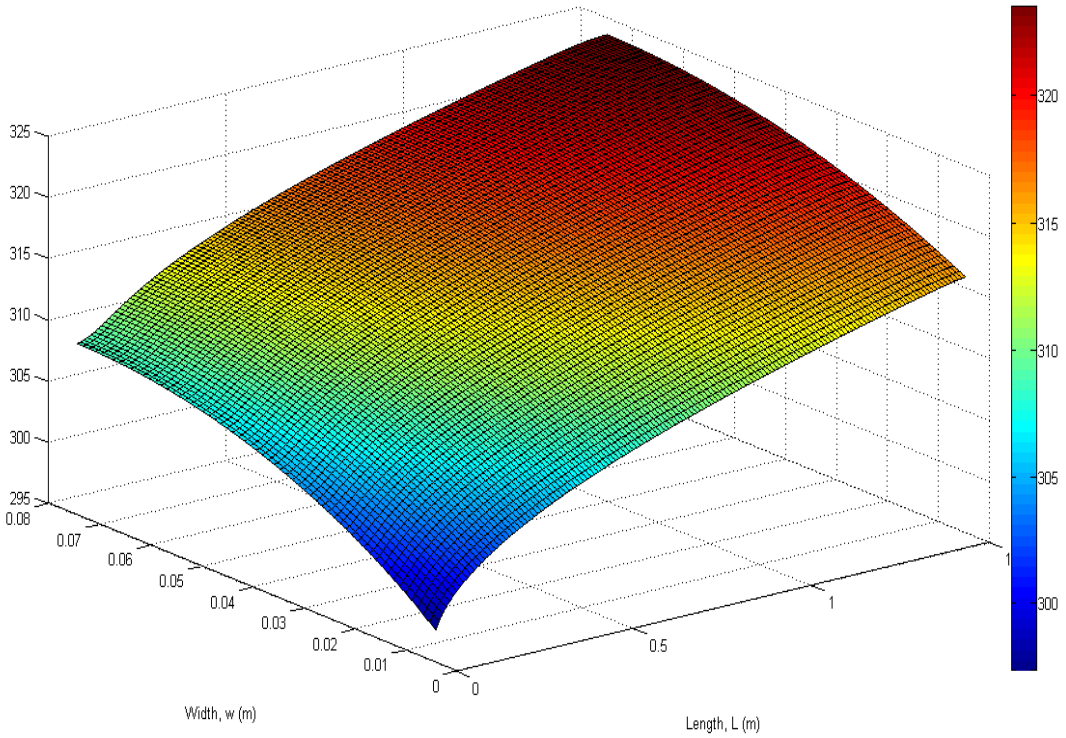

Fig. 6.22: Surface plot of absorber plate temperature

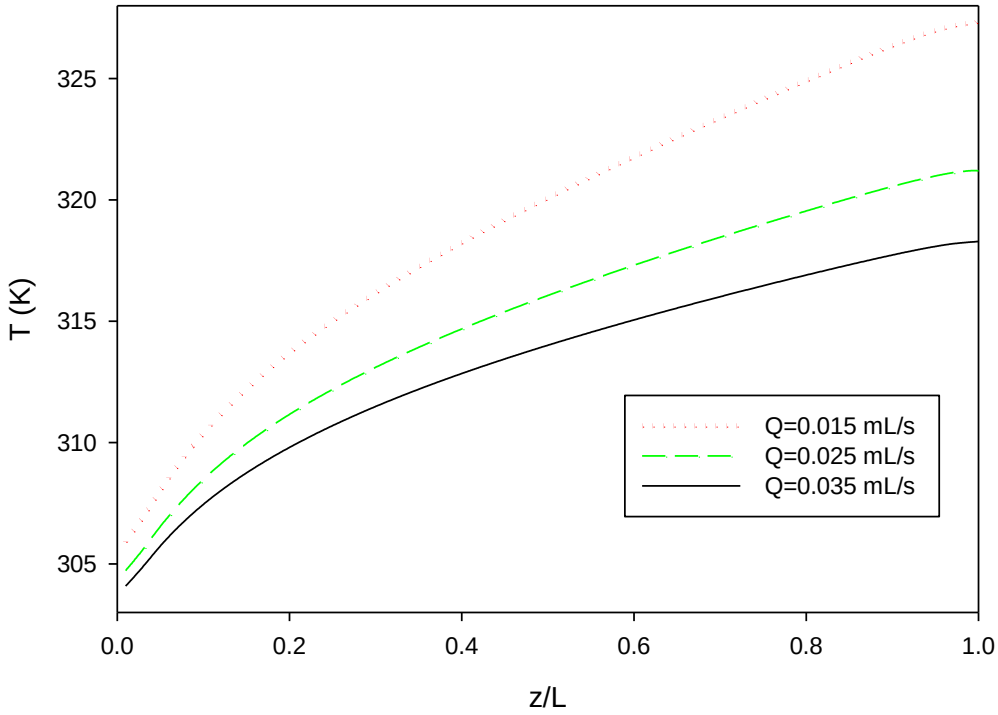

Fig. 6.23: Temperature at the middle of the absorber plate for various flow rates

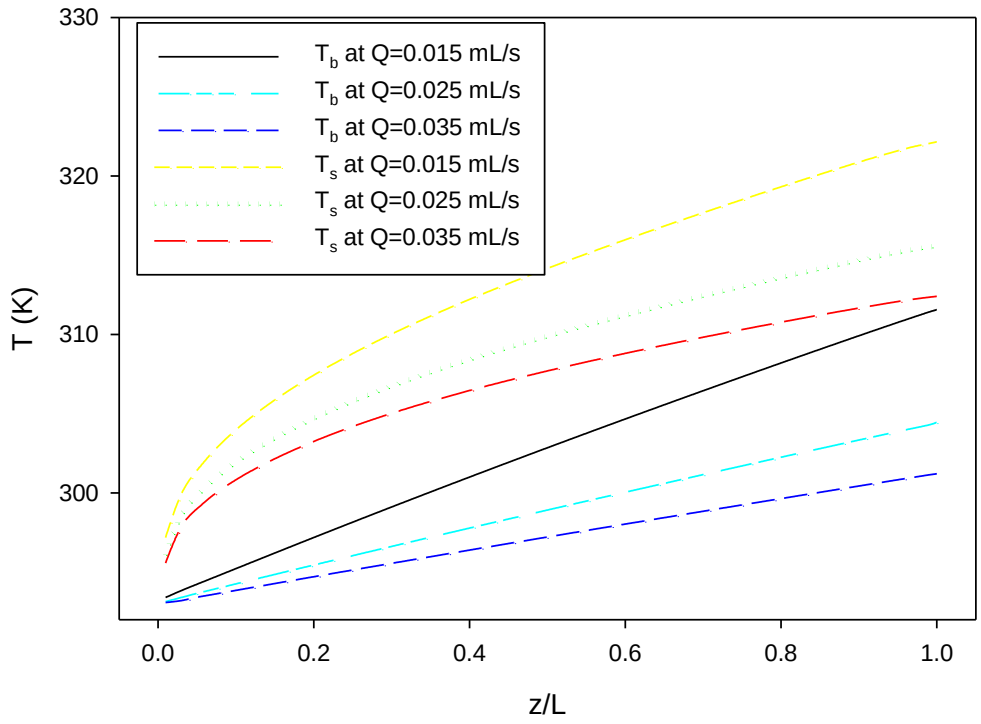

Fig. 6.24: Bulk and surface temperature of the riser tube for various flow rates

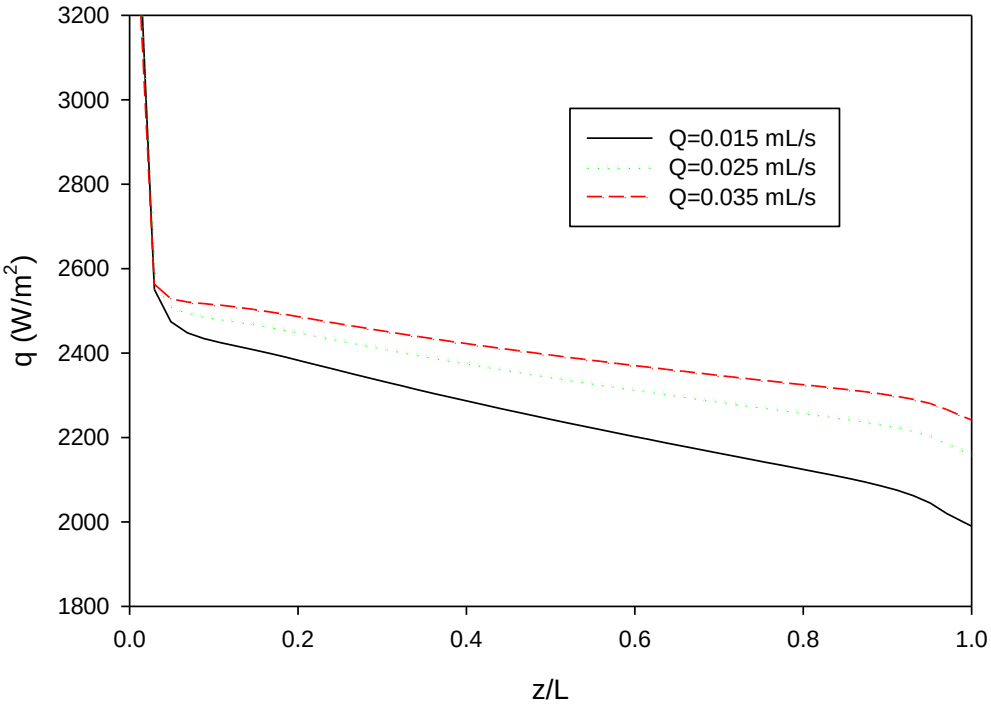

Fig. 6.25: Surface heat flux of the riser tube for various flow rates

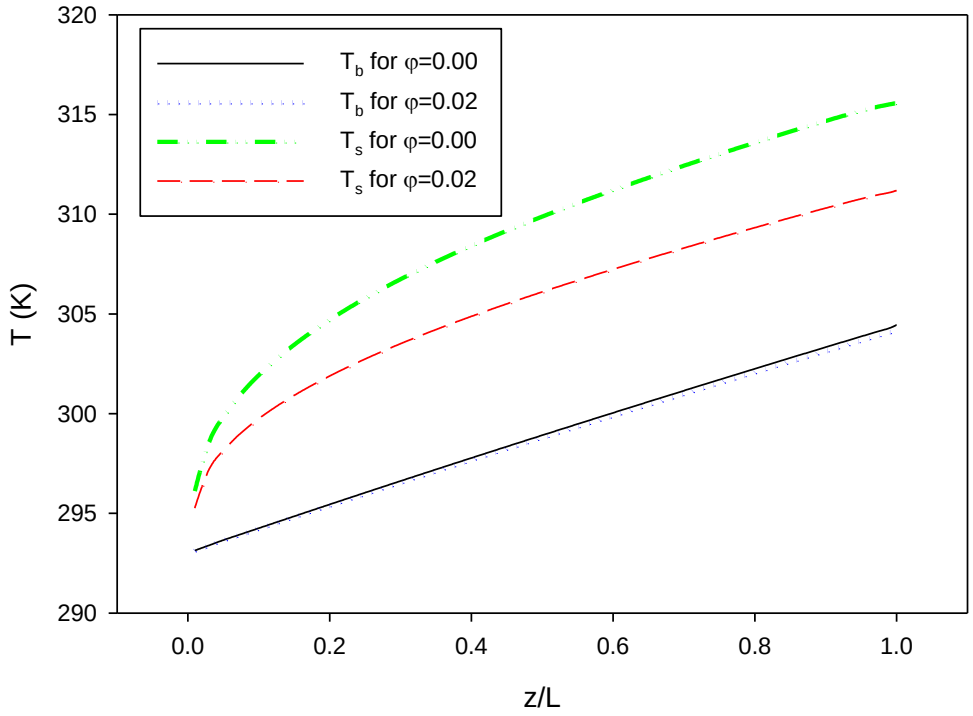

Fig. 6.26: Bulk and surface temperature of the riser tube for water and nanofluid

The efficiency of the flat plate solar collector for Al_2O_3-water nanofluid is plotted against $(T_{in}-T_{\alpha})/I_t$ in Fig. 6.27. The figure is for a flow rate of 0.015 mL/s through the solar collector. The efficiencies are for a constant overall heat loss coefficient of 7 W/m^2K. The efficiency decreases almost linearly with the increase of $(T_{in}-T_{\alpha})/I_t$ term. There are seven different plots of efficiency in Fig. 6.27. These plots are for different nanoparticle volume fractions studied by both single-phase and mixture-phase model. While, both the single-phase and mixture-phase model demonstrates increased efficiency with increasing nanoparticle concentration, the mixture model gives slightly lower efficiency than the single-phase model. This is due to the lower convective heat transfer coefficient demonstrated by the mixture model. The nanoparticle volume percentages studied here are 1%, 3% and 5%. The relative increase in the efficiency of the collector reduces with the increase of the particle concentration. The efficiency increases by 6.6% and 6.3% for the nanofluid with 5% nanoparticles as found by the single-phase and mixture-phase study respectively. The same plots are made for flow rates of 0.025 mL/s and 0.035 mL/s in Fig. 6.28 and Fig. 6.29 respectively. The efficiency increases greatly with the increase of flow rates but again the relative increase reduces with the increase of flow rates. The efficiency values for different flow rates and nanoparticle volume fractions are listed in table 6.2. From the table, it can be seen that the variation between the single-phase and mixture-phase results are very small and since the single-phase model requires less time and memory for computation, only the single-phase model of nanofluids is used hereafter.

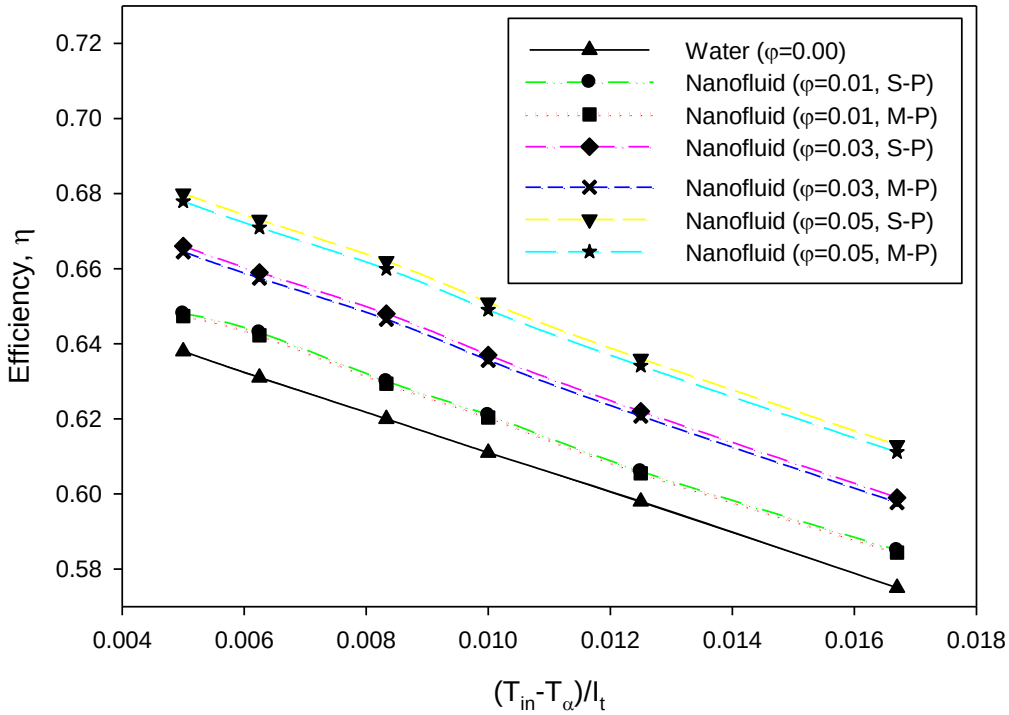

Fig. 6.27: Flat plate collector efficiency for various nanoparticle volume fractions at Q=0.015 mL/s

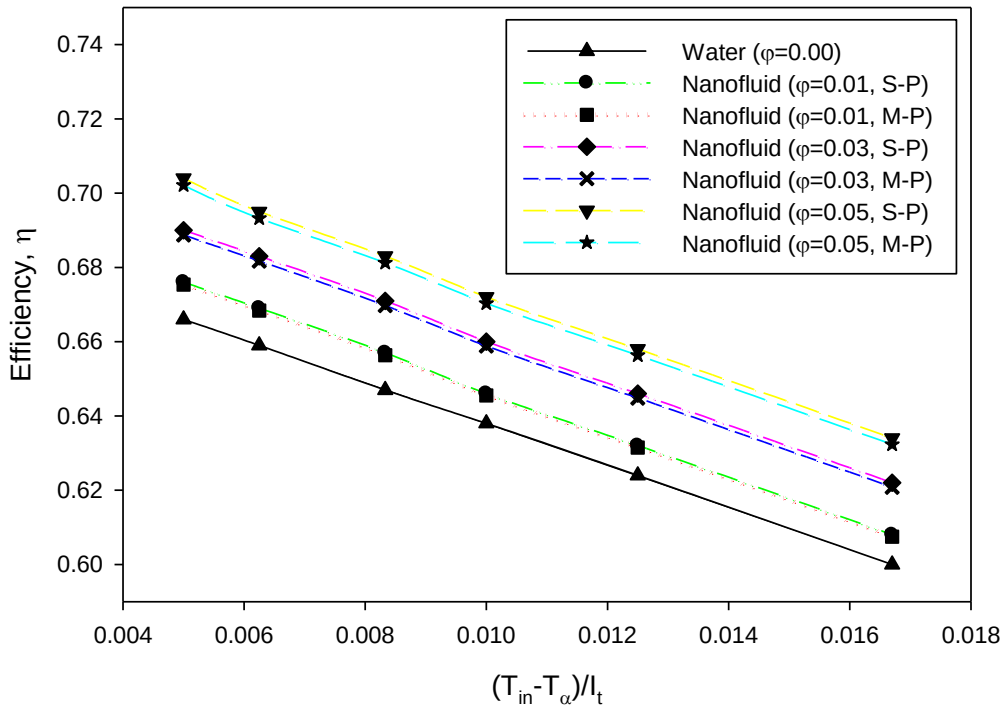

Fig. 6.28: Flat plate collector efficiency for various nanoparticle volume fractions at Q=0.025 mL/s

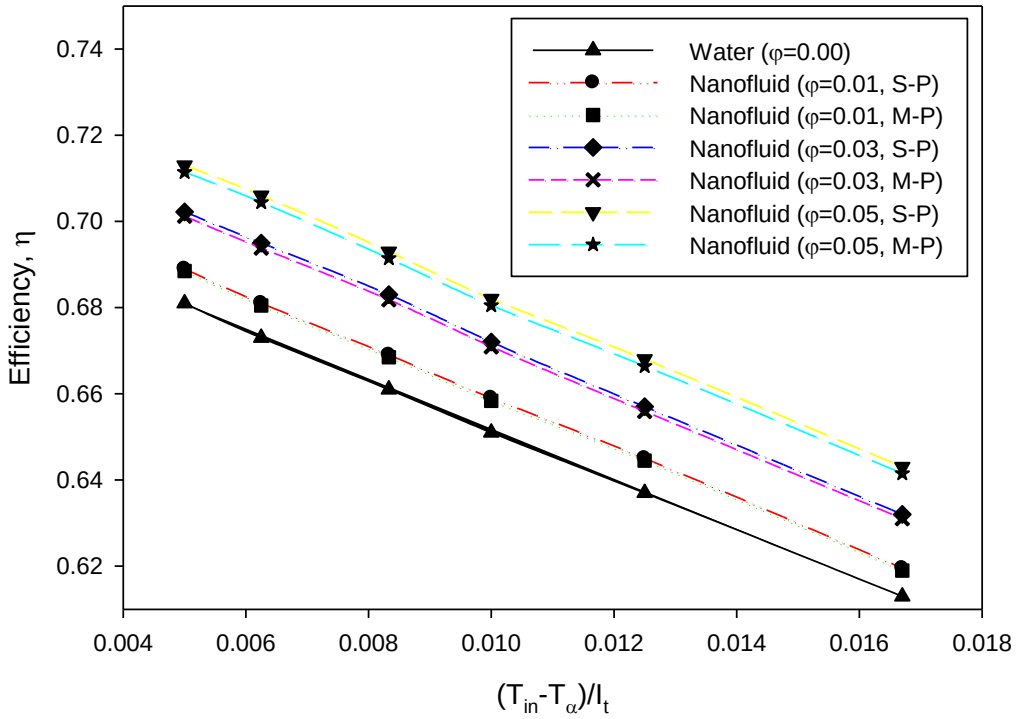

Fig. 6.29: Flat plate collector efficiency for various nanoparticle volume fractions at Q=0.035 mL/s

Table 6.3: Flat plate collector efficiencies for various flow rates and volume fractions

Flow rate, Q (mL/s)	Nanoparticle volume fraction		$(T_{in}-T_{\alpha})/I_t$ ($°Cm^2/W$)					
			0.005	0.0063	0.0083	0.01	0.0125	0.0167
15	φ=0.00		0.638	0.631	0.620	0.611	0.598	0.575
	φ=0.01	S-P	0.648	0.643	0.630	0.621	0.606	0.585
		M-P	0.647	0.642	0.629	0.620	0.606	0.584
	φ=0.03	S-P	0.666	0.659	0.648	0.637	0.622	0.599
		M-P	0.664	0.657	0.646	0.636	0.621	0.598
	φ=0.05	S-P	0.680	0.673	0.662	0.651	0.636	0.613
		M-P	0.678	0.671	0.660	0.649	0.634	0.611
25	φ=0.00		0.666	0.659	0.647	0.638	0.624	0.600
	φ=0.01	S-P	0.676	0.669	0.657	0.646	0.632	0.608
		M-P	0.675	0.668	0.656	0.646	0.632	0.608
	φ=0.03	S-P	0.690	0.683	0.671	0.660	0.646	0.622
		M-P	0.689	0.682	0.670	0.659	0.645	0.621
	φ=0.05	S-P	0.704	0.695	0.683	0.672	0.658	0.634
		M-P	0.702	0.693	0.681	0.670	0.656	0.632
35	φ=0.00		0.681	0.673	0.661	0.651	0.637	0.613
	φ=0.01	S-P	0.689	0.681	0.669	0.658	0.645	0.619
		M-P	0.689	0.681	0.669	0.658	0.645	0.619
	φ=0.03	S-P	0.702	0.695	0.683	0.672	0.657	0.633
		M-P	0.701	0.694	0.682	0.671	0.656	0.632
	φ=0.05	S-P	0.713	0.707	0.693	0.682	0.669	0.643
		M-P	0.711	0.705	0.691	0.681	0.667	0.642

This study uses another nanofluid namely CuO-water for the performance evaluation of the flat plate collector. The effective conductivity of CuO-water nanofluid is higher than the Al_2O_3-water nanofluid. A flow rate of 0.025 mL/s is considered for the study. The efficiencies found from the CuO-water nanofluid are plotted in Fig. 6.30. Only the single-phase model is applied here. The results show higher efficiency of the solar collector than that found by Al_2O_3-water nanafluid. The efficiency reaches as high as 72.3% for 5% volume fraction of CuO nanoparticle

which is 8.6% higher than that of water as the working fluid. The results of CuO-water nanofluid are listed in table 6.4. The results indicate that, the CuO-water naofluid is a better choice as the working fluid for the flat plate solar collector than the Al_2O_3-water nanofluid.

All the above studies on thermal performance of flat plate collector are done using constant overall heat loss coefficient. However, in practice, the overall heat loss coefficient is not constant and depends on flat plate temperature and many other parameters which is described in detail in section 4.1.5. This thesis work also performs a study of the flat plate collector with variable overall heat loss coefficient, U_L. The efficiencies found by the variable U_L are plotted in Fig. 6.31 and Fig. 6.32 for Al_2O_3-water and CuO-water nanofluid. The plots are made for a flow velocity of 0.022 m/s. The value of U_L calculated with equation (4.16) is lower than the constant value of 7 W/m^2K considered in previous studies. As a result the efficiencies found by variable U_L are relatively higher than the constant U_L. However, the increase of the collector efficiency for the nanofluids gets reduced. While the efficiency increases by 6.6% for 5% volume fraction of Al_2O_3-water nanofluid with constant U_L, the efficiency increases by 4.8% for variable U_L. The solar plate efficiencies found by variable U_L are listed in table 6.5 for Al_2O_3-water and CuO-water nanofluids.

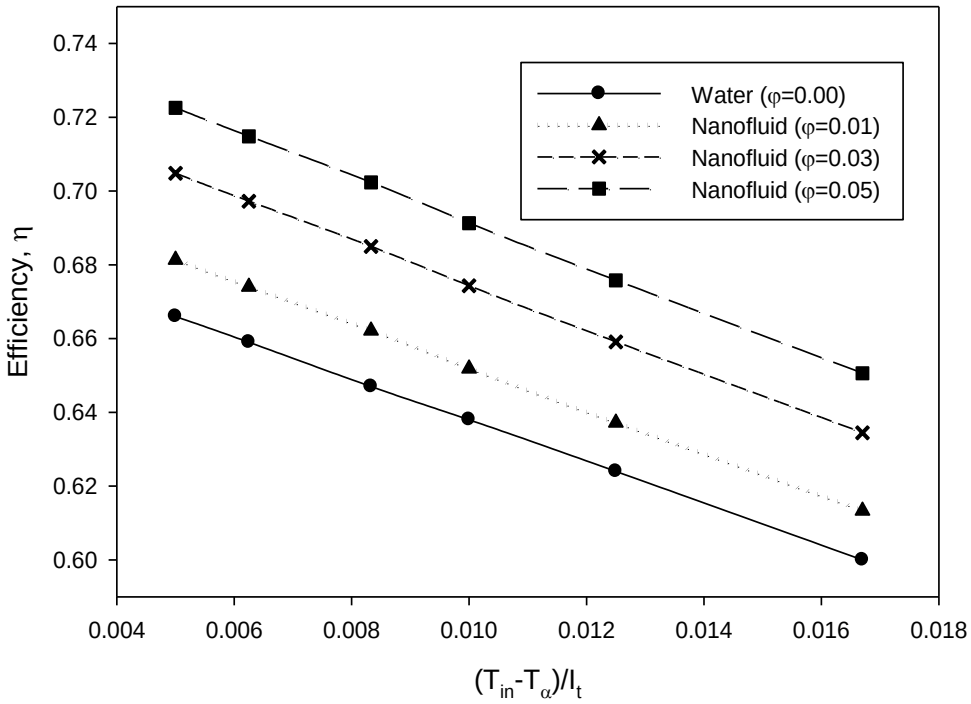

Fig. 6.30: Flat plate collector efficiency of CuO-water nanofluid for various volume fractions

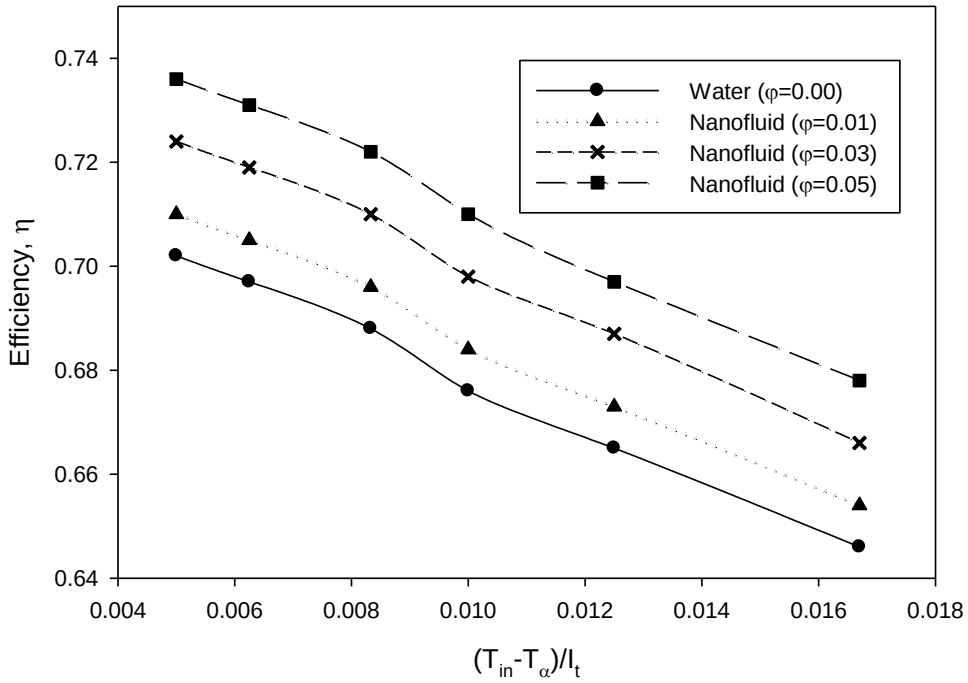

Fig. 6.31: Flat plate collector efficiency with variable overall heat loss coefficient for Al_2O_3-water nanofluid

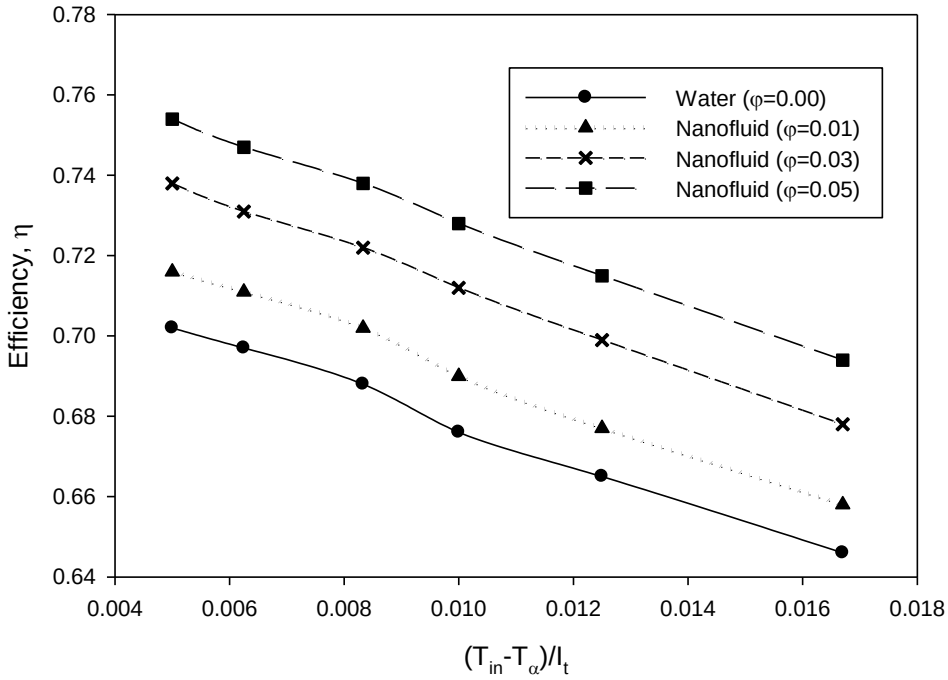

Fig. 6.32: Flat plate collector efficiency with variable overall heat loss coefficient for CuO-water nanofluid

Table 6.4: Flat plate collector efficiencies of CuO-water nanofluids with constant U_L

Nanofluid	Nanoparticle volume fraction	$(T_{in}-T_\alpha)/I_t$ ($°Cm^2/W$)					
		0.005	0.0063	0.0083	0.01	0.0125	0.0167
CuO-water	φ=0.00	0.666	0.659	0.647	0.638	0.624	0.600
	φ=0.01	0.681	0.674	0.662	0.652	0.637	0.613
	φ=0.03	0.705	0.697	0.685	0.674	0.659	0.634
	φ=0.05	0.723	0.715	0.702	0.691	0.676	0.651

Table 6.5: Flat plate collector efficiencies for the two nanofluids with variable U_L

Nanofluid	Nanoparticle volume fraction	$(T_{in}-T_\alpha)/I_t$ ($°Cm^2/W$)					
		0.005	0.0063	0.0083	0.01	0.0125	0.0167
Al_2O_3-water	φ=0.00	0.702	0.697	0.688	0.676	0.665	0.646
	φ=0.01	0.710	0.705	0.696	0.684	0.673	0.654
	φ=0.03	0.724	0.719	0.710	0.698	0.687	0.666
	φ=0.05	0.736	0.731	0.722	0.71	0.697	0.678
CuO-water	φ=0.00	0.702	0.697	0.688	0.676	0.665	0.646
	φ=0.01	0.716	0.711	0.702	0.690	0.677	0.658
	φ=0.03	0.738	0.731	0.722	0.712	0.699	0.678
	φ=0.05	0.754	0.747	0.738	0.728	0.715	0.694

6.2.2 Results with Finned Tube

The performance of the flat plate collector is also investigated by changing the internal structure of riser tube. The study uses two different fins on the inner surface of the riser tube. This study involves 3-D investigation with FEM discretization. Here also a flow rate of 0.025 mL/s is considered. The efficiencies found from these two fins with water as the working fluid is plotted in Fig. 6.33. While fin-1 doesn't produce that much of increment, the increment from fin-2 is quite significant. The efficiency increases by about 1.95% and 10.9% for fin-1 and fin-2 respectively. The efficiency values are given in table 6.6. A surface plot of the absorber plate

temperature is given in Fig. 6.34. The plot shows that temperature increases with the length and width of the absorber plate.

Table 6.6: Flat plate collector efficiencies for different fin configurations

Riser tube fin configurations	$(T_{in}-T_{\alpha})/I_t$ ($°Cm^2/W$)					
	0.005	0.0063	0.0083	0.01	0.0125	0.0167
No fin	0.664	0.658	0.646	0.637	0.622	0.599
Fin-1	0.678	0.670	0.659	0.649	0.635	0.610
Fin-2	0.738	0.730	0.719	0.706	0.690	0.665

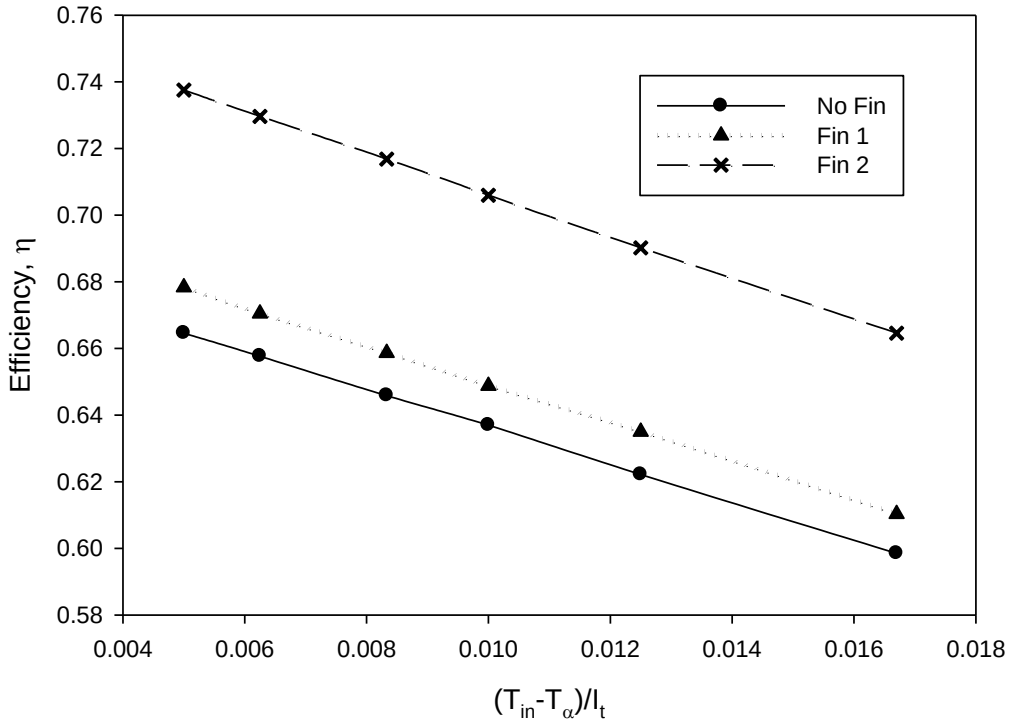

Fig. 6.33: Flat plate collector efficiency for various fin configurations of the riser tube

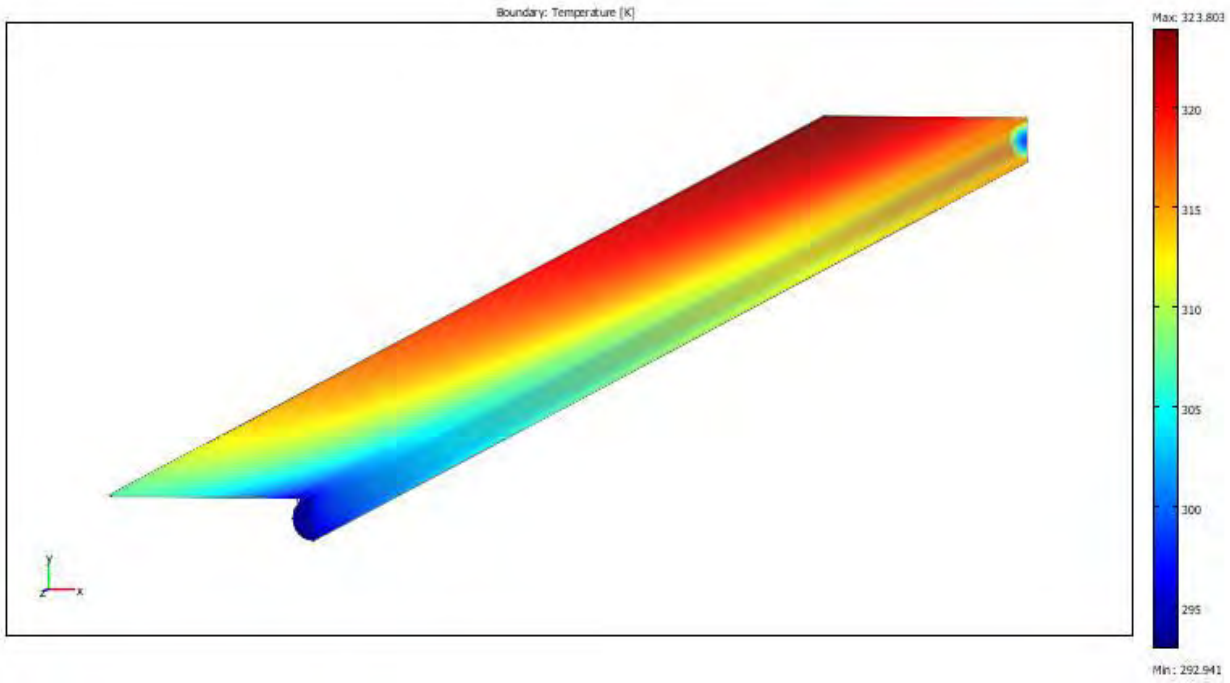

Fig. 6.34: Temperature plot of flat plate collector in 3D

Finally, the pressure required by different working fluids for a flow rate of 0.025 mL/s is listed in table 6.7. Also the efficiencies produced by the working fluids are listed next to the pressure. It is seen that, while the efficiency found from the CuO-water nanofluid is always higher than the Al_2O_3-water nanofluid, this is not the case for pressure. For 1% nanoparticle volume fraction, pressure required by CuO-water nanofluid is higher; for 3% volume fraction, pressure required by Al_2O_3-water nanofluid is higher and for 5% volume fraction, pressure required by CuO-water is higher again. The pressure required by the two fin types are also listed in table 6.7. Compared to the efficiency increase of fin-1, the pressure increase is more. While a significant increase in efficiency is found by fin-2, it also requires much higher pressure than the other types. So, nanofluids are a good choice to increase the efficiency of a flat plate collector. On the other hand, use of a fin in riser tube is simple and requires less maintenance, so use of fins is also a good option for flat plate collector.

Table 6.7: Pressure difference required by different working fluids

Working Fluid		Pressure difference (Pa)	Efficiency
FVM Analysis			
Water		5.56	0.666
Al_2O_3-water nanofluid	$\varphi = 0.01$	6.29	0.676
	$\varphi = 0.03$	8.37	0.690
	$\varphi = 0.05$	11.16	0.704
CuO-water nanofluid	$\varphi = 0.01$	7.25	0.681
	$\varphi = 0.03$	7.31	0.705
	$\varphi = 0.05$	13.38	0.723
FEM Analysis			
Water	No fin	5.81	0.665
Water	Fin-1	9.08	0.678
Water	Fin-2	34.43	0.738

Chapter 7

Conclusions

In this thesis, the hydrodynamic and thermal behaviors of Al_2O_3-water nanofluid are studied first in a circular pipe by using single-phase and mixture-phase models. The nanofluid is then applied to a flat plate solar collector to increase the thermal performance of the collector. CuO-water nanofluid is also used in the solar collector and the performances are compared with the Al_2O_3-water nanofluid. Investigations are also made with variable heat loss coefficient with both the nanofluids. Finally riser tube internal geometries are changed by incorporating fins to check the improvements of the collector.

The major conclusions of Al_2O_3-water nanofluid study are:

- Convective heat transfer coefficient increases significantly with nanoparticle volume fraction for the same Reynolds number. The increment is higher for single-phase model than the mixture-phase model of Buongiorno [17]. The convective coefficient also increases with the Reynolds number.

- Nusselt number varies slightly with the nanoparticle volume fraction for the same Reynolds number. For lower values of volume fraction, the mixture-phase model gives slightly lower values of Nusselt number than the base fluid, while for higher volume fraction, Nusselt number is higher than the base fluid. The single-phase study demonstrates slightly higher Nusselt number than base fluid both for lower and higher volume fraction. Nusselt number also increases with the Reynolds number.

- The wall shear stress increases with the nanoparticle volume fraction. The increment rate tends to increase towards higher volume fraction of nanoparticle. The mixture-phase model gives lower values of shear stress than the single-phase model.

- The mixture-phase model gives the nanoparticle distribution in the flow domain. Nanoparticle concentration tends to reduce near the wall and the reduction increases

towards the outlet section. The reduced volume fraction near the wall inevitably causes the reduced heat transfer coefficient than that found by the single-phase model.

The major findings from the solar plate study are:

- The efficiency of the solar plate collector increases for Al_2O_3-water nanofluid by 6.6% for 5% volume fraction of nanoparticle given by single-phase study. The mixture-phase model gives slightly lower value of 6.3% for the same volume fraction.

- The CuO-water nanofluid gives higher efficiency of the flat plate collector than the Al_2O_3-water nanofluid. The efficiency increases by 8.6% for 5% volume fraction of CuO nanoparticle.

- The variable overall heat loss coefficient gives higher values of efficiency but the efficiency increment by the nanofluids reduces. That's because the variable overall heat loss coefficient is lower than that of the constant value considered in other studies.

- The efficiency of the flat plate collector can also be improved by incorporating internal fins to the riser tubes. While fin-1 doesn't improve the result much, fin-2 increases the efficiency by 10.3%.

Recommendations:

- Use of effective conductivity and viscosity correlation that depends on nanoparticle volume fraction, particle size, temperature etc. may provide better results.

- A comparative study between the increase in energy extracted from the collector and the increase in pumping work might be done.

- Other nanofluids can be considered for the flat plate collector and also other types of solar thermal collectors can be considered.

- Other fin configurations can be considered for the performance improvement of the solar collector.

References

[1] Maxwell, J.C., "A Treatise on Electricity and Magnetism," second ed., pp. 435-441, Oxford University Press, Cambridge, 1904.

[2] Jeffrey, D.J., "Conduction through a random suspension of spheres," *Proceedings of the Royal Society of London*, Series A 335, pp. 355–367 *(1973)*.

[3] Xuan, Y., and Li, Q., "Heat Transfer Enhancement of Nanofuids," *Int. J. Heat Fluid Fl.*, vol. 21, pp. 58-64, 2000.

[4] Boothroyd, R.G., and Haque, H., "Fully Developed Heat Transfer to a Gaseous Suspension of Particles Flowing Turbulently in Duct of Different Size," *J. Mech. Eng. Sci.*, vol. 12 (3), pp. 191–200, 1970.

[5] Sohn, C.W., and Chen, M.M., "Microconvective Thermal Conductivity in Disperse Two-Phase Mixtures as Observed in a Low Velocity Couette Flow Experiment", *J. Heat Transfer,* vol. 103, pp. 45–51, 1981.

[6] Choi, S.U.S., "Enhancing Thermal Conductivity of Fluids with Nanoparticles," *Developments and Applications of Non- Newtonian Flows*, D. A. Siginer and H. P. Wang (eds.), ASME, FED-vol. 231, MD-vol. 66, pp. 99-105, 1995.

[7] Ding, Y., Alias, H., Wen, D., and Williams, R.A., "Heat Transfer of Aqueous Suspensions of Carbon Nanotubes (CNT nanofluids)," *Int. J. Heat Mass Tran.*, vol. 49, pp. 240–250, 2006.

[8] He, Y., Jin, Y.,, Chen, H., Ding, Y., Cang, D., and Lu, H., "Heat Transfer and Flow Behaviour of Aqueous Suspensions of TiO2 Nanoparticles (nanofluids) Flowing Upward Through a Vertical Pipe," *Int. J. Heat Mass Tran.*, vol. 50, pp. 2272–2281, 2007.

[9] Davarnejad, R., Barati, S., and Kooshki, M., "CFD Simulation of the Effect of Particle Size on the Nanofluids Convective Heat Transfer in the Developed Region in a Circular Tube," SpringerPlus, 2:192, 2013.

[10] A.M. Hussein, R.A. Bakar, K. Kadirgama, and K.V. Sharma, "Experimental Measurement of Nanofluids Thermal Properties", *International Journal of Automotive and Mechanical Engineering*, Vol. 7, pp. 850-863 (2013).

[11] Abbasi, S., Zebarjad, S.M., Baghban, S.H.N., and Youssefi, A., "Statistical Analysis of Thermal Conductivity of Nanofluid Containing Decorated Multi-Walled Carbon Nanotubes with TiO_2 Nanoparticles," ***Bull. Mater. Sci.***, vol. 37, no. 6, pp. 1439–1445, 2014.

[12] Sridhara, V., and Satapathy, L.N., "Al_2O_3-based nanofluids: a review," ***Nanoscale Res. Lett.***, 6:456, 2011.

[13] Mahbubul, I.M., Rahman, S., Amalina, M.A., "Latest developments on the viscosity of nanofluids," ***Int. J. Heat Mass Tran.***, vol. 55, pp. 874–885, 2012.

[14] Kalteh, M., Abbassi, A., Saffar-Avval, M., and Harting, J., "Eulerian–Eulerian Two-phase Numerical Simulation of Nanofluid Laminar Forced Convection in a Microchannel," ***Int. J. Heat Fluid Fl.***, vol. 32, pp. 107–116, 2011.

[15] Bianco, V., Chiacchio, F., Manca, O., and Nardini, S., "Numerical Investigation of Nanofluids Forced Convection in Circular Tubes," ***Appl. Therm. Eng.***, vol. 29, pp. 3632–3642, 2009.

[16] Behzadmehr, A., Saffar-Avval, M., and Galanis, N., "Prediction of Turbulent Forced Convection of a Nanofluid in a Tube with Uniform Heat Flux Using a Two Phase Approach," ***Int. J. Heat Fluid Fl.***, vol. 28, pp. 211-219, 2007.

[17] Buongiorno, J., "Convective Transport in Nanofluids," ***J. Heat Transf.***, vol. 128, pp. 240-250, 2006.

[18] Dović, D., and Andrassy, M., "Numerically Assisted Analysis of Flat and Corrugated Plate Solar Collectors Thermal Performances," ***Sol. Energy***, vol. 86, pp. 2416–2431, 2012.

[19] Sultana, T., Morrison, G.L., and Rosengarten, G., "Thermal Performance of a Novel Rooftop Solar Micro-Concentrating Collector," ***Sol. Energy***, vol. 86, pp. 1992–2000,

2012.

[20] Helmers, H., and Kramer, K., "Multi-Linear Performance Model for Hybrid (C)PVT Solar Collectors", ***Sol. Energy***, vol. 92, pp. 313–322, 2013.

[21] Kalogirou, S.A., "Solar Thermal Collectors and Applications," ***Prog. Energ. Combust.***, vol. 30, pp. 231–295, 2004.

[22] Manjunath, M.S., Karanth, K.V., and Sharma, N.Y., "Three Dimensional Numerical Analysis of Conjugate Heat Transfer for Enhancement of Thermal Performance using Finned Tubes in an Economical Unglazed Solar Flat Plate Collector", ***Proceedings of the World Congress on Engineering,*** Vol. III, Jul. 2011, London, U.K. ***(2011).***

[23] Rassamakin, B., Khairnasov, S., Zaripov, V., Rassamakin, A., and Alforova, O., "Aluminum Heat Pipes Applied in Solar Collectors," ***Sol. Energy***, vol. 94, pp. 145–154, 2013.

[24] Chaji, H., Ajabshirchi, Y., Esmaeilzadeh, E., Heris, S.Z., Hedayatizadeh, M., and Kahani, M., "Experimental Study on Thermal Efficiency of Flat Plate Solar Collector Using TiO_2/Water Nanofluid," ***Modern Applied Science***, vol. 7, no. 10, pp. 60-69, 2013.

[25] Jamal-Abad, M.T., Zamzamian, A., Imani, E., and Mansouri, M., "Experimental Study of the Performance of a Flat-plate Collector Using Cu–water Nanofluid," ***J. Thermophys. Heat Tr.***, doi: 10.2514/1.T4074.

[26] R. Nasrin, and M.A. Alim, "Finite Element Simulation of Forced Convection in a Flat Plate Solar Collector: Influence of Nanofluid with Double Nanoparticles", ***Journal of Applied Fluid Mechanics***, Vol. 7, No. 3, pp. 543-556 (2014).

[27] Masuda, H., Ebata, A., Teramae, K., and Hishinuma, N., 1993 "Alteration of Thermal Conductivity and Viscosity of Liquid by Dispersing Ultrafine Particles (Dispersion of γ-Al_2O_3, SiO_2 And TiO_2 Ultra-Fine Particles). Netsu Bussei (in Japanese), vol. 4 (4), pp. 227–233, 1993.

[28] Pak, B. C., and Cho, Y., "Hydrodynamic and Heat Transfer Study of Dispersed Fluids With Submicron Metallic Oxide Particles," Exp. Heat Transfer, vol. 11, pp. 151–170, 1998.

[29] Xuan, Y., and Li, Q., "Heat Transfer Enhancement of Nanofluids," ***Int. J. Heat Fluid***

Fl., vol. 21, pp. 58–64, 2000.

[30] Lee, S., Choi, S.U.S., Li, S., and Eastman, J.A., "Measuring Thermal Conductivity of Fluids Containing Oxide Nanoparticles," J. Heat Transfer, vol. 121, pp. 280–289, 1999.

[31] Das, S.K., Putra, N., Thiesen, P., and Roetzel, W., "Temperature Dependence of Thermal Conductivity Enhancement for Nanofluids," J. Heat Transfer, vol. 125, pp. 567–574, 2003.

[32] Kakaç, S., and Pramuanjaroenkij, A., "Review of Convective Heat Transfer Enhancement with Nanofluids," *Int. J. Heat Mass Tran.,* vol. 52, pp. 3187–3196, 2009.

[33] Wang, X.Q., and Mujumdar, A.S., "Heat Transfer Characteristics of Nanofluids: a Review," *Int. J. Therm. Sci*., vol. 46, pp. 1–19, 2007.

[34] Wang, X.Q., and Mujumdar, A.S., "A Review on Nanofluids - Part II:Experiments and Applications," *Braz. J. Chem. Eng.*, vol. 25, no. 04, pp. 631 - 648, 2008.

[35] Chandrasekar, M., Suresh, S., and Senthilkumar, T., "Mechanisms Proposed Through Experimental Investigations on Thermophysical Properties and Forced Convective Heat Transfer Characteristics of Various Nanofluids – a Review," *Renew. Sust. Energ. Rev.*, vol. 16, pp. 3917– 3938, 2012.

[36] Khanafer, K., and Vafai, K., "A Critical Synthesis of Thermophysical Characteristics of Nanofluids," *Int. J. Heat Mass Tran.*, vol. 54, pp. 4410–4428, 2011.

[37] Wen, D., and Ding, Y., "Experimental Investigation into Convective Heat Transfer of Nanofluids at the Entrance Region under Laminar Flow Conditions," *Int. J. Heat Mass Tran.*, vol. 47, pp. 5181–5188, 2004.

[38] Heris, S.Z., Esfahany, M.N., and Etemad, S.G., "Experimental Investigation of Convective Heat Transfer of Al_2O_3/Water Nanofluid in Circular Tube," *Int. J. Heat Fluid Fl.*, vol. 28, pp. 203–210, 2007.

[39] He, Y., Jin, Y., Chen, H., Ding, Y., Cang, D., and Lu, H., "Heat Transfer and Flow Behaviour of Aqueous Suspensions of TiO_2 Nanoparticles (Nanofluids) Flowing Upward Through a Vertical Pipe," *Int. J. Heat Mass Tran.*, vol. 50, pp. 2272–2281, 2007.

[40] Ding, Y., Alias, H., Wen, D., and Williams, R.A., "Heat Transfer of Aqueous

Suspensions of Carbon Nanotubes (CNT Nanofluids)," ***Int. J. Heat Mass Tran.***, vol. 49, pp. 240–250, 2006.

[41] Chen, H., Yang, W., He, Y., Ding, Y., Zhang, L., Tan, C., Lapkin, A.A., and Bavykin, D.V., "Heat Transfer and Flow Behaviour of Aqueous Suspensions of Titanate Nanotubes (Nanofluids)," ***Powder Technol.***, vol. 183, pp. 63–72, 2008.

[42] Maïga, S.E.B., Palm, S.J., Nguyen, C.T., Roy, G., and Galanis, N., "Heat Transfer Enhancement by Using Nanofluids in Forced Convection Flows," ***Int. J. Heat Fluid Fl.***, vol. 26, pp. 530–546, 2005.

[43] Demir, H., Dalkilic, A.S., Kürekci, N.A., Duangthongsuk, W., and Wongwises, S., "Numerical Investigation on the Single Phase Forced Convection Heat Transfer Characteristics of TiO_2 Nanofluids in a Double-tube Counter Flow Heat Exchanger," ***Int. Commun. Heat Mass***, vol. 38, pp. 218–228, 2011.

[44] W. Rashmi, W., Ismail, A.F., and Khalid, M., and Faridah, Y., "CFD Studies on Natural Convection Heat Transfer of Al_2O_3-Water Nanofluids," ***Heat Mass Transfer***, vol. 47, pp. 1301–1310, 2011.

[45] Kalteh, M., Abbassi, A., Saffar-Avval, M., Frijns, A., Darhuber, A., and Harting, J., "Experimental and Numerical Investigation of Nanofluid Forced Convection inside a Wide Microchannel Heat Sink," ***Appl. Therm. Eng.,*** vol. 36, pp. 260-268, 2012.

[46] Kalteh, M., Abbassi, A., Saffar-Avval, M., Frijns, A., Darhuber, A., and Harting, J., "Experimental and Numerical Investigation of Nanofluid Forced Convection Inside a Wide Microchannel Heat Sink," ***Appl. Therm. Eng.***, vol. 36, pp. 260-268, 2012.

[47] Allahyari, S., Behzadmehr, A., and Sarvari, S.M.H., "Conjugate Heat Transfer of Laminar Mixed Convection of a Nanofluid Through an Inclined Tube with Circumferentially Non-Uniform Heating," ***Nanoscale Res. Lett.***, 6:360, 2011.

[48] Sidik, N.A.C., Khakbaz, M., and Jahanshaloo, L., Samion, S., Darus, A.N., "Simulation of Forced Convection in a Channel with Nanofluid by the Lattice Boltzmann Method," ***Nanoscale Res. Lett.***, 8:178, 2013.

[49] M.S. Manjunath, K.V. Karanth, and N.Y. Sharma, "A Comparative CFD Study on Solar Dimple Plate Collector with Flat Plate Collector to Augment the Thermal Performance", ***World Academy of Science, Engineering and Technology,*** Vol. 6, pp. 10-21 (2012).

[50] Ramani, B.M., Gupta, A., and Kumar, R., "Performance of a Double Pass Solar Air Collector," ***Sol. Energy***, vol. 84, pp.1929–1937, 2010.

[51] A. Mathur, G.D. Agrawal, and M. Chandel, "Recent Developments in the Field of Solar Water Heater Using Flat Plate Collector- a Review", International Journal of Advanced Engineering Technology, Vol. III, issue II, pp. 68-70 (2012).

[52] Ladjevardi, S.M., Asnaghi, A., Izadkhast, P.S., and Kashani, A.H., "Applicability of Graphite Nanofluids in Direct Solar Energy Absorption," ***Sol. Energy***, vol. 94, pp. 327–334, 2013.

[53] Tyagi, H., Phelan, P., and Prashher, R., "Predicted Efficiency of a Low-Temperature Nanofluid-Based Direct Absorption Solar Collector," ***J. Sol. Energ. T-ASME***, vol. 131, p. 041004, 2009.

[54] ASHRAE Standard 93-86, "Methods of Testing to Determine the Thermal Performance of Solar Collectors," Atlanta, GA, USA, 1986.

[55] Yousefi, T., Veysi, F., Shojaeizadeh, E., and Zinadini, S., "An Experimental Investigation on the Effect of Al_2O_3-H_2O Nanofluid on the Efficiency of Flat-Plate Solar Collectors," ***Renew. Energ.***, vol. 39, pp. 293-298, 2012.

[56] Jamal-Abad, M.T., Zamzamian, A., Imani, E., and Mansouri, M., "Experimental Study of the Performance of a Flat-plate Collector Using Cu–water Nanofluid," ***J. Thermophys. Heat Tr.***, doi: 10.2514/1.T4074.

[57] Yousefi, T., Veysi, F., Shojaeizadeh, E., and Zinadini, S., "An Experimental Investigation on the Effect of MWCNT-H_2O Nanofluid on the Efficiency of Flat-plate Solar Collectors," ***Exp. Therm. Fluid Sci.***, vol. 39, pp. 207–212, 2012.

[58] R.K. Sambare, and S.V. Prayagi, "Enhancement of Heat Transfer in Solar Collectors with Nanofluid: a Review", ***International Journal of Engineering Research & Technology***, Vol. 3 issue 11, pp. 480-484 (2014).

[59] Nasrin, R., Parvin, S., and Alim, M.A., "Effect of Prandtl Number on Free Convection in a Solar Collector Filled with Nanofluid," in ***5th BSME International Conference on Thermal Engineering, Procedia Engineering***, Vol. 56, pp. 54-62 (2013).

[60] E.A.H. Tora, and T. Moustafa, "Numerical Simulation of an Al_2O_3-H_2O Nanofluid as a

Heat Transfer Agent for a Flat-Plate Solar Collector", *International Journal of Scientific & Engineering Research*, Vol. 4, issue 5, pp. 562-573 (2013).

[61] Klein, S.A., "Calculation of flat plate collector loss coefficients," ***Sol. Energy***, vol. 17, pp. 79–80, 1975.

[62] Nguyen, C.T., Desgranges, F., Roy, G., Galanis, N., Maŕe, T., Boucher, S., and Mintsa, H.A., "Temperature and particle-size dependent viscosity data for waterbased nanofluids–hysteresis phenomenon," Int. J. Heat Fluid Flow, vol. 28, pp. 1492–1506, 2007.

[63] Eastman, J.A., Choi, U.S., Li, S., Thompson, L.J., and Lee, S., "Enhanced thermal conductivity through the development of nanofuids," in S. Komarneni, J.C. Parker and H.J. Wollenberger (eds.). ***Nanophase and Nanocomposite Materials II,*** pp. 3-11, MRS, Pittsburg, PA, 1997.

[64] Ferziger, J. (1999) ***Computational Methods for Fluid Dynamics.*** Springer.

[65] Versteeg, H.K., and Malalasekera, W., "An Introduction to Computational Fluid Dynamics-The Finite Volume Method," chap. 5, pp. 85-123, Longman Group Ltd., England, 1995.

[66] Spalding, D.B., "A Novel Finite-difference Formulation for Differential Expressions Involving Both First and Second Derivatives," Int. J. Numer. Methods Eng., vol. 4, p. 551, 1972.

[67] Patankar, S.V. (1980) ***Numerical Heat Transfer and Fluid Flow***. Hemisphere Publishing Corporation, Taylor & Francis Group, New York.

[68] Harlow, F.H., and Welch, J.E., "Numerical Calculation of Time-dependent Viscous Incompressible Flow of Fluid with Free Surface, Phys. Fluids, vol. 8, pp. 2182-2189, 1965.

[69] Versteeg, H.K., and Malalasekera, W., "An Introduction to Computational Fluid Dynamics-The Finite Volume Method," chap. 9, pp. 192-208, Longman Group Ltd., England, 1995.

[70] Shah, R. K., and London, A. L., "Laminar Forced Convection in Ducts," ***Adv. Heat Transfer***, Academic Press, New York, 1978.